EXTRACELLULAR AND SARCOMERIC ALTERATIONS IN MARFAN SYNDROME: INSIGHTS FROM AORTIC FIBRILLIN-1 AND MYOCARDIAL TITIN INVESTIGATIONS

PhD Thesis

Cristina-Maria Șulea, MD

Semmelweis University Doctoral School

Cardiovascular Medicine and Research Division

Supervisors: Miklós Kellermayer, MD, DSc
Zoltán Szabolcs, MD, PhD

Official reviewers: Zoltán Péter Jakus, MD, PhD
Attila Borbély, MD, PhD

Head of the Complex Examination Committee:
Zoltán Benyó, MD, DSc

Members of the Complex Examination Committee:
Bálint Dér, MD, PhD
Márton Kolossváry, MD, PhD

Budapest
2025

Table of Contents

List of Abbreviations

AFM: atomic force microscopy/microscope
BMI: body mass index
C: control (sample)
cbEGF: calcium-binding epidermal growth factor-like domain
DCM: dilated cardiomyopathy
DN: dominant-negative
ECM: extracellular matrix
EDTA: ethylenediaminetetraacetic acid
EGF: epidermal growth factor
***FBN1*:** fibrillin-1 gene
FBN2: fibrillin-2 gene
FBN3: fibrillin-3 gene
HI: haploinsufficiency
HTAD: heritable thoracic aortic disease
IB-H: interbead region height
ID: identification code
Ig: immunoglobulin
IQR: interquartile range
LAP: latency-associated protein
LDS: Loeys-Dietz syndrome
LLC: large latent complex
LTBP: latent transforming growth factor-beta binding protein
LV: left ventricle
MFS: Marfan syndrome (group/sample)
MHC: myosin heavy chain
MMP: matrix metalloproteinases
mRNA: messenger ribonucleic acid
N2B: short cardiac titin isoform
N2BA: long cardiac titin isoform
NMD: nonsense-mediated mRNA decay
Nx3: novex-3-specific region
PEVK: proline- (P), glutamate- (E), valine- (V), and lysine (L)-rich domain
PLL: poly-L-lysine
PMSF: phenylmethylsulfonyl fluoride
PTC: premature termination codon
RGD: arginine-glycine-aspartic acid motif
(R-)SMAD: (receptor-regulated) small mothers against decapentaplegic protein
SD: standard deviation
SDS: sodium dodecyl sulfate
SLC: small latent complex
T1: full-length titin (N2BA + N2B)
T2: titin's proteolytic degradation product
TGF-β: transforming growth factor-beta
TGFBR1/2: transforming growth factor-beta receptor type 1/2
TT: total titin amount (T1 + T2)
***TTN*:** titin gene
***TTN*tv:** titin gene truncating variant
***TTN*tv-:** absence of truncation in the titin gene
UMD: Universal Mutation Database
US/LS: upper-to-lower segment ratio

1. Introduction

The history of Marfan syndrome (MFS) began with it being clinically described for the first time in 1896 by French pediatrician Antoine-Bernard Marfan, who presented the case of a five-year-old girl exhibiting elongated limbs and joint contractures [1]. Although the complete clinical picture of what would later be recognized as MFS was not captured in this initial description, subsequent case reports expanded the phenotypic profile of the disorder, including notable associations with skeletal abnormalities, ocular manifestations, and, most critically, cardiovascular involvement, particularly aneurysmal dilation of the ascending aorta, which was increasingly recognized as a major cause of morbidity and mortality [2].

MFS is currently considered the most prevalent and extensively studied fibrillinopathy, affecting approximately 1 in 5,000 individuals worldwide regardless of sex or race [3]. It is caused by fibrillin-1 gene (*FBN1*) mutations, which occur *de novo* in approximately 25% of cases, although the majority (roughly 75%) are inherited following an autosomal dominant pattern [4]. In exceptional cases, recessive *FBN1* mutations have also been described [5]. *FBN1* encodes the glycoprotein fibrillin-1, an essential component of microfibrils within the extracellular matrix (ECM) of connective tissues. The ubiquitous distribution of fibrillin-1 underlies the multisystemic involvement in MFS [6,7]. However, of primary concern is the vast cardiovascular pathology, encompassing aortic disease, valvular dysfunction, pulmonary artery and extra-aortic vascular involvement, arrhythmia, and primary cardiomyopathy [8].

The aneurysmal dilation of the aorta and its subsequent progression to acute aortic events represent the main determinants of survival in up to 80% of the Marfan population [9]. Aortic wall dissection occurs in MFS individuals at a younger age compared to the general cohort [10]. In this regard, timely prophylactic aortic surgery constitutes the most effective intervention to avoid life-threatening complications and improve life expectancy [11,12]. Current strategies advocate for integrating molecular data into surgical decision-making, with growing interest in establishing genotype-phenotype correlations. Specific *FBN1* mutations are being investigated for their potential to enhance risk stratification and facilitate more personalized, timely surgical management of individuals living with MFS [13].

1.1. Genetics of Marfan syndrome

In humans, the fibrillin protein family comprises three homologous isoforms – fibrillin-1, fibrillin-2, and fibrillin-3 – encoded by *FBN1*, *FBN2*, and *FBN3*, respectively. Among these, *FBN1*, located on the long arm of chromosome 15 (15q21.1), is associated with MFS [14]. *FBN1* contains 65 coding exons and spans approximately 200 kilobases, producing a large, cysteine-rich glycoprotein that is pivotal to the architecture and function of extracellular microfibrils [15,16]. Over 3,000 mutations have been identified in *FBN1* [17]. The resulting molecular dysfunction typically involves a dominant-negative (DN) effect or haploinsufficiency (HI).

The DN effect is predominantly attributed to missense mutations, which result in the substitution of a single amino acid within the fibrillin-1 polypeptide chain. These mutations do not typically affect the overall length of the protein, as the open reading frame remains intact; rather, they induce a qualitative alteration in the protein's primary structure [18]. As a result, both the wild-type and mutant alleles are transcribed and translated, leading to the synthesis of a full complement of fibrillin-1 molecules. However, the incorporation of structurally aberrant monomers into multimeric microfibrils impairs their assembly or function [19]. Additionally, as cysteine residues are critical for intra-domain stability and inter-domain and supramolecular assembly, DN mutations are further classified based on cysteine involvement [20,21]. By contrast, HI may arise through several distinct genetic mechanisms that ultimately result in the quantitative or functional loss of one *FBN1* allele. "True" HI occurs when transcription or translation is completely disrupted by the deletion of the entire gene or its critical coding regions, and is primarily associated with an overall reduction of the amount of functional fibrillin-1, which leads to quantitative deficits in microfibrillar formation [22]. Functional HI is mostly associated with nonsense mutations, which introduce a premature termination codon (PTC) within the *FBN1* messenger ribonucleic acid (mRNA) sequence. This aberration leads to early cessation of translation and the production of a truncated, typically nonfunctional polypeptide. In most cases, the mutant transcript undergoes nonsense-mediated mRNA decay (NMD) or the resulting polypeptide is subject to accelerated degradation due to misfolding or instability. The consequence is, conceivably, a quantitative deficiency of functional fibrillin-1, because only the wild-type allele remains capable of producing the full-length protein. This monoallelic expression

is insufficient to maintain normal microfibrillar architecture and function, particularly in tissues subjected to high mechanical stress [23].

1.2. Molecular basis

1.2.1. Fibrillin-1

From an evolutionary perspective, fibrillin-1 is a highly conserved protein across vertebrate species, playing a fundamental role in the structural and regulatory organization of connective tissues [24]. In the human organism, it serves as the main component of fibrillin-1 microfibrils, which are integral to the physiology of the ECM, fulfilling both mechanical and signaling purposes [25]. During histogenesis, fibrillin-1 microfibrils build a scaffold for the formation of elastic fibers, later becoming embedded in the elastin network, where they contribute significantly to tissue elasticity [26,27]. Fibrillin-1 microfibrils represent a mechanical backbone not only in elastin-rich, highly dynamic tissues and organs (e.g., ligaments, dermis, pulmonary parenchyma, aortic wall), where they contribute to long-range elastic recoil, but also in structures virtually devoid of elastin, including the ciliary zonule, renal glomerulus, and tendon, where they primarily provide tensile strength and structural resilience [28].

As a large, cysteine-rich glycoprotein, fibrillin-1 encompasses 2,871 amino acids and is estimated to have a molecular weight of 320 kDa in its active form [29]. Its modular structure (**Figure 1**) is primarily composed of 47 epidermal growth factor (EGF)-like domains, of which 43 possess calcium-binding capability (cbEGF) [30]. The binding of calcium to the cbEGF domains protects the fibrillin-1 molecule against proteolytic degradation and maintains its structural integrity [31,32]. Moreover, it stabilizes the rigid, rod-like structure of certain domains, thus facilitating the role of microfibrils in load-bearing tissues [33]. Interspersed among the EGF domains are seven transforming growth factor-β-binding protein-like (TB) domains – also referred to as 8-cysteine domains – with TB4 containing an arginine-glycine-aspartic acid (RGD) motif that facilitates interactions with integrin receptors, thereby promoting cell adhesion [34,35]. Additional modules include two hybrid domains, which exhibit structural similarities to both cbEGF and TB domains; a variable, proline-rich domain, which differs from its fibrillin-2 and -3 homologs in that they contain either glycine or both proline and glycine, respectively; and unique N- and C-terminal domains, the latter being critical for the furin-mediated

proteolytical processing that precedes the assembly of fibrillin-1 molecules into microfibrils [26,36].

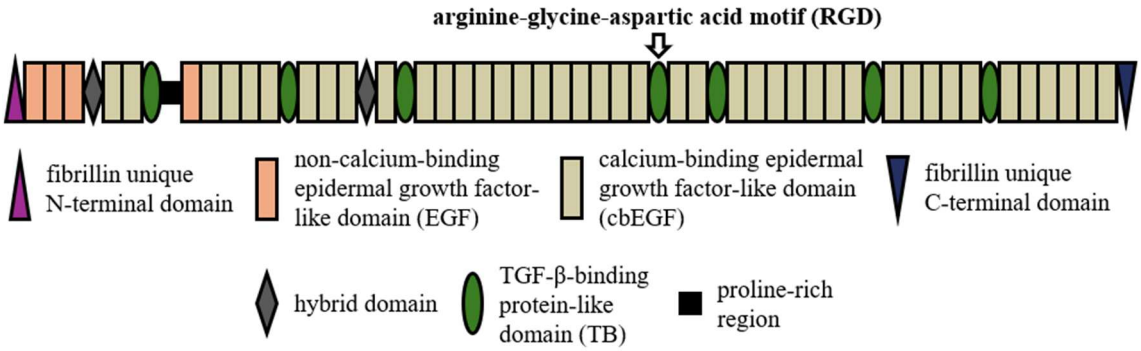

Figure 1. The domain structure of fibrillin-1. Adapted from Șulea *et al*. [37].

Fibrillin-1 engages in a vast array of molecular interactions mediated by its various domains. Through its N-terminal region, it interacts with heparan sulfate proteoglycans, contributing to the spatial organization of matrix components and influencing cellular behavior [38]. Its cbEGF and TB domains form covalent and non-covalent associations with other ECM components, including elastin, versican, fibulins, microfibril-associated glycoproteins, fibrillin-2, and latent transforming growth factor-β binding proteins (LTBPs) [27,39-43]. These molecular interactions are essential for the assembly and stability of microfibrils and for the proper sequestration and regulation of transforming growth factor-β (TGF-β) signaling. The dysregulation of the latter mechanism is mainly incriminated in the pathogenesis of aortopathy and other MFS-specific manifestations. Therefore, the regulatory role of fibrillin-1 in modulating TGF-β bioavailability warrants special consideration.

1.2.2. TGF-β signaling

The TGF-β signaling cascade regulates a wide array of cellular processes. In mammals, the TGF-β family comprises three isoforms – TGF-β1, TGF-β2, and TGF-β3 – that exert their functions through canonical and non-canonical intracellular signaling pathways [44-46]. In its canonical form, TGF-β signaling is initiated upon ligand binding to a heterotetrameric receptor complex composed of two type I TGF-β receptors (TGFBR1) and two type II TGF-β receptors (TGFBR2). Ligand binding prompts TGFBR2 to phosphorylate and activate TGFBR1, which phosphorylates receptor-regulated small mothers against decapentaplegic (R-SMAD) proteins, primarily SMAD2

and SMAD3. Through the further involvement of the common mediator SMAD4, they translocate to the nucleus to regulate the transcription of target genes [47,48]. The canonical pathway is responsible for the induction of ECM components (e.g., collagen, fibronectin), modulation of inflammatory responses, and control of cell cycle regulators. The non-canonical activation relies on several SMAD-independent cascades involving, among others, mitogen-activated protein kinase, phosphatidylinositol 3-kinase, or TGF-β-activated kinase 1, and is implicated in numerous cellular events, such as survival and metabolism, migration, proliferation, and apoptosis [49].

TGF-β is initially synthesized in precursor form, as part of a small latent complex (SLC) composed of the mature cytokine non-covalently bound to a latency-associated peptide (LAP) [50]. Through the LAP, the SLC is then covalently linked via disulfide bonds to an LTBP, forming the large latent complex (LLC) [51]. Following its secretion from the cell, the LLC is sequestered in the ECM, and its availability is tightly controlled to prevent untimely or excessive signaling. Fibrillin-1 plays a central role in this regulation by anchoring the LLC to the microfibrillar network through specific interactions with LTBPs [52]. Therefore, fibrillin-1 exerts control over TGF-β activation. The release of active TGF-β from the ECM can be induced by proteolytic cleavage mediated by matrix metalloproteinases (MMP), mechanical strain, or integrin-mediated conformational changes [49,53,54].

Genetic mutations leading to aberrant TGF-β signaling have been associated with disorders of the connective tissue. In MFS, *FBN1* mutations compromise the integrity of fibrillin-1 and thus its ability to bind LTBPs and sequestrate TGF-β, a mechanism that has been strongly implicated in the development of the disorder's clinical manifestations, including aortic aneurysm formation and emphysematous changes in the pulmonary parenchyma [55,56]. Increased TGF-β transduction has been found to promote fibrogenesis, as demonstrated by murine experiments in which exogenous cytokine administration to subcutaneous or pulmonary tissue induced fibrotic reactions [57,58]. Independent studies further established plasma TGF-β levels as a prognostic biomarker for aortic events in adult human subjects with MFS [59,60]. It is, however, plausible that an interplay exists between biochemical dysregulation and mechanical failure, whereby structurally impaired microfibrils contribute to and amplify tissue dysfunction.

1.2.3. Fibrillin-1 microfibrils

Fibrillin-1 molecules assemble to form microfibrils with a beaded structure characterized by 56 nm periodicity (i.e., the distance between the centers of two successive beads) and an approximate mass of 2.55 MDa per repeat [61]. They have been described as measuring 10–12 nm in diameter based on early transmission electron microscopy images [7]. Immunofluorescence studies placed fibrillin-1 microfibrils in the ECM of various tissues such as the dermis, aortic media, pulmonary and hepatic parenchyma, tendon and cartilage, and ocular structures, where they associate with basement membranes, elastic fibers, and integrin-rich cell surfaces, forming an extensive and well-organized matrix scaffold [62-66]. Their arrangement and overall abundance are influenced not only by *FBN1* defects, but also by various other pathological conditions and lifestyle factors, such as diabetes mellitus, photoaging, smoking, and chronic kidney disease [67-69].

The assembly of fibrillin-1 microfibrils takes place on the cell surface, where fibrillin-1 monomers that had initially undergone preprotein processing and multimerization are aligned in a head-to-tail configuration [36]. The interaction between the N- and C-terminal ends of adjacent fibrillin-1 molecules is facilitated by furin-mediated proteolytic cleavage, which enables the subsequent axial and lateral assembly [26,36,70]. The process is further regulated by additional molecules that promote stronger multimer binding, such as heparan sulfate proteoglycans, glutamine aminotransferase, and fibronectin. However, microfibrillar assembly may depend on cell type and, subsequently, the presence or absence of fibronectin networks [71].

The ultrastructure of fibrillin-1 microfibrils is made of alternating beads and connecting segments, which further contain arms, a central interbead region, and a shoulder region [72]. Scanning transmission electron microscopy mass mapping demonstrated that the regions of highest mass correspond with the beads, accounting for approximately 1.1 MDa [73,74]. Studies using various imaging techniques have reported a range of bead diameters, from approximately 15–18 nm in automated electron tomography data sets to 30–40 nm in atomic force microscopy (AFM) [75,76]. However, bead morphology seems to be tissue-dependent [77].

The precise spatial arrangement of fibrillin-1 monomers within the microfibrillar architecture has been a subject of considerable debate. Several models have been proposed, each aiming to integrate structural observations with biochemical findings. They have included both parallel (head-to-tail) and antiparallel alignments, as well as staggered and unstaggered configurations [78]. Given the length of a single fibrillin-1 monomer (148 nm) [79] and the observed microfibrillar periodicity of approximately 56 nm, different theories have suggested certain degrees of molecular folding where fibrillin-1 molecules span one, two, or three repeats [80-82]. However, a completely extended state of the fibrillin-1 molecules within relaxed microfibrils would be unable to explain their extensibility. Regardless of the degree of stagger, all models propose that both N- and C-terminal ends of the molecules interact in or near the beads. Additionally, it has been demonstrated that eight parallel fibrillin-1 molecules can be accommodated along the microfibrillar axis [76,83].

Fibrillin-1 microfibrils possess distinct mechanical properties that allow them to provide both tensile strength and elasticity within the ECM. In the ciliary zonule, which is made predominantly of fibrillin-1 bundles, these microfibrils act like reinforcing structures, demonstrated by a lower breaking force due to a depleted fibrillin-1 network [84]. Under mechanical stress, which may occur physiologically in elastic tissues, the microfibrillar assemblies are capable of significant elongation without permanent deformation. Within the 56–90 nm periodicity range, they are capable of reversible stretch and recoil owing to TB-cbEGF interdomain sliding events within the interbead segments exclusively. Extension above 90–100 nm was found to be accompanied by irreversible conformational changes, hinting at the unravelling of the beads [73,85].

Efforts to characterize the elasticity of fibrillin-1 microfibrils have yielded a wide spectrum of results, reflecting not only the diversity of the experimental setups across studies but also the wide variety of tissue sources from which samples have been obtained. Due to the invasiveness of human tissue harvesting for mechanical testing, most studies have relied on animal models to estimate microfibrillar Young's modulus. This fundamental measure of stiffness quantifies how much a material resists deformation under stress, defined as the ratio of applied stress to the resulting strain [86]. The studies demonstrated estimates for the Young's modulus of pure fibrillin-1 microfibrils or fibrillin-1-containing elastic fibers spanning three orders of magnitude – from 0.2 MPa

to 96 MPa – emphasizing the influence of both biological variability and methodological design (**Table 1**).

Table 1. Previously estimated Young's modulus values of fibrillin-1-containing structures.

Species	Tissue	Method	Young's modulus
sea cucumber	dermis network	macroscopic stretching	0.2 MPa [87]
pig	aorta	mechanical testing	0.4 MPa [88]
octopus	aorta	mechanical testing	0.4 MPa [89]
horse	ligamentum nuchae	AFM indentation	0.56–0.74 MPa [90]
jellyfish	mesogleal fibers	mechanical testing	0.9 MPa [91]
lobster	aorta	transmural pressure	1.06 MPa [92]
cow	zonular filament	macroscopic stretching	0.19–1.88 MPa [93]
cow	zonular filament	molecular combing	78–96 MPa [85]

In the aortic wall, fibrillin-1 microfibrils exhibit a circumferential disposition within the media, where they form a sheath-like structure around the amorphous core of elastic fibers and are interwoven with collagen fibers and smooth muscle cells [94]. Their dysfunction, whether through impaired regulatory capacity or altered biomechanical properties, has been identified as a central pathogenic mechanism in the development of clinical manifestations in MFS.

1.3. Clinical manifestations

The clinical picture of MFS includes a broad spectrum of features due to the ubiquitous role of fibrillin-1 in connective tissue homeostasis. Moreover, the disorder presents with high variability even among individuals carrying the same mutation [95]. However, MFS symptomatology is dominated by disorders of the skeletal, ocular, and cardiovascular systems. Although skeletal and ocular manifestations are clinically relevant and impact quality of life, cardiovascular involvement remains the primary area of concern, as it is associated with the highest morbidity and mortality in MFS.

Skeletal involvement is one of the most visually apparent hallmarks of MFS and is often the first feature to raise clinical suspicion. The skeletal phenotype is predominantly characterized by excessive linear growth of the long bones, leading to a typically tall and slender *habitus* with disproportionate limb length and arachnodactyly [96]. These characteristics translate into key diagnostic features, such as reduced upper-to-lower segment ratio (US/LS), increased arm span-to-height ratio, and the thumb and

wrist signs. Additional features include *pectus excavatum* or *carinatum*, scoliosis or kyphosis, joint hypermobility, and foot deformities. Craniofacial features may also be present in the form of dolichocephaly, down-slanting palpebral fissures, enophthalmos, retrognathia, and malar hypoplasia. These manifestations reflect the underlying connective tissue laxity and may significantly impact quality of life, requiring corrective surgery [97].

The eye is another major site of clinical involvement. The cardinal ocular manifestation in MFS is *ectopia lentis*, which occurs in up to approximately 70% of patients [98]. The lens typically displaces upward and temporally due to weakened or fragmented zonular fibers, which are rich in fibrillin-1. Other ophthalmological findings include myopia (often severe), increased axial length of the eye globe, early-onset cataracts, and a predisposition to retinal detachment [99]. These changes may significantly impair visual acuity and require regular ophthalmologic surveillance and, in some cases, surgical intervention.

Other important physical manifestations include spontaneous pneumothorax, dural ectasia, skin lesions, particularly *striae atrophicae*, and an increased tendency to develop hernias due to connective tissue fragility [14]. Obstructive respiratory impairment occurs in 20 to 25% of patients [100,101]. Nevertheless, the most critical and potentially fatal manifestations of MFS occur within the cardiovascular system, making its thorough monitoring and timely management essential.

1.3.1. Aortic involvement

The aortic root is the most commonly affected vascular segment in MFS. Its progressive dilation, occurring particularly at the level of the sinuses of Valsalva, results from a structural degeneration within the medial layer of the aortic wall, including elastic fiber fragmentation, smooth muscle cell loss, and ECM disorganization, a process exacerbated by aberrant TGF-β signaling [102]. As the aortic diameter increases, wall tension rises, predisposing the aorta to continued dilation and the risk of aneurysm development. A predisposing factor for this specific localization, besides the locally increased blood pressure, may be the thinner and stiffer structure of the sinuses of Valsalva compared to other aortic segments [103].

Typically, an aneurysm refers to the localized enlargement of a vessel by more than 50% of its normal diameter. However, as the risk of dissection is significantly elevated even at smaller sizes, in clinical practice, it is defined as an aortic diameter of 45 mm or more [104]. In MFS, a standardized measure, known as the aortic Z-score, is used to assess whether the aortic root diameter is abnormally enlarged relative to the patient's body surface area, age, and sex by quantifying how many standard deviations (SD) the given measurement deviates from the mean of a matched healthy population [105].

Aortic root aneurysms in MFS typically develop during adolescence or early adulthood, but dilation may also be detectable in childhood [106]. The estimated prevalence of aortic aneurysm in individuals with MFS revolves around 90% by the age of 60 [107], with progression rates and onset age influenced by the specific nature of the *FBN1* mutation and other modifying factors [108]. Aortic root aneurysms tend to grow at a significantly accelerated rate in individuals with MFS, thereby elevating the risk of associated complications [109].

If aortic dilation is not identified and managed appropriately, it may be complicated by aortic dissection, a life-threatening condition characterized by the separation of the layers within the aortic wall. This disruption can severely compromise blood flow, leading to end-organ ischemia or, if affecting the ascending aorta, sudden death due to complications such as aortic rupture, acute aortic valve insufficiency, myocardial infarction, or cardiogenic shock [110]. MFS-related aortic dissections account for approximately 5% of all aortic dissection cases [111]. In MFS, aortic dissection occurs at a significantly younger age compared to the general population [10].

1.3.2. Extra-aortic vascular manifestations

Vasculopathy in MFS extends beyond the aortic root and ascending aorta. Dilation of the main pulmonary artery has been observed in up to 70% of adults and approximately 10% of pediatric patients with MFS [112,113]. Similar to proximal aortic dilation, pulmonary artery enlargement can become clinically relevant when exerting compression on adjacent structures. However, due to the lower pressure in the pulmonary circulation, dissection of the main pulmonary artery remains a rare complication [114]. Nonetheless, its presence seems to be associated with a more severe systemic phenotype in affected individuals [113].

Peripheral arterial involvement in MFS often presents as increased visceral, intracranial, or retinal artery tortuosity [115-117]. This condition describes the presence of abnormal curvature, looping, or kinking along the axis of a blood vessel. Although it has also been observed in other heritable aortopathies, arterial tortuosity has been proposed as an indicator of aortic phenotype severity in individuals with MFS [118,119].

1.3.3. Cardiac pathology

Beyond the well-documented vascular complications, MFS is also associated with distinct forms of cardiac involvement, primarily affecting the valves and, to a lesser degree, the myocardial function. Mitral valve prolapse is the most frequent valvular abnormality in MFS, with prevalence estimates reaching up to 80% [120]. It may present with varying degrees of mitral regurgitation and, in more severe cases, particularly among pediatric patients, can progress to congestive heart failure [121]. Mitral annular disjunction, defined as a structural separation between the mitral valve hinge point and the adjacent left ventricular (LV) myocardium, has been reported in a third of an MFS cohort and was associated with an elevated risk of arrhythmias [122]. Additionally, degenerative changes affecting the tricuspid valve have been documented in approximately 12% of MFS patients undergoing aortic or valvular surgery [123]. Aortic valve insufficiency may also occur, typically due to annular dilation related to progressive aortic root enlargement [124]. Nevertheless, myocardial dysfunction and LV impairment have been observed in MFS even in the absence of significant valvular disease and in pediatric populations, suggesting a possible intrinsic “Marfan cardiomyopathy”.

1.3.3.1. Marfan cardiomyopathy

Several studies have reported intrinsic myocardial dysfunction in patients with MFS, often characterized as mild in severity [125-127]. Decreased LV ejection fraction (below 55%) has been observed in up to 25% of cases [125]. Moreover, magnetic resonance studies have revealed subtle systolic impairment even in patients with preserved ejection fraction [128]. While biventricular dilation and dysfunction are typically subclinical and not accompanied by overt symptoms, these changes can manifest independently of other cardiovascular abnormalities, such as valvular pathology, suggesting a primary myocardial involvement. Current evidence suggests that this

inherent ventricular dysfunction may predispose MFS individuals to developing heart failure when exposed to additional cardiac stressors [127].

The underlying pathophysiology of Marfan cardiomyopathy is not yet fully elucidated. Abnormal fibrillin-1 microfibril architecture in the myocardium may impair force transmission across the ECM, contributing to reduced contractile performance. This hypothesis is supported by the spatial distribution of fibrillin-1 within the ventricular myocardium, where it is more abundantly localized in the inner trabecular region, the area that suffers the greatest mechanical stress and dynamic changes during the cardiac cycle [129]. Additionally, TGF-β dysregulation has been implicated in myocardial remodeling processes, including interstitial fibrosis, cellular hypertrophy, and apoptosis, further promoting myocardial dysfunction [130].

The primary myocardial dysfunction in MFS shares some phenotypic overlap with dilated cardiomyopathy (DCM), a myocardial disorder defined by enlargement of the cardiac chambers and compromised ventricular contractility. Approximately 40% of cases have a genetic origin, being caused by truncating variants in the *TTN* gene (*TTN*tv), which encodes the sarcomeric protein titin [131]. Although *TTN* gene mutations are not typically associated with MFS, the intrinsic nature of Marfan cardiomyopathy has led investigations into potentially overlapping molecular pathways.

1.3.3.2. Titin

Titin, the largest known human protein, ranks as the third most abundant myofilament in striated muscle after myosin and actin [132]. It spans from the Z-disk to the M-line within the half-sarcomere, contributing to structural integrity and passive muscle tension [133]. Due to distinct structural domains, titin's mechanical and functional properties vary along its length (**Figure 2**). The A-band region is largely inextensible, serving, hypothetically, as a scaffold for thick filament assembly through fibronectin type III and immunoglobulin (Ig)-like domains. The M-band portion supports structural and regulatory roles via protein interactions and a titin kinase domain [134]. In contrast, the I-band segment is elastic and contains extensible elements such as Ig regions, the special proline-, glutamate-, valine-, and lysine-rich (PEVK) domain, and the N2B-unique sequence, which confer titin's spring-like characteristics. Anchoring occurs at both ends

of the molecule, at the Z-disk and the M-band, where additional unique sequence motifs further contribute to titin's specialized structural and regulatory functions [135].

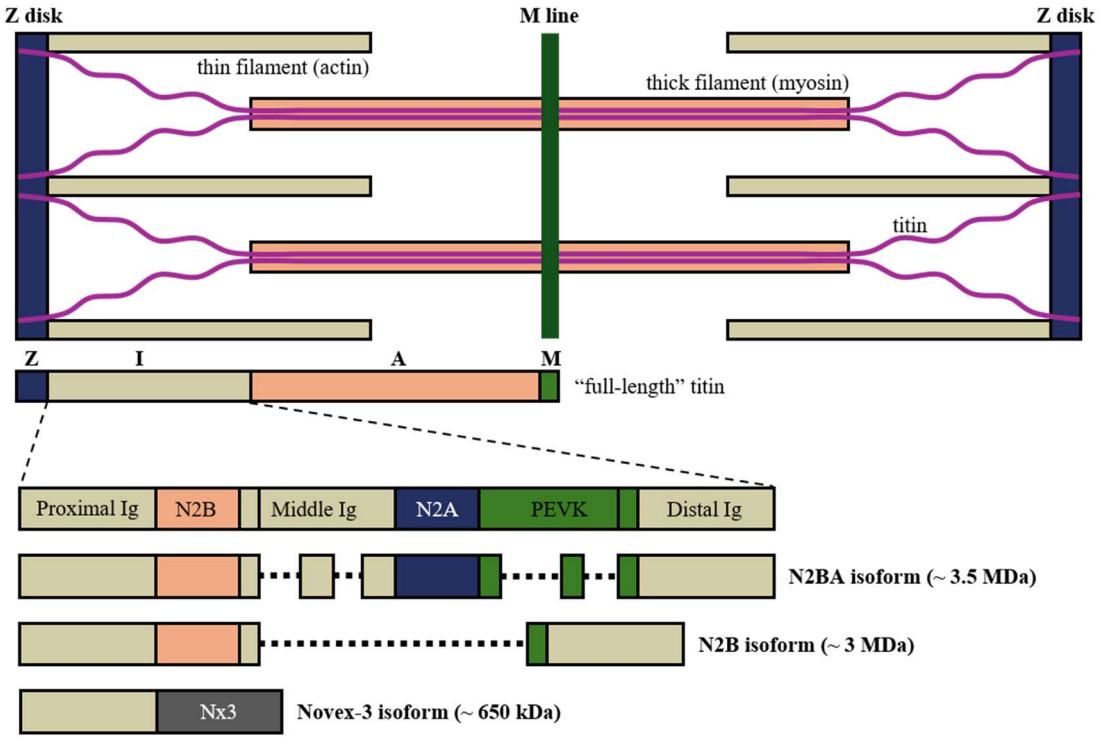

Figure 2. Disposition of titin in the sarcomere (top) and I-band structure of cardiac titin isoforms (bottom). Dotted lines mark alternative splicing sites. Adapted from Loescher *et al*. [135].

Titin exists in multiple isoforms that are generated through alternative mRNA splicing during development and differ in terms of stiffness and extensibility due to their different spring lengths [135]. This post-transcriptional regulatory mechanism occurs particularly in the I-band region and enables the myocardium to adapt its passive tension and compliance in response to various stimuli. In mammalian hearts, two primary isoforms are co-expressed in variable proportions: N2B, a shorter and stiffer variant, and N2BA, a longer and more compliant form (**Figure 2**). The relative expression of the two isoforms in the myocardium reflects species-specific hemodynamic demands: the N2B isoform is predominantly expressed in small mammals such as rodents, where it contributes to higher passive tension in the cardiac sarcomere and confers greater resistance to stretch, while the N2BA isoform is more prevalent in larger mammals such as pigs and humans, as it imparts greater elasticity and allows increased stroke volumes. Consequently, the N2BA:N2B ratio is around 0.25 in mice and approximately 0.66 in pigs [136], whereas in non-ischemic, non-diseased human myocardial tissue, the ratio ranges

between 0.47 and 0.56 [137,138]. The N2BA:N2B isoform ratio also adapts in response to physiological (e.g., endurance training) and pathological (e.g., diastolic dysfunction) conditions, where increased N2BA expression was observed [135,139]. This isoform shift appears to serve as an adaptive mechanism to modulate myocardial stiffness.

A minor myocardial isoform of titin, novex-3, is significantly shorter and lacks much of the extensible functionality. It primarily includes the novex-3-specific region (Nx3) and is thought to contribute to signaling pathways within the myocardium and sarcomeric remodeling triggered by mechanical stretch, both during muscle development and in the context of cardiac disease [140].

1.4. Diagnosis

The precise and timely diagnosis of MFS is critical, given the overall morbidity and potentially life-threatening cardiovascular complications associated with the disease. MFS is currently diagnosed based on a set of clinical criteria known as the revised Ghent nosology, first established in 1996 and updated in 2010 to enhance its diagnostic value and to incorporate molecular genetic findings [14]. The updated Ghent criteria emphasize the importance of aortic involvement and *ectopia lentis*, alongside systemic manifestations and a confirmed pathogenic variant in *FBN1*.

A definitive diagnosis in the absence of a positive family history relies on the presence of one of the following four scenarios [14]:

1. aortic Z-score ≥ 2 or aortic dissection AND *ectopia lentis*;
2. aortic Z-score ≥ 2 or aortic dissection AND *FBN1* mutation;
3. aortic Z-score ≥ 2 or aortic dissection AND systemic score ≥ 7;
4. *ectopia lentis* AND *FBN1* mutation known to be associated with aortic aneurysm.

In individuals with a positive family history of MFS, the presence of any one of the following criteria is sufficient for diagnosis [14]:

1. *ectopia lentis*;
2. systemic score ≥ 7;
3. aortic Z-score ≥ 2 or ≥ 3 above or below the age of 20, respectively.

The systemic score quantifies the degree of systemic connective tissue involvement by assigning specific point values to various physical features based on their

relevance to the disorder (**Table 2**). A cumulative score of at least 7 points supports systemic involvement consistent with MFS [14].

Table 2. Physical manifestations included in the calculation of the systemic score. Adapted from Loeys *et al*. [14].

Physical feature	**Points**
Wrist AND thumb sign	3
Wrist OR thumb sign	1
Pectus carinatum	2
Pectus excavatum OR chest asymmetry	1
Hindfoot deformity	2
Pes planus	1
Spontaneous pneumothorax	2
Dural ectasia (on imaging)	2
Protrusio acetabuli (on imaging)	2
Reduced US/LS AND increased arm span-to-height ratio AND no severe scoliosis	1
Scoliosis OR thoracolumbar kyphosis	1
Reduced elbow extension (less than 170°)	1
Facial features (at least three of the following: dolichocephaly, enophthalmos, downslanting palpebral fissures, malar hypoplasia, retrognathia)	1
Skin striae	1
Myopia greater than 3 diopters	1
Mitral valve prolapse (on echocardiography)	1

Genetic testing for *FBN1* mutations has become an essential component in the management of MFS, improving diagnostic accuracy and facilitating familial screening. Given the considerable phenotypic variability of MFS and its clinical overlap with other connective tissue disorders, molecular confirmation can significantly aid in distinguishing MFS from related conditions. In a research setting, exploring genotype-phenotype correlations has revealed that certain *FBN1* mutation types may be associated with distinct clinical patterns and disorder severity, thus offering potential for a more personalized approach to patient care in this population [141].

1.4.1. Differential diagnosis

MFS represents the most prevalent syndromic form of heritable thoracic aortic disease (HTAD), a spectrum of genetic disorders characterized by an increased risk of thoracic aortic aneurysms, dissections, and related vascular abnormalities. Eleven genes, including *FBN1*, are strongly linked to HTAD [142]. Some variants cause non-syndromic forms of HTAD, such as bicuspid aortic valve and familial thoracic aortic aneurysm and dissection, which should still be considered in the differential diagnosis of MFS despite

the absence of widespread systemic features [143]. Distinguishing MFS from related HTADs is critical for appropriate surveillance, management, and genetic counseling [144]. In ambiguous cases, especially in young individuals or those with incomplete phenotypes, molecular testing is the definitive tool in establishing the correct diagnosis.

Loeys-Dietz syndrome (LDS) is perhaps the most phenotypically similar condition to MFS, characterized by arterial tortuosity and aortic disease. Unlike MFS, LDS involves craniofacial abnormalities and more aggressive vascular disease with widespread aneurysms and dissection at smaller aortic diameters, warranting earlier surgical intervention. Genetic testing is essential to differentiate the disorders, as LDS is typically associated with mutations in genes of the TGF-β signaling cascade [145].

Ehlers-Danlos syndrome encompasses a spectrum of disorders primarily affecting collagen-encoding genes, leading to symptoms such as skin hyperextensibility, tissue fragility, and joint hypermobility. Its vascular subtype is particularly notable for severe arterial complications such as spontaneous arterial rupture without significant aneurysmal dilation, often in peripheral arteries rather than the ascending aorta [145].

Additional *FBN1*-associated conditions to include are Shprintzen-Goldberg syndrome, presenting with craniosynostosis and skeletal features but rare aortic manifestations; the MASS phenotype, consisting of mitral valve prolapse, myopia, non-progressive aortic root dilation, musculoskeletal manifestations, and skin striae; and familial *ectopia lentis*, which lacks aortic features [114]. Congenital contractural arachnodactyly (Beals-Hecht syndrome) presents with disproportionally long extremities, arachnodactyly, and tall stature, features that closely resemble MFS, but is distinguished by congenital joint contractures and characteristic external ear malformations. Aortic involvement is uncommon. The condition is caused by *FBN2* pathogenic variants [146].

1.4.2. Genotype-phenotype correlations

Studies indicate that the type and localization of *FBN1* mutations influence the clinical phenotype and prognosis of MFS. *Ectopia lentis* was found to strongly correlate with missense mutations affecting cysteine residues within fibrillin-1 [108,147]. Similarly, PTC mutations are more frequently linked to pronounced skeletal and skin manifestations [107]. Mutations clustered in a specific region of *FBN1*, namely exons 24–32, associate with the occurrence of neonatal MFS, a severe, early-onset form of the

disease marked by severe physical manifestations and high early mortality due to cardiac failure [148]. At the tissue level, this phenotype corresponds to severely compromised microfibril formation, where fibroblasts fail to assemble fibrillin-1 into organized microfibrils, resulting in nearly absent elastic fiber formation [149].

Franken *et al*. reported that MFS patients with HI variants had a 2.5-fold higher risk of experiencing cardiovascular death and a 1.6-fold greater likelihood of developing aortic complications compared to those with DN variants [141]. These findings are supported by murine experiments, where HI mutations resulted in a sparser microfibrillar matrix with reduced tensile strength [150]. These insights warrant the importance of further nanoscale structural and biomechanical investigations, as they may reveal key features underlying the pathomechanism of MFS.

1.5. Management

In addition to multidisciplinary care addressing the systemic manifestations of MFS and lifestyle changes to limit physical exertion, the primary focus of MFS management is the prevention of life-threatening cardiovascular complications. Given the often silent progression of aortic dilation until advanced stages, regular imaging surveillance (e.g., echocardiography, magnetic resonance imaging, etc.) is essential for monitoring aortic root size and detecting enlargement. Pharmacotherapy with beta-blockers or angiotensin receptor blockers (e.g., losartan) is commonly prescribed to reduce hemodynamic stress on the aorta. Prophylactic surgery is typically recommended upon reaching an aortic root diameter of 50 mm, or even earlier (at 45 mm) in the presence of rapid growth (≥ 5 mm/year), a family history of acute aortic events, or additional risk factors such as severe aortic regurgitation or pregnancy [151]. Composite graft replacement (Bentall procedure) is preferred for managing aortic root dilation in MFS, with valve-sparing approaches (Yacoub and Tirone-David procedures) increasingly favored when anatomically feasible [12,152]. Psychological challenges also warrant attention, as MFS significantly impacts psychosocial well-being, particularly influenced by surgery [153,154]. Optimizing patient selection and the timing of preventive surgery require the identification of accurate prognostic markers. A deeper understanding of the tissue-level alterations in MFS could provide valuable insight into disease progression and support the development of improved therapeutic strategies.

2. Objectives

As dysregulation of the TGF-β signaling pathway is widely regarded as the central mechanism underlying the pathophysiology of MFS, the nanoscale characteristics of fibrillin-1 microfibrils remain insufficiently explored. In particular, human aortic fibrillin-1 microfibrils have not yet been directly investigated at the ultrastructural level. Additionally, increasing evidence of myocardial involvement suggests that the giant sarcomeric protein titin, a key determinant of cardiomyocyte elasticity and function, may play a role in Marfan cardiomyopathy. The present research aimed to address these understudied aspects, offering new insights into the molecular consequences of MFS on the cardiovascular system.

The primary objectives of this study were as follows:

1. **To investigate the morphological and nanomechanical properties of individual fibrillin-1 microfibrils isolated from human aortic tissue in MFS and non-MFS individuals. This included:**
    a. assessing structural dimensions and stiffness of human aortic fibrillin-1 microfibrils using AFM;
    b. evaluating the impact of *FBN1* mutations on the morphology and biomechanics of single fibrillin-1 microfibrils in MFS;
    c. exploring potential associations between types of *FBN1* mutations and measured biophysical parameters, thereby contributing to improved genotype-phenotype correlations.
2. **To explore the possible role of sarcomeric titin in the myocardial impairment observed in Marfan cardiomyopathy** by analyzing total titin levels and titin isoform expression in LV myocardial tissue from MFS patients using molecular biology techniques.

3. Methods

3.1. Experimental design

The research was elaborated and conducted in accordance with the Helsinki Declaration of 1975, amended in 2013. Ethical approval for the harvesting and use of human tissues and the use of genomic data was obtained from the Medical Research Council of Hungary (ethical permission numbers: TUKEB 73/2005, ETT TUKEB 7891/2012/EKU (119/PI/12.), ETT TUKEB 12751-3/2017/EKU, ETT TUKEB IV/10161-1/2020/EKU, and ETT TUKEB BM/17671-3/2024). All patients provided their informed consent prior to inclusion in the study.

The participants were selected based on the following inclusion criteria:

1. Marfan syndrome (MFS) group (n = 10):
    a. Genetically confirmed diagnosis of MFS through the detection of a (likely) pathogenic *FBN1* variant;
    b. Undergoing aortic root surgery for MFS-related aortic complications (i.e., aortic root aneurysm, annuloaortic ectasia);
    c. Age ≥ 15 years.
2. Non-Marfan syndrome/control group (n = 10):
    a. Medical history unsuggestive of connective tissue disorders or aortic disease;
    b. Undergoing orthotopic heart transplantation due to cardiac failure of ischemic etiology;
    c. Age ≥ 15 years.
3. Marfan syndrome group within the titin study (n = 12):
    a. Genetically confirmed diagnosis of MFS through the detection of a (likely) pathogenic *FBN1* variant;
    b. Undergoing aortic root surgery for MFS-related aortic complications (i.e., aortic root aneurysm, annuloaortic ectasia);
    c. Any age.

A total of 32 patients were included across two studies (i.e., fibrillin-1 and titin studies). All surgical interventions took place at the Heart and Vascular Center of Semmelweis University. The clinical data of the participants were obtained from the

databases of the Hungarian Marfan Register [155] and the Transplantation Biobank of the Heart and Vascular Center of Semmelweis University.

3.2. Fibrillin-1 study

Aortic root tissue samples were collected from 10 MFS patients (labeled MFS1–MFS10) and 10 non-MFS control individuals (labeled C1–C10). The tissue was received as pieces cut from above the sinuses of Valsalva. Following removal, the specimens were immediately immersed in 0.9% saline solution and transported on ice to the Department of Biophysics and Radiation Biology of Semmelweis University, where they were stored at 4°C until being processed within 48 hours of collection.

3.2.1. Fibrillin-1 microfibril purification

The microfibril isolation protocol was conducted as previously described [37], based on an adapted version of an earlier methodology [156,157]. All reagents and materials were purchased from Sigma-Aldrich (St. Louis, MO, USA).

Following the careful removal of adipose tissue from the adventitia, a full-thickness aortic wall piece weighing roughly 1 gram was prepared for purification. The tissue was cut up into fine pieces and then homogenized in 5 mL of 0.05 M Tris-HCl buffer (pH 7.4) containing 0.4 M NaCl, 0.01 M $CaCl_2$, 0.01% NaN_3, and protease inhibitors, namely 10 mM N-ethylmaleimide and 2 mM phenylmethylsulfonyl fluoride (PMSF), using a handheld, blade-type homogenizer. 5 mg of type 1A bacterial collagenase was added to the tissue suspension, and the digestion was allowed to proceed for 4 hours at room temperature (around 22°C) with gentle stirring. The digestion process was terminated by adding 100 µL ethylenediaminetetraacetic acid (EDTA), and the homogenate was centrifuged at a relative centrifugal force of 10,000 g for 30 minutes. The excluded supernatant (labeled “low salt extract”) was filtered using a 0.22 µm syringe filter unit and stored at 4°C. The pellet was resuspended in 5 mL of 0.05 M Tris-HCl buffer (pH 7.4) containing 1 M NaCl, 10 mM EDTA, 0.01% NaN_3, and protease inhibitors (10 mM N-ethylmaleimide, 2 mM PMSF), and left to extract for 48 hours at 4°C with gentle stirring. After centrifugation at 10,000 g for 30 minutes, the supernatant (labeled “high salt extract”) was filtered and stored as described previously. The extracts underwent size-exclusion chromatography at room temperature on a Sepharose CL-2B column (150 x 1.5 cm) in 0.05 M Tris-HCl buffer (pH 7.4) containing 0.4 M NaCl and

0.01% NaN_3. The column eluate corresponding to the chromatogram peaks was collected in the form of 1 mL fractions. All pooled fractions were further investigated for protein concentration by measuring ultraviolet light absorbance at 280 nm using a NanoDrop 1000 spectrophotometer (Thermo Fisher Scientific, Waltham, MA, USA). Aliquots from the fractions with the highest protein concentrations were selected for AFM imaging.

3.2.2. Atomic force microscopy imaging

AFM is a high-resolution imaging technique widely used in nanoscience to visualize and manipulate materials at the nanoscale. It employs a sharp probe (tip) mounted on a flexible cantilever to scan the surface of a sample (**Figure 3**). As the tip moves across the sample surface, intermolecular forces between the tip and the sample cause the cantilever to deflect. Using a laser beam focused on the surface of the cantilever and reflected onto a photodetector, this deflection is recorded and converted into three-dimensional topographical images of the scanned surface, showing height differences at (sub)nanometer resolution. This mechanism is characteristic of the non-contact/tapping mode of AFM scanning, where the tip oscillates just above the sample surface, measuring attractive forces without touching it, and is more suitable for soft biological materials in order to minimize damage. Beyond imaging, AFM can perform force spectroscopy, where the probe indents the sample to measure local mechanical properties such as stiffness (Young's modulus), elasticity, and adhesion forces [158].

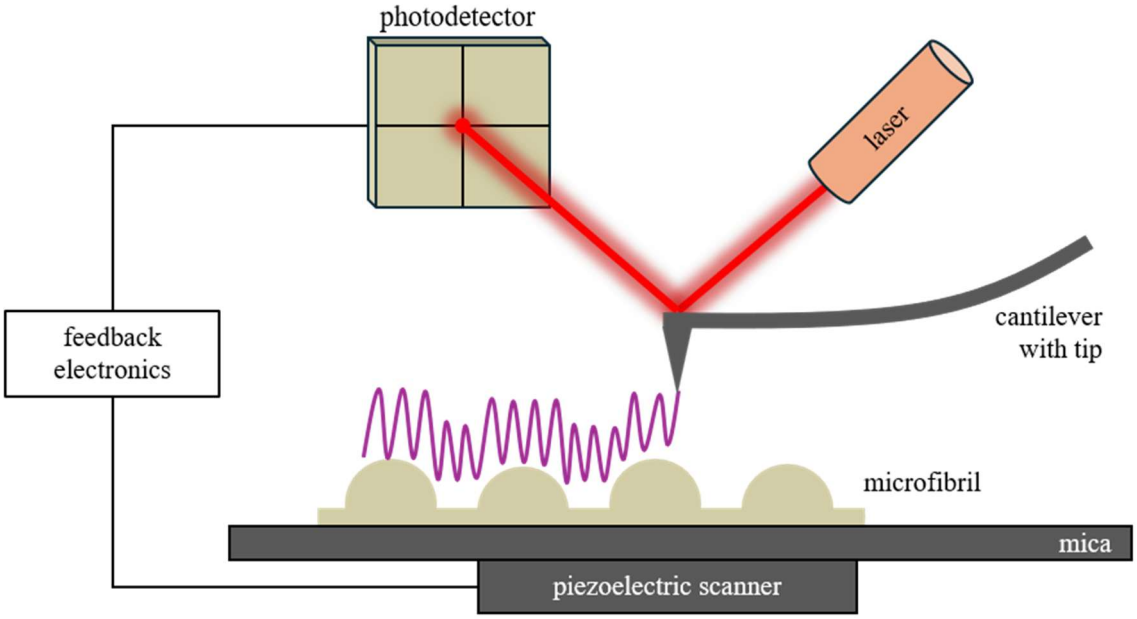

Figure 3. Schematic representation of the main components of an AFM.

AFM is especially suitable for biological samples due to its ability to operate both in air and in aqueous environments, enabling the investigation of hydrated, soft, and dynamic systems in near-physiological conditions. It requires minimal sample preparation or fixation, preserving the native state of biological structures [158].

3.2.2.1. Morphological measurements

Aliquots were diluted with chromatographic buffer based on the spectrophotometric readings when necessary. 20 μL from the obtained suspension were pipetted onto a freshly cleaved mica surface and allowed to equilibrate for 15 minutes before being rinsed with ultrapure water and dried using gentle high-purity nitrogen gas stream.

To assess microfibrillar morphology, probe scanning was performed with an Asylum Research Cypher ES AFM (Oxford Instruments, Santa Barbara, CA, USA) at room temperature. Topographical images (height data) were recorded in tapping mode, employing OMCL-AC160TS-R3 microcantilevers (Olympus Corporation, Shinjuku City, Tokyo, Japan) with force constant of 26 N/m and resonance frequency of 300 ± 100 kHz. Scanning was conducted at a typical setpoint of 700 mV and image resolution of 512 x 512 pixels. Image processing and data analysis were carried out using the Igor Pro 6 environment (WaveMetrics, Lake Oswego, OR, USA) and the open-source Gwyddion software [159].

The morphological analysis of individual fibrillin-1 microfibrils focused firstly on a detailed characterization of the bead regions. Measured parameters included maximum and average height, length, width, projected area, volume, bead roundness, and aspect ratio. In addition, microfibril length, interbead segment height, and periodicity were assessed [37]. Following the individual assessment of each sample, comparative analyses were performed between the MFS and control groups. Within the MFS cohort, subgroup comparisons were carried out between patients harboring HI and DN *FBN1* mutations and between each subgroup and the control group to investigate genotype-specific effects on microfibril properties.

3.2.2.2. Mechanical measurements

Force spectroscopy was carried out in liquid (chromatographic buffer) at room temperature. The mica substrate had been affixed to the bottom of a small petri dish in order to allow complete immersion of the scanning surface, minimizing evaporation during measurements. The mica was first coated with 100 µL of poly-L-lysine and incubated for 20 minutes. It was then rinsed with ultrapure water and dried using nitrogen gas. Sample aliquots (100 µL) were applied to the mica surface and allowed to equilibrate for 15 minutes. After incubation, the surface was gently washed five times with chromatographic buffer using pipette aspiration, and finally covered with 1.5 mL of the same buffer to maintain full coverage during measurements.

The stiffness of fibrillin-1 microfibril beads was investigated with a DriveAFM instrument (Nanosurf AG, Liestal, Switzerland) using BL-AC40TS cantilevers (Olympus Corporation, Shinjuku City, Tokyo, Japan) with force constant of 0.1 N/m and resonance frequency of 110 ± 35 kHz. Cantilever calibration was conducted using the thermal method prior to imaging. Force mapping was performed in static mode at a setpoint force of 500 pN. Young's modulus values were determined by fitting the Hertzian mechanics model to the approach segment of the recorded force-distance curves in the integrated Nanosurf Studio 12 software (Nanosurf AG, Liestal, Switzerland), assuming a conical indenter geometry and Poisson's ratio of 0.25. The generated height and Young's modulus maps were exported and further processed using Gwyddion.

As with the morphological measurements, equivalent comparisons were conducted between groups and within the MFS subgroups.

3.3. Titin study

Human myocardial tissue samples were sourced from the Transplantation Biobank of the Heart and Vascular Center of Semmelweis University. LV septal endomyocardium specimens had been collected from 12 MFS patients (labeled PAP, in accordance with the identification codes (ID) given in the Transplantation Biobank database) undergoing aortic root surgical interventions. Following excision, the samples were immediately snap-frozen in liquid nitrogen under sterile conditions and stored at -80°C until analysis [160]. Additionally, myocardial samples from two DCM patients (labeled DCM) without titin truncating variants (*TTN*tv-) [161] and one adult male Wistar

rat (labeled HK9) were included in the analysis as control and reference specimens. Previously investigated *TTN*tv- DCM specimens [161] were used for comparison.

3.3.1. Protein solubilization

The solubilization protocol followed an earlier established method [161]. The small LV myocardial fragments (10–15 mg) were homogenized in glass Kontes Dounce tissue grinders under liquid nitrogen. After a 20-minute incubation at -20°C, the samples were solubilized at 60°C for 15 minutes in a 50% urea buffer (8 M urea, 2 M thiourea, 50 mM Tris-HCl, 75 mM dithiothreitol, 3% sodium dodecyl sulfate (SDS), and 0.03% bromophenol blue, pH 6.8) and 50% glycerol supplemented with protease inhibitors (0.04 mM E64, 0.16 mM leupeptin, and 0.2 mM PMSF). Following solubilization, the samples were centrifuged at 16,000 g for 5 minutes, aliquoted, snap-frozen in liquid nitrogen, and stored at -80°C.

3.3.2. Titin isoform analysis

Titin expression levels were assessed using 1% SDS-agarose gel electrophoresis, conducted at 16 mA per gel for 3.5 hours [160,161]. The gels were stained overnight with SYPRO Ruby Protein Gel Stain (Thermo Fischer Scientific, Waltham, MA, USA) before being digitized with a Typhoon laser scanner (Amersham Biosciences, Amersham, UK). The optical density of the titin bands was analyzed using the ImageJ software (National Institutes of Health, Bethesda, MD, USA). These data were further used to calculate the relative titin isoform ratio (N2BA:N2B ratio). The relative content of full-length titin (T1), which included N2BA and N2B, and titin's proteolytic degradation product (T2), were normalized to the myosin heavy chain (MHC). The total titin (TT) amount, representing the sum of T1 and T2, was also normalized to MHC.

3.3.3. Titin truncated protein detection

To confirm whether the additional bands observed on the gel represented truncated titin fragments, Western blot analysis was performed [139,160,161]. Protein samples were separated on a 0.8% SDS-agarose gel and transferred onto a Hybond LFP polyvinylidene fluoride membrane (Amersham Biosciences, Amersham, UK) using a Trans-Blot Cell semi-dry electrophoretic transfer system (Bio-Rad Laboratories, Hercules, CA, USA). The membranes were incubated overnight at 4°C with two primary antibodies targeting titin's termini: anti-T12, targeting the N-terminal region (obtained

from the University of Bonn, Germany; dilution 1:1,000), and anti-M8M10, targeting the C-terminal region (Myomedix, GmbH, Neckargemünd, Germany; dilution 1:1,000). This was followed by incubation with CyDye-conjugated secondary antibodies (Amersham Biosciences, Amersham, UK). Blots were visualized using a Typhoon laser scanner, and relative protein expression levels were quantified using the ImageJ software. The truncated proteins detected on the gels were normalized to T1.

3.4. Statistical analysis

Statistics were performed using GraphPad Prism 8 (GraphPad Software, Boston, MA, USA). Outliers were identified and excluded using the ROUT method (Q = 1%). For pooled group analysis, all original data points were included, and outliers were re-evaluated within each group using the same criteria. The normality of data was assessed either with the Shapiro-Wilk test or the Anderson-Darling test, depending on dataset sizes. The data are reported as mean with SD or median with Q1–Q3 interquartile range (IQR). For comparisons between two groups, the unpaired Student's t-test with Welch's correction in cases of unequal variances, or the Mann-Whitney U test was applied. Categorical variables were compared using Fisher's exact test. For comparisons involving more than two groups, the Kruskal-Wallis test was used, followed by Dunn's post hoc test with correction for multiple comparisons. Correlations were tested using either the Pearson or Spearman test, depending on data distribution; corresponding regression lines were plotted to visualize linear relationships. The results were considered significant at a *P* value of less than 0.05.

4. Results

4.1. Fibrillin-1 study

4.1.1. Study population

Tables 3 and **4** present the relevant general and clinical characteristics (including atherosclerotic risk factors) and preoperative echocardiographic findings in the two patient groups, including the revised Ghent diagnostic criteria [14] for the MFS cohort. **Table 5** summarizes the specific genetic mutations identified in the MFS patient cohort. MFS patients were significantly younger (34.1 ± 12.7 years vs. 56.5 ± 7.0 years, $P < 0.001$) and had lower body mass index (BMI) (23.3 ± 5.9 kg/m^2 vs. 27.5 ± 2.7 kg/m^2, $P = 0.026$) at the time of surgery. The control group had a higher prevalence of certain atherosclerotic risk factors, namely hyperlipidemia ($P = 0.006$) and diabetes mellitus ($P = 0.033$). No significant differences were observed regarding the prevalence of hypertension ($P = 0.087$), smoking ($P = 0.350$), and obesity (BMI > 30.0) ($P > 0.999$) in the two patient groups. In the MFS cohort, the mean diameters of the aortic annulus, sinuses of Valsalva, and ascending aorta were 24.9 ± 2.9 mm, 49.6 ± 8.8 mm, and 42.7 ± 8.0 mm, respectively. Comprehensive preoperative echocardiographic assessments were unavailable for most control patients, owing to the absence of recent imaging or incomplete records.

Table 3. General characteristics and preoperative echocardiographic data of the control group subjects. Present features are marked with "+". Symbols: ♀, female; ♂, male.

Control sample ID	**C1**	**C2**	**C3**	**C4**	**C5**	**C6**	**C7**	**C8**	**C9**	**C10**
Age	66	56	67	52	52	43	57	55	56	61
Sex	♂	♂	♂	♀	♂	♂	♀	♂	♂	♀
BMI (kg/m^2)	29.1	27.8	24.6	25.0	26.3	30.1	28.7	30.6	22.6	29.9
Risk factors for atherosclerosis										
Hypertension	+	+	+	+	+	+	+	+	+	+
Hyperlipidemia	+	+			+	+	+	+	+	+
Diabetes mellitus	+	+		+				+	+	
Smoking	+	+			+		+			+
Obesity						+		+		
Preoperative echocardiographic findings										
Aortic root diameter (mm)		17	28		21					29
Ascending aortic diameter (mm)		28		28	27	37	32			37

Table 4. Overview of the key characteristics in the studied MFS cohort. For each patient, present features are marked with "+". Symbols: ♀, female; ♂, male.

MFS sample ID	**MFS1**	**MFS2**	**MFS3**	**MFS4**	**MFS5**	**MFS6**	**MFS7**	**MFS8**	**MFS9**	**MFS10**
Age	37	17	36	44	28	16	29	50	54	30
Sex	♀	♂	♀	♀	♂	♂	♂	♂	♂	♂
BMI (kg/m^2)	23.4	16.1	27.8	24.0	21.3	26.0	32.9	23.8	26.0	11.9
Risk factors for atherosclerosis										
Hypertension	+		+			+	+	+		+
Hyperlipidemia								+		
Diabetes mellitus										
Smoking								+		+
Obesity							+			
Preoperative echocardiographic findings										
Aortic root diameter (mm)	20	26	21	25		26	29	25	24	28
Sinus Valsalva diameter (mm)	48	49	41	50	52	46	46	73	47	44
Ascending aortic diameter (mm)	46	56	33	37	48	39	40		34	51
MFS-specific diagnostic criteria (revised Ghent nosology [14])										
FBN1 mutation	+	+	+	+	+	+	+	+	+	+
Family history	+		+	+		+	+		+	
Aortic involvement	+	+	+	+	+	+	+	+	+	+
Ectopia lentis			+		+				+	+
Systemic involvement	+	+	+	+	+	+			+	+
Systemic score	**9**	**8**	**9**	**7**	**8**	**7**	**6**	**2**	**8**	**7**
Wrist sign	+	+	+	+	+	+			+	+
Thumb sign	+	+	+	+	+	+			+	
Pectus carinatum		+	+	+			+		+	+
Pectus excavatum or deformity	+				+	+		+		
Hindfoot deformity							+		+	
Pes planus	+	+	+			+				+
Reduced US/LS and increased arm span/height ratios with no severe scoliosis		+								
Scoliosis or thoracolumbar kyphosis	+		+	+	+	+		+	+	+
Dolichocephaly	+									
Enophthalmos										+
Downslanting palpebral fissures		+			+					+
Malar hypoplasia										
Retrognathia	+		+		+					
Skin striae	+		+	+	+	+	+		+	+
Myopia > 3 diopters	+		+		+		+			+
Mitral valve prolapse	+	+		+	+					

Table 5. *FBN1* variants identified in the MFS cohort.

*according to published literature, the Universal Mutation Database (UMD) [162], or the Universal Protein resource (UniProt) [163]; **where a publication was not found, the Single Nucleotide Polymorphism Database (National Center for Biotechnology Information, Bethesda, MD, USA) identifier was used.

Patient ID	Nucleotide change	Exon	Amino acid substitution	Protein domain*	Mutation effect	Mutation type	Variant classification	Reports**
MFS1	c.1665C>A	13	p.Cys555Ter	cbEGF4	nonsense	HI	pathogenic	this study; rs531101773
MFS2	c.5671+1G>A	intron 46	–	cbEGF28	splice site	HI	pathogenic	this study; rs112104270
MFS3	c.6313+1G>T	intron 51	–	TB6	splice site	HI	pathogenic	Comeglio P *et al.* [164]
MFS4	c.2988T>A	25	p.Cys996Ter	TB5	nonsense	HI	likely pathogenic	this study; rs1555398803
MFS5	c.6032G>C	49	p.Cys2011Ser	cbEGF30	missense	DN	pathogenic	Madar L *et al.* [165]
MFS6	c.7583G>T	62	p.Cys2528Phe	cbEGF40	missense	DN	pathogenic	Yum HR *et al.* [166]
MFS7	c.4472G>T	37	p.Cys1491Phe	cbEGF22	missense	DN	likely pathogenic	Lebreiro A *et al.* [167]
MFS8	c.7564_7566delinsAGA	61	p.Cys2522Arg	cbEGF39	missense	DN	likely pathogenic	this study
MFS9	c.3373C>T	28	p.Arg1125Ter	cbEGF13	nonsense	HI	pathogenic	Comeglio P *et al.* [164]; Rommel K *et al.* [168]; Attanasio M *et al.* [169]; Hung CC *et al.* [170]; Magyar I *et al.* [171]
MFS10	c.401G>A	5	p.Cys134Tyr	EGF2	missense	DN	pathogenic	Howarth R *et al.* [172]; Baudhuin LM *et al.* [173]

Among the 10 MFS individuals, a diverse spectrum of (likely) pathogenic *FBN1* mutations was identified, including five missense, three nonsense, and two splice site variants (**Table 5**). Four variants were presumably *de novo*; one of them was novel and had not been previously reported in public variant databases or the scientific literature. Namely, in patient MFS8, the missense mutation c.7564_7566delinsAGA, leading to the amino acid substitution p.Cys2522Arg, was detected. This variant was classified as likely pathogenic and was found in a 50-year-old male who met the diagnostic criteria for MFS based on aortic involvement and the confirmed genetic mutation. At the same time, the fulfillment of systemic features, *ectopia lentis*, and family history were absent.

4.1.2. Fibrillin-1 microfibril purification and AFM imaging

Chromatographic separation of collagenase-digested aortic extracts showed characteristic elution profiles indicative of both high-molecular-weight aggregates and smaller soluble components [157]. Both low and high salt extracts exhibited two prominent peaks (**Figure 4**). Initial AFM imaging revealed that the first peak contained predominantly fibrillin-1 microfibrils and thinner collagen VI filaments, whereas the second peak consisted largely of densely aggregated, poorly visualizable material. High salt extraction yielded a relatively larger quantity of fibrillin-1 microfibrils than the low salt extract. Therefore, all AFM analyses were conducted on fractions from the first peak of the high salt extract chromatogram.

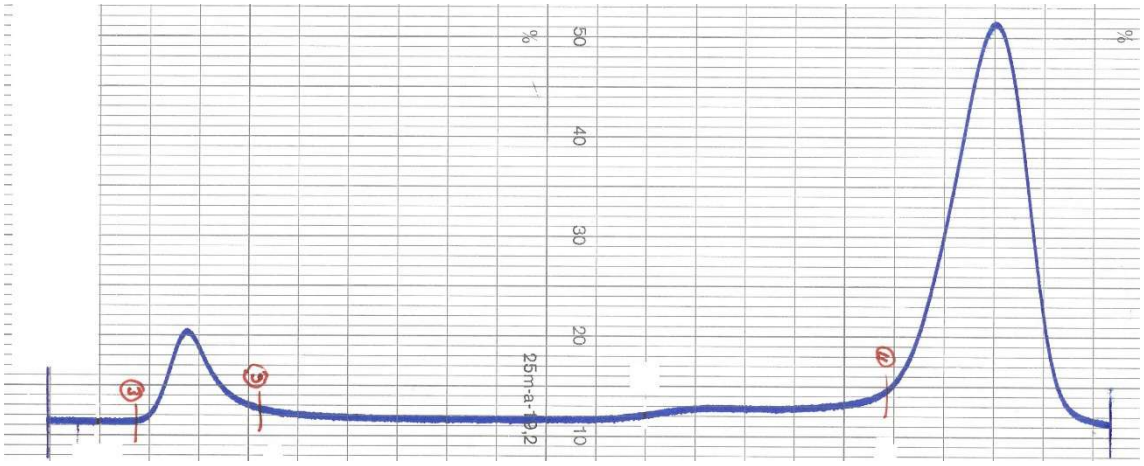

Figure 4. Typical profile of a chromatogram (MFS6, high salt extract).

AFM visualization revealed fibrillin-1 microfibrils with conserved aspect across all samples, irrespective of pathological status (**Figure 5A**). Their typical "beads-on-a-string" appearance was dominated by globular beads connected by filamentous interbead

regions. The interbead regions often presented as multiple thin “arms” bridging adjacent beads. Additionally, most beads displayed thread-like lateral projections extending from their surface (**Figure 5B**) [37].

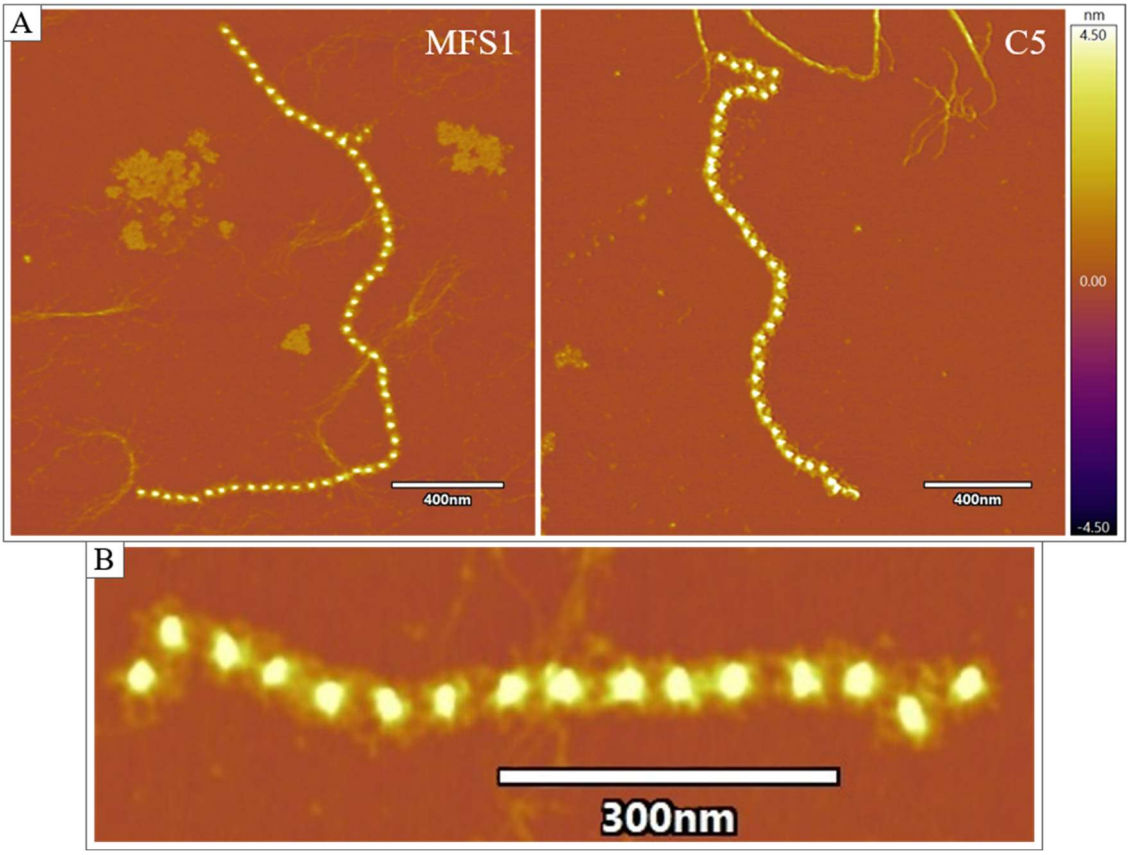

Figure 5. AFM imaging of fibrillin-1 microfibrils. **A.** Microfibrils isolated from MFS and control aorta. **B.** Zoomed-in aspect of a fibrillin-1 microfibril, showing bead and interbead details, and lateral projections.

4.1.2. Morphological assessment

To quantitatively assess the morphology of fibrillin-1 microfibrils, we developed a customized image analysis workflow. Initial measurements were performed in Igor Pro 6 along two orthogonal axes: microfibril length, bead length, and periodicity were analyzed along the longitudinal axis of the microfibrils, while bead width and maximum interbead height were measured laterally. Bead length and width were defined as the full width at half maximum of the respective height profiles (**Figure 6**). Microfibril length was measured as the axial distance between the peaks of the first and last beads. For advanced morphological characterization, we used Gwyddion, where individual beads were segmented using Otsu’s thresholding method, enabling objective and standardized bead selection while excluding interbead regions. From these segmented beads, we

extracted data on their maximum and average height, projected area, and volume. Additionally, bead roundness was computed as the ratio between the largest inscribed and the smallest circumscribed circle diameters, and bead aspect ratio was calculated as the width-to-length ratio, providing a comprehensive quantification of bead geometry.

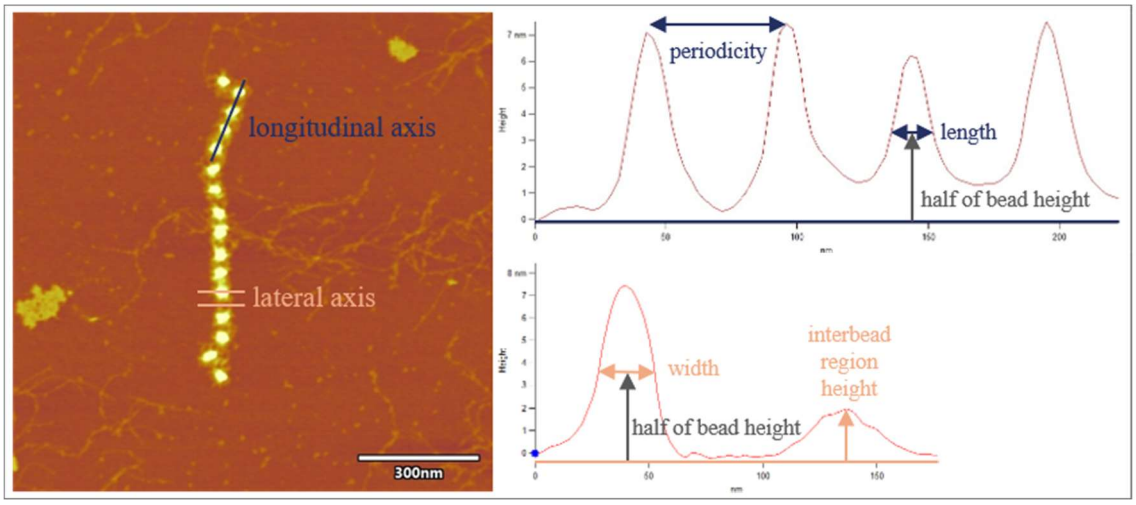

Figure 6. Workflow of the morphological analysis of fibrillin-1 microfibrils performed in Igor Pro 6, where parameters were measured along two perpendicular axes of the height profile.

For each sample, around 200 bead repeats were included. Only microfibrils exhibiting a relatively linear disposition and free from entanglement with other structures were selected for analysis. In total, 4,370 beads from 176 individual fibrillin-1 microfibrils were analyzed, comprising 98 microfibrils with 2,229 beads in the MFS group and 78 microfibrils with 2,141 beads in the control group. The results of the bead-specific parameters for each sample are summarized in **Table 6**. Interbead region height and periodicity data are detailed in **Table 7** and **Figure 7**.

Table 6. Values of measured bead parameters for each sample. For consistency, all variables are reported as median with IQR, regardless of distribution.

Sample ID	Maximum height (nm)	Average height (nm)	Length (nm)	Width (nm)	Projected area (nm^2)	Volume (nm^3)	Roundness	Aspect ratio
MFS1	7.46 (6.86–8.27)	4.26 (3.83–5.06)	18.1 (16.4–19.8)	18.6 (17.0–20.4)	640 (487–799)	2,773 (2,327–3,227)	0.64 (0.58–0.68)	1.02 (0.91–1.19)
MFS2	8.70 (7.74–9.81)	5.20 (4.51–6.37)	16.9 (14.6–18.4)	18.4 (16.6–19.6)	586 (489–705)	3,015 (2,467–3,882)	0.63 (0.58–0.69)	1.10 (0.96–1.27)
MFS3	7.19 (6.56–7.64)	4.49 (4.27–4.74)	18.9 (16.4–21.2)	20.5 (18.5–23.2)	597 (493–754)	2,726 (2,215–3,400)	0.64 (0.58–0.70)	1.08 (0.92–1.30)
MFS4	9.13 (8.22–10.00)	5.77 (5.00–6.45)	18.9 (17.5–20.1)	19.5 (18.2–20.9)	653 (551–752)	3,571 (3,144–4,009)	0.66 (0.60–0.69)	1.04 (0.93–1.13)
MFS5	8.24 (7.63–9.07)	4.36 (4.12–4.68)	18.8 (16.9–20.6)	19.6 (17.9–22.0)	700 (593–818)	3,132 (2,602–3,663)	0.63 (0.57–0.67)	1.04 (0.92–1.25)
MFS6	8.20 (7.67–8.72)	4.87 (4.45–5.36)	19.2 (17.8–20.7)	19.7 (18.3–21.7)	725 (637–820)	3,438 (2,967–4,078)	0.59 (0.54–0.64)	1.03 (0.93–1.15)
MFS7	7.49 (6.79–8.14)	4.94 (4.39–5.51)	19.4 (18.0–21.3)	20.9 (19.2–22.4)	651 (570–782)	3,343 (2,725–4,023)	0.69 (0.64–0.73)	1.07 (0.95–1.17)
MFS8	10.3 (9.68–10.8)	6.26 (5.92–6.83)	19.1 (17.7–20.5)	19.9 (18.4–21.5)	573 (496–669)	3,633 (3,136–4,278)	0.67 (0.62–0.71)	1.04 (0.92–1.16)
MFS9	9.06 (8.38–10.4)	5.83 (5.41–6.69)	19.5 (18.3–20.9)	20.3 (18.9–21.7)	601 (522–668)	3,549 (3,022–4,133)	0.67 (0.62–0.71)	1.04 (0.93–1.14)
MFS10	6.44 (5.87–7.07)	3.64 (3.43–3.94)	19.3 (18.0–20.1)	19.9 (18.8–20.9)	972 (853–1,144)	3,534 (3,079–4,157)	0.66 (0.61–0.71)	1.04 (0.97–1.10)
C1	6.35 (5.89–6.95)	3.76 (3.52–4.05)	23.6 (22.7–24.2)	23.7 (22.9–24.4)	1,090 (943–1,286)	4,102 (3,319–5,096)	0.71 (0.67–0.74)	1.01 (0.97–1.05)
C2	7.82 (7.22–8.34)	4.31 (3.93–4.58)	23.0 (21.8–24.6)	23.7 (22.0–25.4)	976 (841–1,107)	4,076 (3,558–4,644)	0.64 (0.59–0.69)	1.03 (0.94–1.11)
C3	8.43 (7.80–9.16)	4.83 (4.48–5.10)	24.3 (22.4–26.0)	24.7 (23.5–26.2)	915 (804–1,082)	4,296 (3,576–5,383)	0.67 (0.63–0.71)	1.04 (0.93–1.12)
C4	9.24 (8.54–9.69)	5.38 (4.98–5.67)	23.3 (21.8–24.8)	24.2 (22.6–26.1)	898 (779–1,029)	4,780 (4,103–5,552)	0.63 (0.59–0.66)	1.04 (0.95–1.15)
C5	6.73 (6.29–7.48)	4.02 (3.72–4.66)	23.9 (22.7–25.2)	24.5 (23.5–25.7)	1,027 (881–1,181)	4,291 (3,549–4,961)	0.64 (0.60–0.68)	1.02 (0.96–1.10)
C6	7.40 (6.70–8.81)	4.40 (3.93–5.47)	23.1 (22.3–24.1)	23.4 (21.9–24.6)	922 (805–1,046)	4,188 (3,545–4,943)	0.66 (0.61–0.70)	1.00 (0.94–1.07)
C7	6.47 (6.01–7.16)	4.02 (3.83–4.39)	24.1 (23.0–25.2)	25.8 (24.2–27.2)	1,079 (897–1,236)	4,295 (3,653–5,073)	0.66 (0.62–0.70)	1.06 (0.98–1.15)
C8	5.51 (5.05–6.30)	3.53 (3.11–4.01)	23.5 (22.0–24.7)	24.4 (23.1–26.1)	1,189 (1,017–1,362)	4,084 (3,604–4,969)	0.67 (0.62–0.71)	1.04 (0.99–1.12)
C9	3.95 (3.65–4.19)	2.50 (2.37–2.66)	24.9 (23.7–26.3)	27.1 (25.4–28.6)	1,802 (1,630–1,996)	4,538 (4,043–5,026)	0.65 (0.61–0.70)	1.08 (1.00–1.15)
C10	6.95 (6.57–7.53)	3.68 (3.36–3.93)	23.3 (22.3–24.2)	23.7 (23.0–24.8)	1,153 (1,034–1,307)	4,218 (3,554–4,895)	0.63 (0.58–0.67)	1.01 (0.97–1.09)

Table 7. Maximum interbead region height and periodicity values for all included samples. For consistency, all variables are reported as median with IQR, regardless of distribution.

Sample ID	Interbead region height (nm)	Periodicity (nm)	Correlation analysis	
			Spearman's *r* value	*P* value
MFS1	1.10 (0.87–1.38)	52.4 (48.7–55.8)	-0.381	< 0.001
MFS2	1.06 (0.81–1.44)	49.9 (45.4–52.5)	-0.570	< 0.001
MFS3	1.09 (0.93–1.29)	55.0 (50.0–61.7)	-0.426	< 0.001
MFS4	1.28 (0.99–1.79)	52.7 (46.3–58.2)	-0.486	< 0.001
MFS5	1.33 (0.99–1.91)	52.3 (46.6–57.2)	-0.463	< 0.001
MFS6	1.66 (1.10–2.48)	48.1 (38.9–56.4)	-0.686	< 0.001
MFS7	1.43 (1.05–2.00)	49.3 (43.5–55.4)	-0.660	< 0.001
MFS8	1.39 (1.08–1.77)	51.2 (46.0–56.8)	-0.469	< 0.001
MFS9	1.17 (0.92–1.49)	52.7 (48.1–57.5)	-0.163	0.018
MFS10	1.74 (1.34–2.19)	50.8 (45.2–55.4)	-0.602	< 0.001
C1	1.44 (1.16–1.86)	54.3 (49.6–57.5)	-0.359	< 0.001
C2	1.21 (0.95–1.53)	52.7 (48.3–58.3)	-0.498	< 0.001
C3	1.25 (0.91–1.85)	52.8 (48.4–57.6)	-0.201	0.003
C4	1.45 (1.18–1.76)	52.8 (47.4–58.5)	-0.277	< 0.001
C5	1.37 (1.10–1.74)	50.7 (45.6–55.9)	-0.284	< 0.001
C6	1.39 (0.99–1.89)	53.0 (47.1–57.3)	-0.375	< 0.001
C7	1.26 (0.92–1.80)	54.7 (49.4–59.5)	-0.475	< 0.001
C8	1.67 (1.29–2.14)	53.7 (47.4–58.6)	-0.488	< 0.001
C9	1.60 (1.30–1.95)	52.8 (47.5–57.0)	-0.588	< 0.001
C10	1.63 (1.22–2.00)	51.1 (45.9–55.8)	-0.588	< 0.001

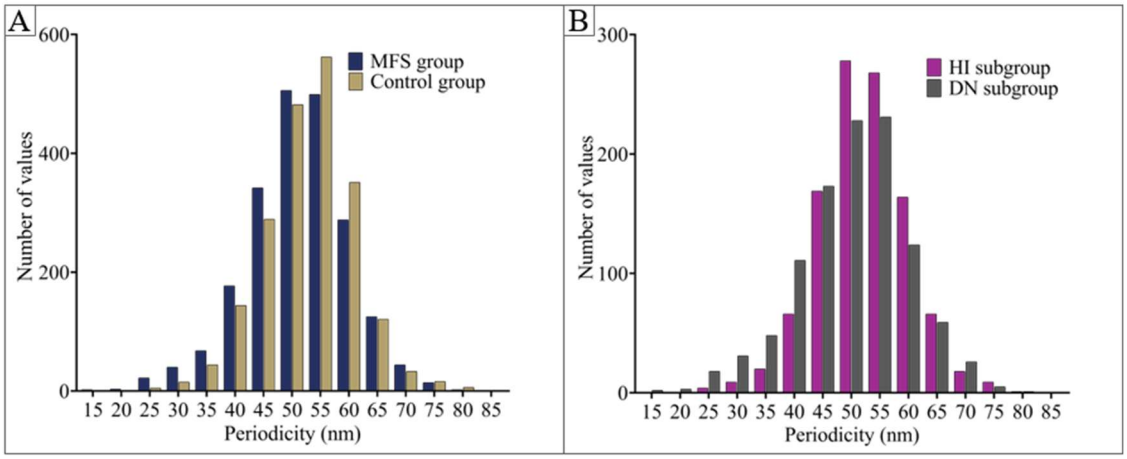

Figure 7. Distribution of fibrillin-1 microfibril periodicity across the MFS and control groups (**A**), and within the HI and DN subgroups (**B**).

The comparative analysis of fibrillin-1 microfibril morphology between MFS and control samples is illustrated in **Figure 8**, which displays results across the ten investigated structural parameters. **Figure 9** presents the results of the genotype-based

stratification**,** along with comparisons between each genetic subgroup and the control group, following the same parameter structure.

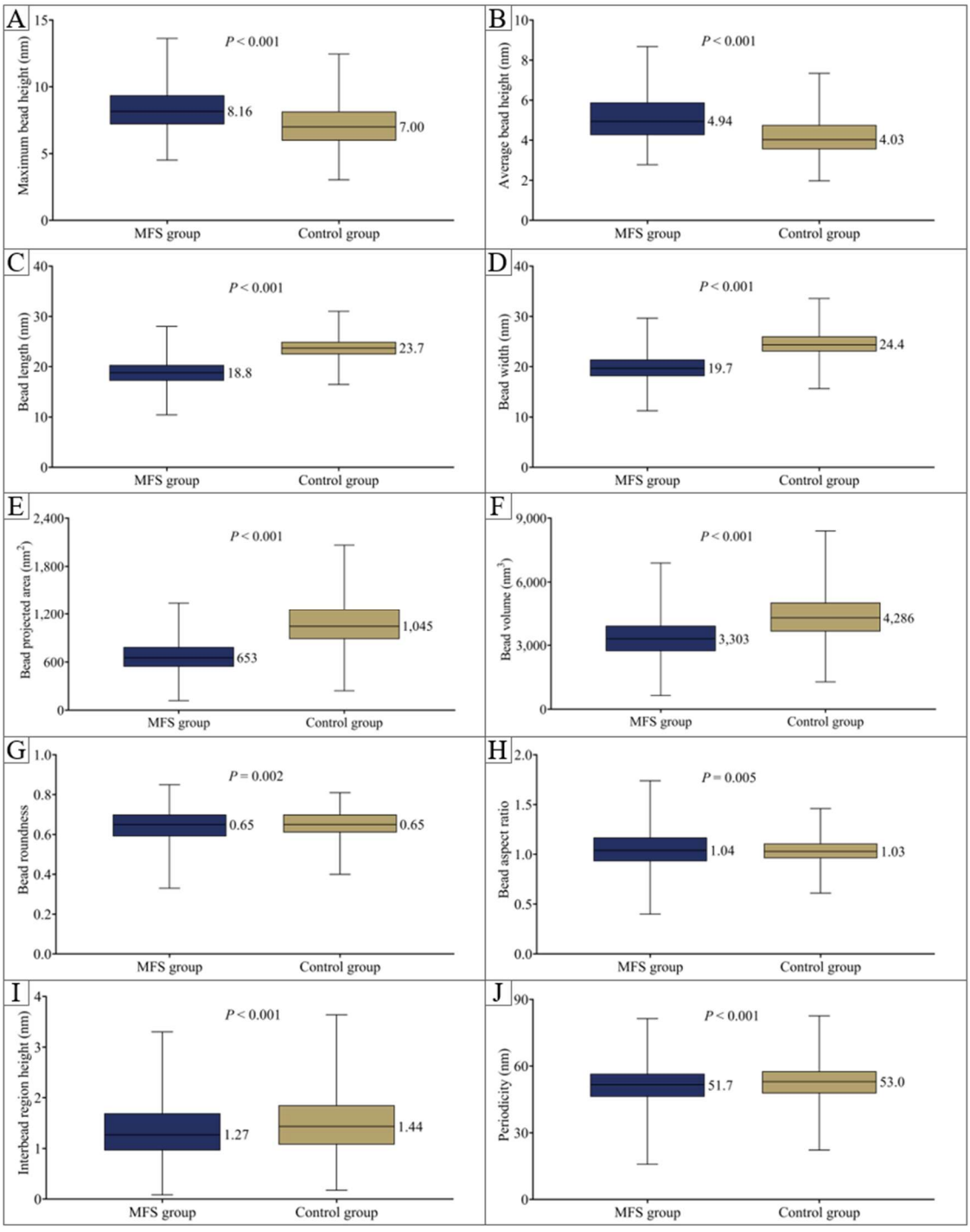

Figure 8. Comparative analysis of fibrillin-1 microfibril characteristics between MFS and control samples: maximum (**A**) and average (**B**) bead height, length (**C**), width (**D**), projected area (**E**), volume (**F**), roundness (**G**), and aspect ratio (**H**), interbead region height (**I**), and periodicity (**J**). Box plots display the median (horizontal line), IQR (box), and minimum-to-maximum values (whiskers). Median values are indicated next to each box.

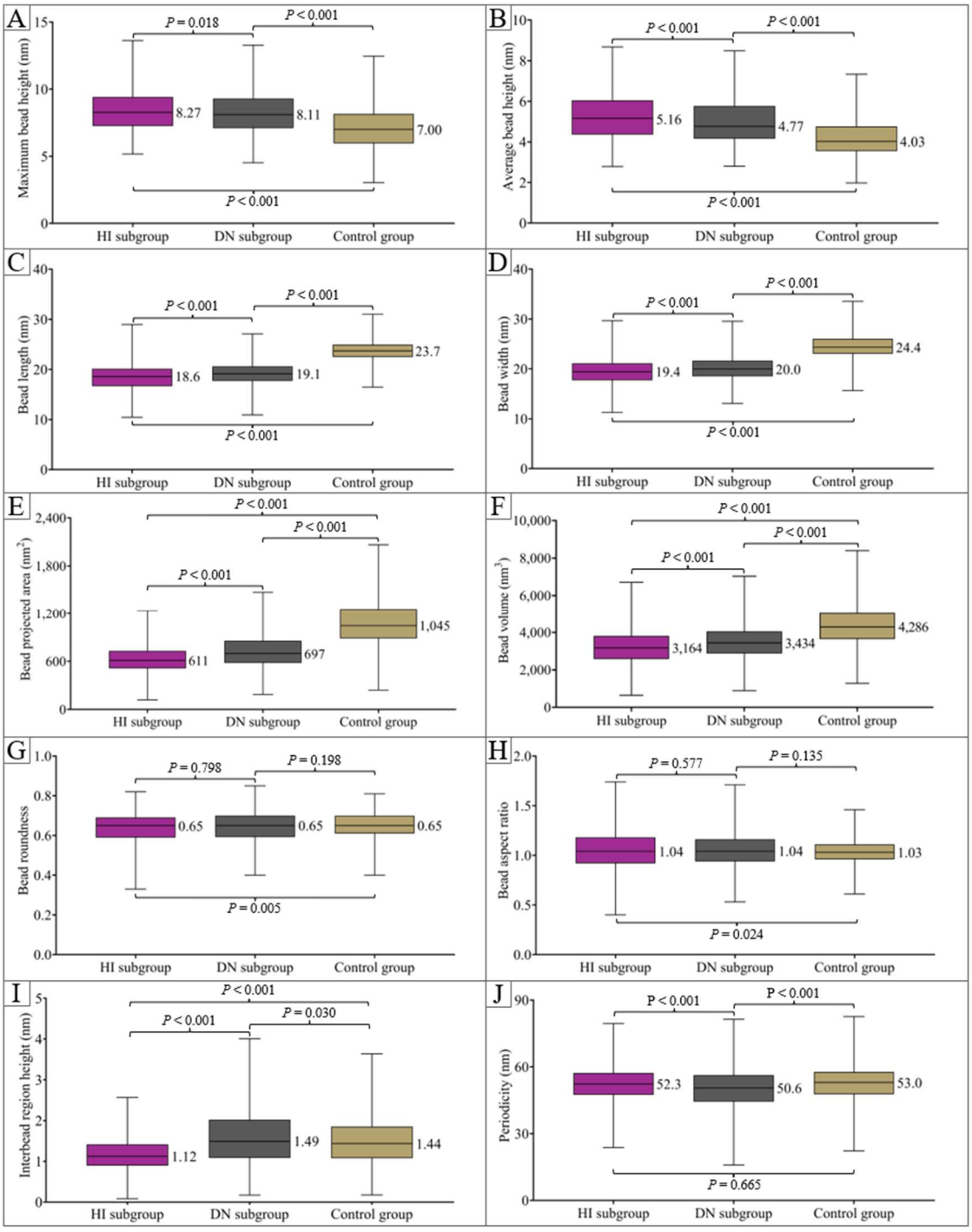

Figure 9. Genotype-based subgroup comparison of fibrillin-1 microfibril morphological parameters in MFS samples with HI and DN *FBN1* mutations, alongside comparisons with the control group: maximum (**A**) and average (**B**) bead height, length (**C**), width (**D**), projected area (**E**), volume (**F**), roundness (**G**), and aspect ratio (**H**), interbead region height (**I**), and periodicity (**J**). Box plots display the median (horizontal line), interquartile range (box), and minimum-to-maximum values (whiskers). Median values are indicated next to each box.

The length of purified individual microfibrils varied substantially, from short chains comprising only a few bead units to elongated assemblies reaching up to 15 μm, with most measuring around 0.5–2 μm [37]. The analysis performed on 1,010 microfibrillar assemblies yielded no significant differences in microfibril length between the MFS and control groups, nor between the HI and DN subgroups (**Figure 10**).

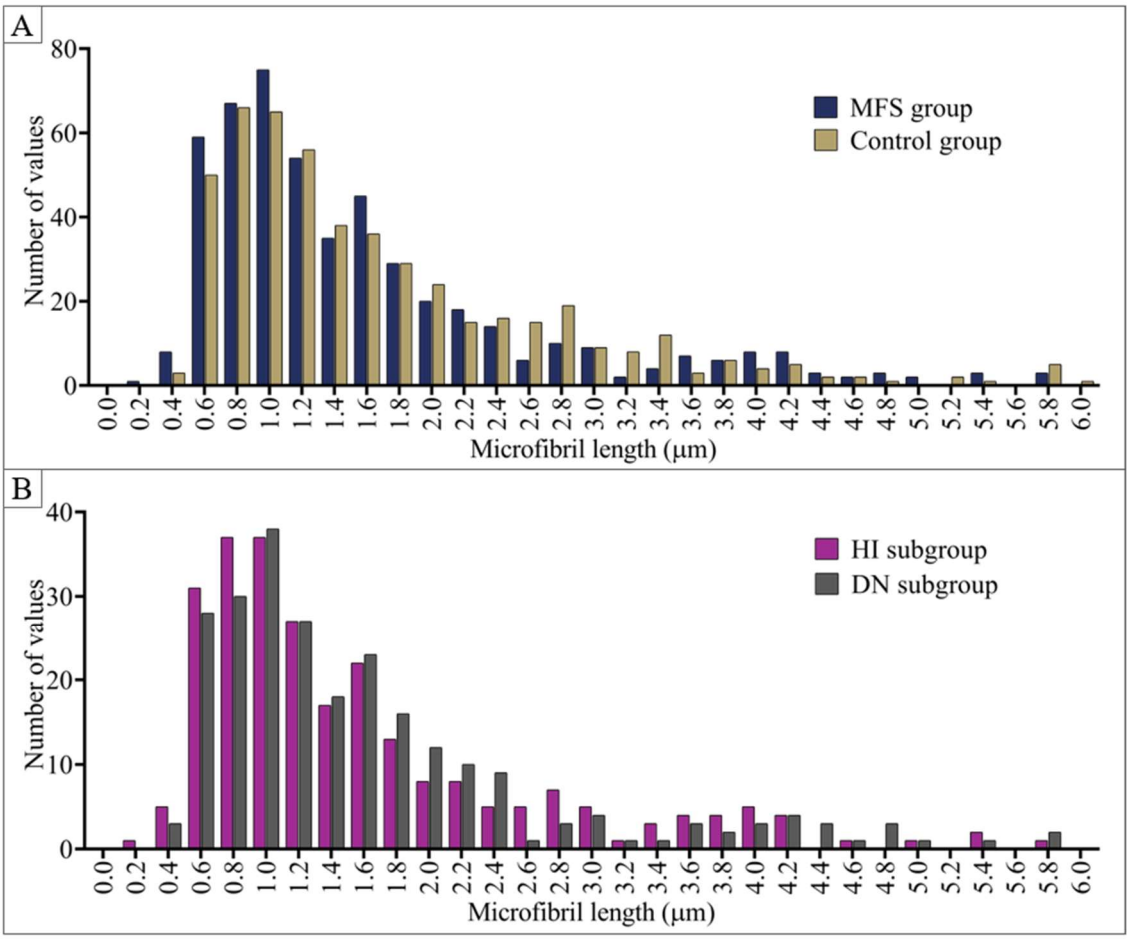

Figure 10. Fibrillin-1 microfibril length distribution within the MFS and control groups (**A**), and across the HI and DN subgroups (**B**).

4.1.3. Mechanical investigation

In force mapping AFM mode, a force-distance curve is acquired for each scanned pixel. Following a similar approach to the structural analysis, bead regions were identified on the corresponding height maps using Otsu's thresholding method in Gwyddion and subsequently mapped onto the Young's modulus images (**Figure 11**). Thus, 1–2 representative force curves were selected per bead, corresponding to their peaks.

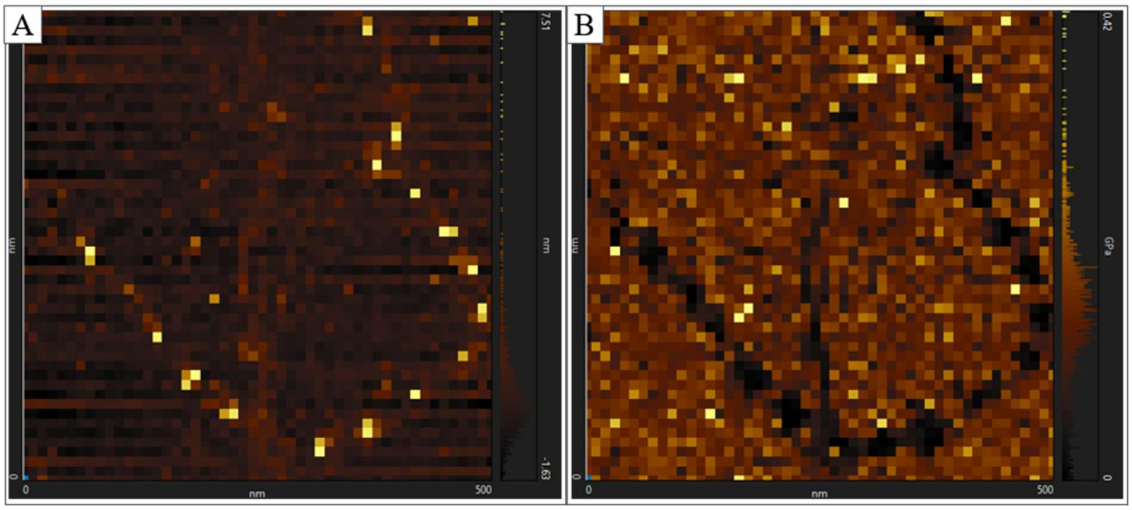

Figure 11. AFM force mapping. Height (**A**) and stiffness (**B**) maps of a fibrillin-1 microfibril.

A total of 3,930 beads were analyzed across 281 individual fibrillin-1 microfibrils, based on data extracted from over 7,000 recorded force-distance curves. **Table 8** summarizes the median Young's modulus and IQR for each sample.

Table 8. Young's modulus of fibrillin-1 microfibrils measured by AFM nanoindentation in individual samples.

Sample ID	Analyzed curves (n)	Young's modulus (MPa)	Sample ID	Analyzed curves (n)	Young's modulus (MPa)
MFS1	331	2.28 (1.52–3.32)	**C1**	322	3.40 (2.61–4.37)
MFS2	381	1.96 (1.37–2.73)	**C2**	382	2.53 (1.81–3.29)
MFS3	305	2.18 (1.60–3.10)	**C3**	431	2.63 (1.94–3.47)
MFS4	432	2.51 (1.92–3.17)	**C4**	348	2.70 (2.01–3.41)
MFS5	361	2.43 (1.71–3.39)	**C5**	203	2.75 (1.97–3.54)
MFS6	318	2.92 (2.17–3.73)	**C6**	315	2.67 (1.77–3.47)
MFS7	342	2.59 (2.05–3.13)	**C7**	325	2.63 (1.87–3.58)
MFS8	226	2.58 (1.81–3.62)	**C8**	304	2.75 (1.90–3.70)
MFS9	305	3.16 (2.44–4.05)	**C9**	217	3.12 (2.11–4.61)
MFS10	257	3.21 (2.35–4.57)	**C10**	373	3.00 (2.10–3.80)

Median Young's modulus values showed greater dispersion among MFS samples, indicating higher variability in bead stiffness. However, the distribution in the DN subgroup closely overlapped with that of the control group (**Figure 12A** and **B**). Overall, MFS samples exhibited a lower median Young's modulus than controls. In the HI subgroup, median Young's modulus was significantly lower than in both DN and control groups ($P < 0.001$). At the same time, there was no significant difference in bead stiffness between DN and control samples ($P = 0.327$) (**Figure 12C** and **D**).

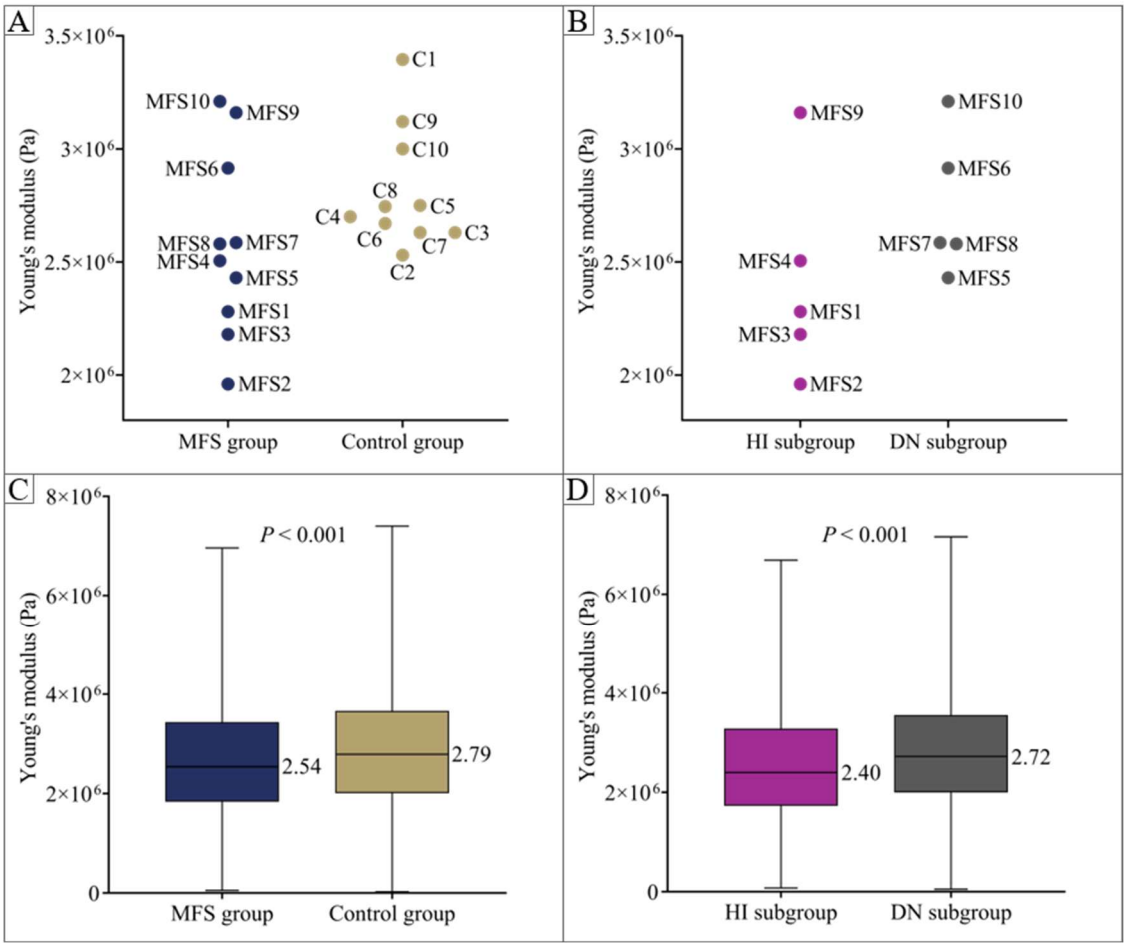

Figure 12. Scatter plots illustrating the distribution of median Young's modulus values calculated across the MFS and control groups (**A**), and between the HI and DN samples (**B**). Comparison between MFS and control groups (**A**), and between HI and DN subgroups (**B**) regarding median Young's modulus values and IQR. Median values are indicated next to each box.

During force spectroscopy measurements, a subset of approach curves displayed consistent indentation-like features ("steps" in the force signal), interpreted as indicative of disruptive tip-sample interactions at the bead surface. To analyze these events, the respective force-distance curves were extracted and processed using a custom Python script. First, the force data were smoothed using a rolling average with a window size of 15 data points to reduce noise. Indentation events were then identified using the find_peaks function from the SciPy library, applying the following parameters: prominence = 3×10^{-12} N and minimum peak height = 0.5×10^{-10} N. These values were chosen empirically based on exploratory analysis to ensure optimal sensitivity for detecting small but distinct deflections while minimizing false positives due to noise. Force values corresponding to the detected peaks were recorded for statistical analysis

(**Figure 13**). Only curves with well-defined indentation peaks were retained for quantitative evaluation.

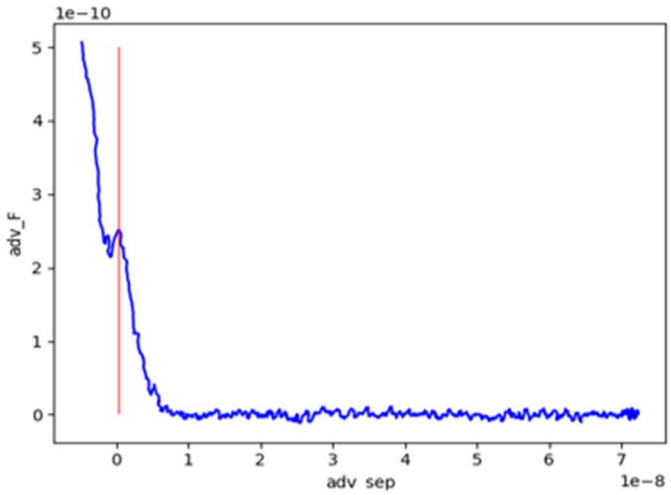

Figure 13. Python force-distance curve analysis: smoothed approach segment displaying characteristic indentation, with indentation peak marked (red line).

All force-distance curves corresponding to bead measurements were manually inspected, resulting in the identification of 100–130 indented curves per sample. After excluding outliers, around 1,400 peak force values were retained for analysis (**Table 9**). The median indentation force was 178 (IQR, 107–262) pN in the MFS group and 240 (IQR, 170–340) pN in controls ($P < 0.001$). The HI and DN subgroups exhibited median forces of 182 (IQR, 116–258) pN and 177 (IQR, 102–265) pN, respectively ($P = 0.322$), both significantly lower than the control group ($P < 0.001$) (**Figure 14**).

Table 9. Median indentation peak values with IQR per sample.

Sample ID	Number of peaks (n)	Peak force (pN)	Sample ID	Number of peaks (n)	Peak force (pN)
MFS1	28	223 (131–294)	**C1**	29	269 (201–359)
MFS2	37	155 (94–241)	**C2**	49	225 (170–392)
MFS3	86	169 (109–268)	**C3**	67	306 (219–366)
MFS4	64	160 (115–223)	**C4**	123	232 (166–317)
MFS5	69	194 (112–304)	**C5**	91	176 (122–315)
MFS6	86	185 (103–271)	**C6**	91	210 (163–317)
MFS7	74	172 (104–266)	**C7**	40	228 (146–354)
MFS8	100	136 (88–212)	**C8**	82	271 (214–360)
MFS9	27	208 (174–396)	**C9**	106	239 (150–322)
MFS10	80	193 (105–273)	**C10**	94	280 (182–371)

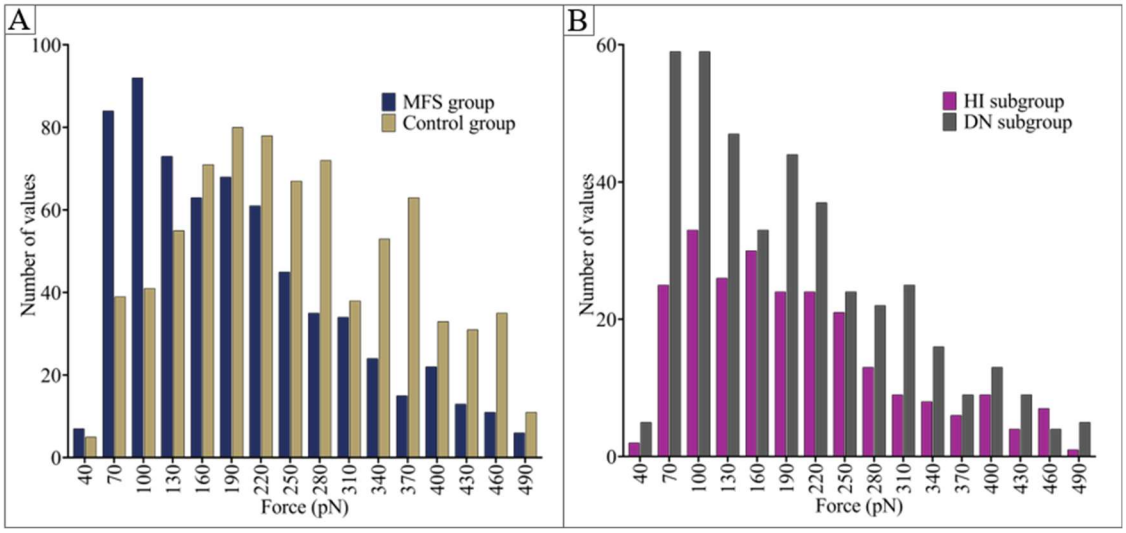

Figure 14. Indentation peak force analysis from AFM force-distance curves. **A.** Histogram comparing the distribution of force values between the MFS and control cohorts. **B.** Comparison between the HI and DN subgroups.

4.2. Titin study

4.2.1. Study population

The investigated cohort consisted of six females and six males with a mean age of 33.0 ± 10.9 years and a BMI of 21.6 ± 3.7 kg/m² at the time of surgery. Besides hypertension, which had been diagnosed in three patients (25%), no other atherosclerotic risk factors were present in the population. Coronary artery disease and symptomatic heart failure (New York Heart Association class II) were each present in two cases (16.7%). MFS-specific diagnostic criteria and the results of *FBN1* genetic testing are presented in **Table 10**. All included patients had genetically confirmed *FBN1* mutations: six DN missense variants and six HI mutations, namely two nonsense, two splice site, one copy number variation, and one frameshift mutation. Systemic involvement (score equal to or greater than 7 according to the revised Ghent criteria [14]) was established in ten patients (83.3%), with a median score of 8 (7–9). All patients had aortic involvement in the form of aortic root aneurysm, and one patient also had a previous history of chronic Stanford type B aortic dissection. Familial history of MFS was present in five patients (41.7%). *Ectopia lentis* occurred in 30% of cases, exclusively among individuals with cysteine-affecting missense variants.

Table 10. MFS-specific diagnostic criteria and results of *FBN1* genetic testing in the PAP cohort [160].

Patient ID	MFS-specific diagnostic criteria			*FBN1* mutation					
	Systemic score	Family history	*Ectopia lentis*	Nucleotide change	Exon	Amino acid change	Mutation effect	Mutation type	Variant classification
PAP33	9			c.6697C>T	55	p.Pro2233Ser	missense	DN	likely pathogenic
PAP37	8		present	c.3959G>C	32	p.Cys1320Ser	missense	DN	likely pathogenic
PAP39	8			c.6856G>T	56	p.Gly2286Ter	nonsense	HI	pathogenic
PAP46	7	present		c.4748-3T>G	intron 38		splice site	HI	pathogenic
PAP57	13	present		c.762delC	8	p.Leu256Serfs*74	frameshift	HI	pathogenic
PAP70	9		present	c.7168T>C	58	p.Cys23390Arg	missense	DN	pathogenic
PAP87	5			c.4337-2A>G	intron 35		splice site	HI	pathogenic
PAP90	9	present			2–4		copy number variation	HI	pathogenic
PAP93	7	present		c.1693C>T	14	p.Arg565Ter	nonsense	HI	pathogenic
PAP100	5			c.1282_1283delCCinsTG		p.Pro428Cys	missense	DN	likely pathogenic
PAP101	9	present	present	c.2287T>G	19	p.Cys763Gly	missense	DN	likely pathogenic
PAP104	7		present	c.2809T>C	24	p.Cys937Arg	missense	DN	likely pathogenic

Surgery was indicated by annuloaortic ectasia, often with associated ascending aortic aneurysm (n = 9), or aortic (n = 5) or mitral (n = 1) valve insufficiency. The aortic valve had a tricuspid conformation in all patients. The median grade of regurgitation for both the aortic and mitral valves was 1 (0–2). Mitral valve prolapse was present in seven cases. Preoperative echocardiographic assessment revealed no wall motion abnormalities. Detailed echocardiographic results are summarized in **Table 11**.

Table 11. Preoperative echocardiographic findings [160]. Reference values are stated according to the Recommendations of the European Society of Cardiology and the American Society of Echocardiography [174,175].

Investigated parameter	Measured values	Normal values
Ejection fraction (%)	60.83 ± 3.97	52–72
LV end-systolic diameter (mm)	35.60 ± 8.75	25.0–39.8
LV end-diastolic diameter (mm)	50.08 ± 7.75	42.0–58.4
Aortic annulus diameter (mm)	23.75 ± 1.91	26 ± 3
Diameter at the sinuses of Valsalva (mm)	50.42 ± 7.54	34 ± 3
Ascending aorta diameter (mm)	40.20 ± 9.85	30 ± 4
Aortic valve regurgitation > 1 (n)	4 (30%)	absent
Mitral valve regurgitation > 1 (n)	4 (30%)	absent
Mitral valve E/A ratio	1.32 ± 0.36	0.73–2.33
Deceleration time (msec)	205.11 ± 51.91	138–219

4.2.2. Proteomic analysis

The SDS-agarose gel electrophoresis revealed clearly distinguishable N2BA and N2B titin isoform bands in both PAP and DCM samples, while the rat control sample predominantly displayed the stiffer N2B band (**Figure 15A**). Diffuse T2 bands, indicative of titin degradation products, were also observed. Notably, several PAP samples (particularly PAP100 and PAP104) exhibited additional prominent bands above those corresponding to the MHC. Gel densitometry analysis was performed to quantify titin isoform expression and their relative proportions (**Figure 15B** and **C**). The mean N2BA:N2B ratio in PAP myocardial samples was 0.71 ± 0.19 (**Table 12**), markedly higher than in the control rat heart (0.28), but lower (P = 0.045) than in previously investigated *TTN*tv- DCM specimens (0.84 ± 0.19) [161]. Overall, the N2BA:N2B ratios in PAP samples exceeded values typically reported for healthy human myocardium (around 0.5) [137,138] (**Figure 15D**). The expression profile in PAP specimens resembled

that of DCM samples, with a marked predominance of the more compliant N2BA isoform, in contrast to the control rat heart, where the stiffer N2B isoform dominated (**Figure 15C**).

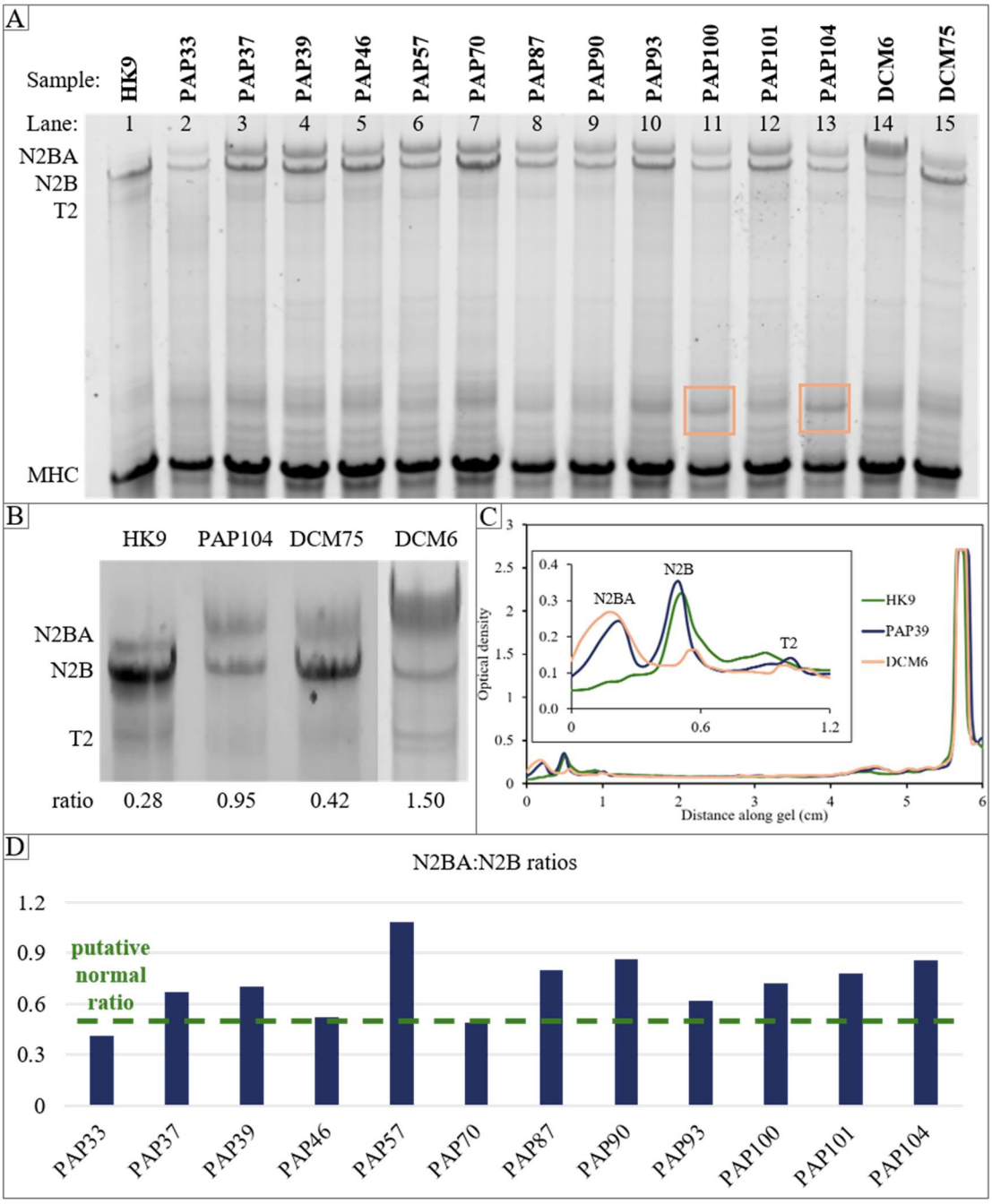

Figure 15. Proteomic analysis of titin [160]. **A.** 1% SDS-agarose gel analysis of included samples from MFS patients (labeled PAP), including samples used as control (HK9, rat; DCM6 and DCM75, human). The beige squares highlight the additional bands observed more prominently in samples PAP100 and PAP104. **B.** Magnified gel regions showing the titin isoforms N2BA and N2B, and titin's proteolytic cleavage product T2, in the three types of samples, as well as the respective calculated N2BA:N2B ratios. **C.** A typical optical density plot profile used to calculate the titin isoform ratios from the areas under the curves. **D.** N2BA:N2B titin isoform ratios calculated across the PAP patient cohort. The green segmented line indicates the mean conceived normal ratio (approximately 0.5).

Table 12. Proteomic analysis of titin isoforms in PAP samples [160].

Sample ID	N2BA:N2B	N2BA:MHC	N2B:MHC	T1:MHC	T2:MHC	TT:MHC
PAP33	0.41	0.02	0.06	0.08	0.05	0.13
PAP37	0.67	0.07	0.11	0.18	0.05	0.23
PAP39	0.70	0.07	0.10	0.17	0.05	0.22
PAP46	0.53	0.06	0.11	0.16	0.05	0.21
PAP57	1.08	0.08	0.07	0.15	0.04	0.19
PAP70	0.49	0.06	0.13	0.19	0.04	0.24
PAP87	0.80	0.07	0.08	0.15	0.04	0.19
PAP90	0.87	0.06	0.07	0.12	0.03	0.16
PAP93	0.62	0.06	0.09	0.15	0.05	0.20
PAP100	0.72	0.05	0.07	0.11	0.04	0.15
PAP101	0.78	0.07	0.09	0.16	0.05	0.21
PAP104	0.86	0.07	0.08	0.14	0.06	0.20
Mean	0.71	0.06	0.09	0.15	0.05	0.19
SD	0.19	0.01	0.02	0.03	0.01	0.03

TT level normalized to MHC was 0.19 ± 0.03, lower (P = 0.004) than values observed in earlier analyzed *TTN*tv- DCM samples (0.27 ± 0.09) [161]. T1 expression relative to MHC was also significantly lower in PAP than in *TTN*tv- DCM samples (0.15 ± 0.03 vs. 0.22 ± 0.08, $P < 0.001$), while titin degradation (T2:MHC) showed no significant difference between groups (0.05 ± 0.01 vs. 0.04 ± 0.02, $P = 0.117$) (**Table 12**).

Western blotting using titin-specific antibodies T12 and M8M10 (**Figure 16**) showed weak labeling of the additional bands by the T12 antibody, while M8M10 produced no detectable signal. These findings indicate that the prominent bands, particularly in PAP100 and PAP104, likely correspond to N-terminal titin fragments associated with T2.

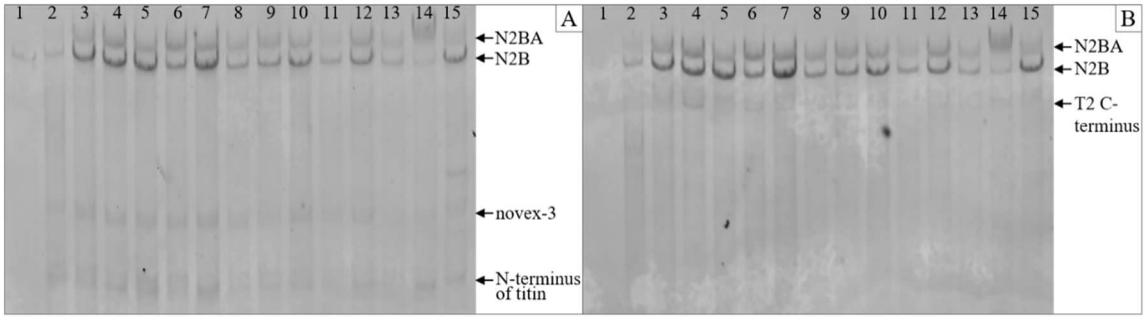

Figure 16. Western blot analysis of additional bands [160]. **A.** T12 antibody labeling, which binds the N-terminus of titin. **B.** M8M10 anti-titin antibody labeling, which binds titin near its C-terminus. The smaller or partial titin forms are also indicated.

4.2.3. Clinical correlations

To assess whether the titin isoform expression ratio in MFS LV myocardium is linked to cardiac performance, potential correlations between the N2BA:N2B ratio and a range of clinical and echocardiographic parameters (**Figure 17**). Three patients (PAP33, PAP90, and PAP100) exhibited LV enlargement based on end-systolic and end-diastolic diameter measurements. However, due to the small cohort size and the generally preserved cardiac function across most cases, no clear associations between the N2BA:N2B ratio and any of the assessed parameters could be established.

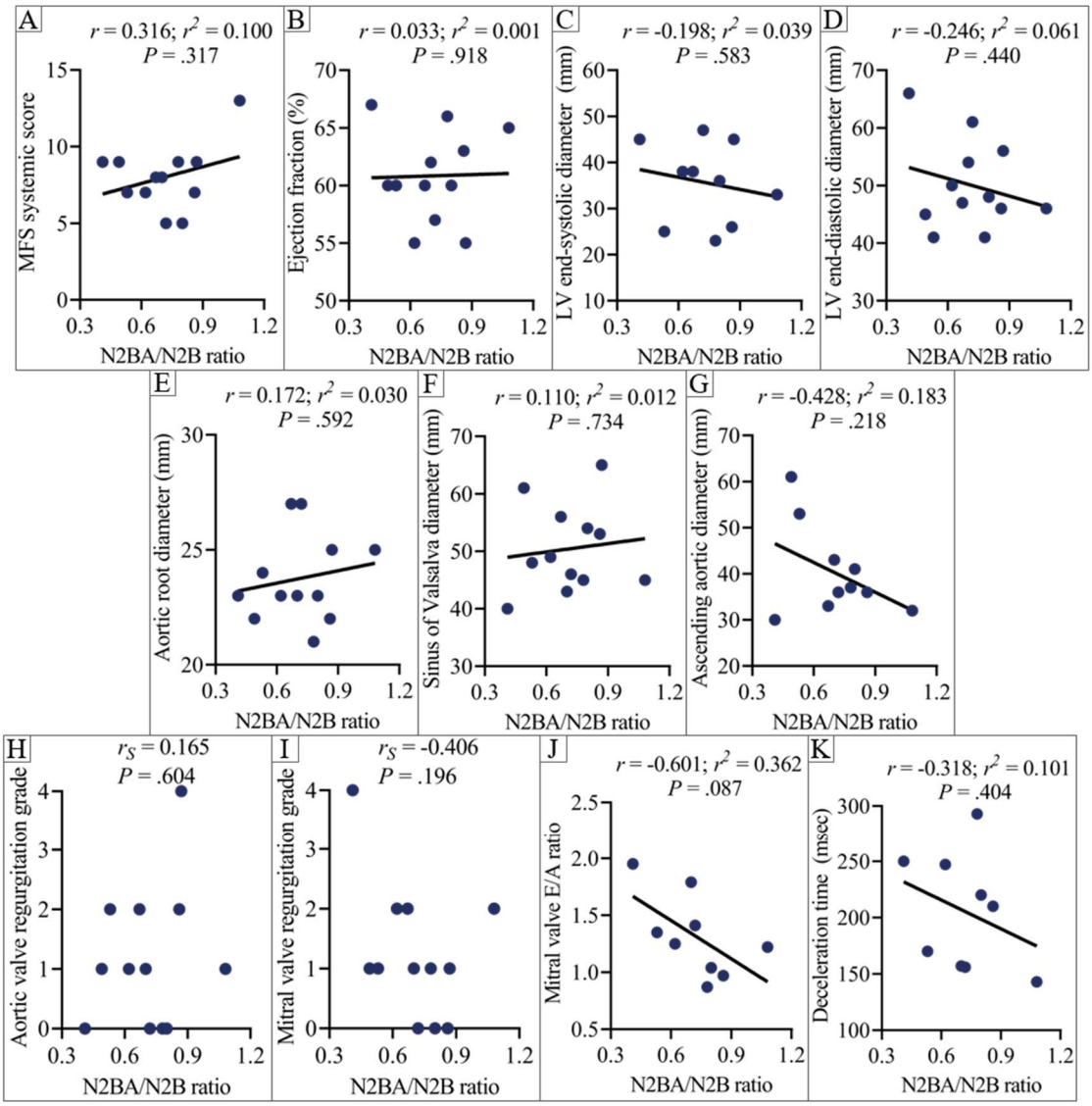

Figure 17. Correlation analyses between the N2BA:N2B titin isoform expression ratio and selected clinical and echocardiographic parameters in the PAP cohort [160]. Each panel (**A**–**K**) displays a scatter plot; linear regression lines are shown for datasets analyzed with Pearson's correlation. Spearman's correlation (r_S) was used for non-normally distributed datasets (**H** and **I**), for which no r^2 values or regression lines are shown.

5. Discussion

The present study explored two aspects of cardiovascular involvement in MFS: the structural and nanomechanical properties of aortic fibrillin-1 microfibrils, and the expression of myocardial titin isoforms. Our findings provide insight into how defects in extracellular and sarcomeric structural components may shape aortic pathology and myocardial dysfunction, thus contributing to the complex MFS cardiovascular phenotype.

5.1. Fibrillin-1 study

We hypothesized that ultrastructural and mechanical alterations in fibrillin-1 microfibrils contribute to aortic root pathology in MFS. To investigate this, we first performed a detailed AFM-based analysis focusing on quantitative parameters that describe bead and interbead morphology. These metrics reflect the molecular organization, packing, and surface topography of the microfibrils, which are dependent on biochemical composition. To evaluate the mechanical properties of human aortic fibrillin-1 microfibrils and the impact of *FBN1* mutations on their elastic behavior, transverse stiffness was measured using AFM-based force spectroscopy. To our knowledge, this study represents the first characterization of fibrillin-1 microfibrils in human aortic tissue, specifically comparing MFS and non-MFS samples.

5.1.1. MFS cohort genetic profile

Seven of the identified variants affected cysteine residues within fibrillin-1 (**Figure 18**). Cysteine is the most abundant amino acid in fibrillin-1, accounting for 12.6% of its sequence, as reported in the National Center for Biotechnology Information RefSeq database (accession NM_000138.4) [176]. This high cysteine content reflects the prevalence of (cb)EGF and TB domains within fibrillin-1, which relies on disulfide bonding for proper folding and structural integrity. These domains contain six and eight conserved cysteines, respectively, that form disulfide bonds in characteristic pairings: 1–3, 2–4, and 5–6 in (cb)EGF modules, and 1–3, 2–6, 4–7, and 5–8 in TB domains [177,178]. Missense mutations substituting or generating cysteine residues are the most frequent MFS-causing variants identified in *FBN1* [162]. In this cohort, five of the seven cysteine-altering variants were missense changes predicted to disrupt disulfide bonding within cbEGF or EGF domains, thereby destabilizing domain structure and overall protein conformation.

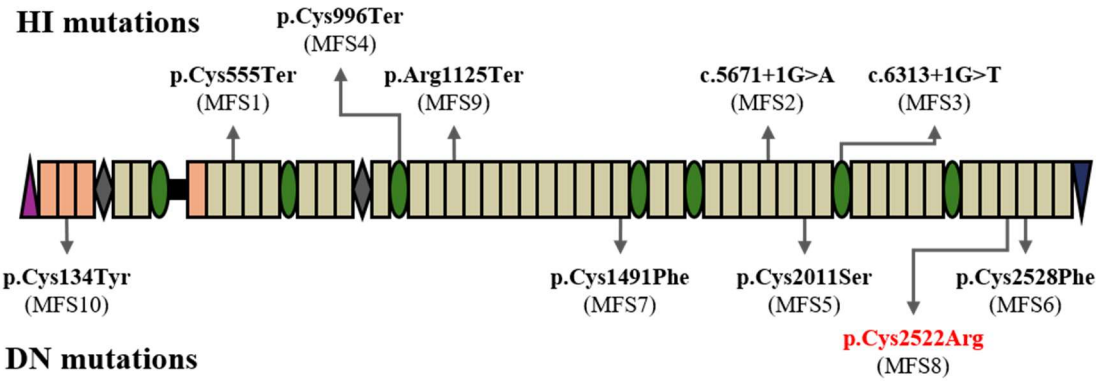

Figure 18. The spectrum of *FBN1* variants identified in the MFS cohort, listed according to their location within the fibrillin-1 molecule and the predicted pathogenic mechanism. The novel variant is highlighted in red.

In cases with nonsense variants, the mutant fibrillin-1 is predicted to undergo NMD, as the PTCs occur well upstream of the final exon-exon junction or the last 50 base pairs of the penultimate exon [179]. This mechanism would result in functional HI, with degradation of truncated fibrillin-1 before it can be incorporated into microfibrils, ultimately reducing total protein levels [180]. While not directly introducing a PTC, the two splice site mutations are anticipated to result in protein truncation, although they may also cause exon skipping or other splicing abnormalities [181].

Overall, the genetic spectrum identified in this cohort reflects the well-established allelic heterogeneity of MFS. The predicted molecular consequences of the identified *FBN1* mutations range from localized structural disruption at critical residues within fibrillin-1 to complete transcript degradation due to NMD. These molecular effects are important to consider in interpreting microfibril morphology and mechanics.

5.1.2. Structural measurements

Fibrillin-1 microfibrils were easily identifiable on AFM images based on their typical “beads-on-a-string” appearance. While their overall aspect was preserved across all samples regardless of disease status, subtle size differences were apparent. The interbead regions typically appeared as two or, occasionally, three thin arms linking adjacent beads, though they often formed a thicker connecting band. In some cases, these regions were extremely thin and barely discernible. The purified microfibrils displayed considerable variability in length in both MFS and control specimens.

In many cases, fine filamentous projections extended laterally from the beads. Previous experiments demonstrated that C-terminal fibrillin-1 fragment multimerization

produces assemblies that closely mimic native microfibrillar beads, often displaying lateral projections terminating in globular domains, resembling monomeric fibrillin-1 particles [182]. Therefore, these structures may contribute to the lateral association and spatial organization of microfibrils within the ECM.

MFS microfibrils displayed significant morphological alterations compared with controls across multiple parameters. Maximum and average bead heights were slightly increased in the MFS group, whereas bead length and width were significantly reduced compared to controls. Consequently, the projected area of the control beads greatly exceeded that of MFS beads. To better capture the three-dimensional complexion of the beads, we also assessed their volume, which was significantly lower in MFS microfibrils, potentially indicating reduced protein density or impaired bead assembly.

The maximum bead height values measured in both groups aligned with previous AFM reports [75,183]. However, the lateral dimensions (19–25 nm) appeared somewhat smaller than earlier AFM measurements (30–40 nm) [75]. This discrepancy can likely be attributed to the known fact that horizontal AFM measurements are strongly affected by cantilever tip geometry. As a result, AFM has historically yielded larger bead widths than other imaging modalities, such as rotary shadowing electron microscopy, which typically reported bead diameters in the range of 22–29 nm [182]. Nevertheless, the consistency of our measurements supports the reliability of the observed differences between samples and groups.

Bead roundness and aspect ratio were evaluated to further explore morphological differences. Although statistically significant, the absolute values were similar, suggesting minimal practical variation between individual specimens. Roundness indicated a slightly elongated bead shape, consistent with AFM observations. The aspect ratio reinforced this finding, with most beads appearing laterally elongated. Thus, based on our analysis, fibrillin-1 microfibril beads appear as ellipsoid structures with dimensions of 8.2 x 18.8 x 19.7 nm and 7.0 x 23.7 x 24.4 nm in MFS and control aortic tissue, respectively.

Interbead region height showed considerable variability among individual MFS samples but remained relatively uniform in the control group. This variability may reflect structural disruptions caused by *FBN1* mutations affecting regions of the fibrillin-1

molecule that are localized in the interbead segments. On average, interbead height was significantly reduced in the MFS group. In contrast, periodicity ranged narrowly from approximately 50 to 56 nm across individual samples, independent of clinical diagnosis. Despite reaching statistical significance, the difference in periodicity between groups seems to have limited biological relevance, as this interval for periodicity is within the expected physiological range for relaxed microfibrils [73,75,76,85].

A significant negative correlation was consistently observed between interbead region height and periodicity across all samples, suggesting that microfibril elongation is accompanied by an increase in bead-to-bead distance and thinning of the interbead region. This aligns with previous findings by Baldock *et al*., who proposed that elongation up to approximately 100 nm results from reversible interbead unfolding involving TB-EGF domain flexibility, whereas elongations beyond 100 nm involve irreversible bead unraveling and loss of elasticity [73,184]. Similarly, Wang *et al*. demonstrated that periodicity changes up to 85 nm arise from reversible salt bridge dynamics, and that elongation beyond this threshold leads to bead mass reduction [185].

When stratifying MFS patients based on the predicted molecular mechanism of the respective *FBN1* mutation, different morphological patterns became apparent. Across most parameters, DN microfibrils occupied an intermediate position between the HI and control groups regarding size. Compared to HI samples, DN beads exhibited slightly lower heights but larger horizontal dimensions, resulting in greater projected areas and increased volume. Bead roundness and aspect ratio did not differ significantly between subgroups. However, intriguing differences were observed regarding the interbeads, as the interbead region height in DN samples closely resembled that of controls. In contrast, HI samples showed a marked reduction in this parameter despite having a comparable median periodicity.

To interpret these results, it is important to consider the distinct molecular mechanisms underlying each MFS case. However, the precise arrangement of fibrillin-1 molecules within microfibrils remains incompletely resolved, limiting our ability to interpret variant-specific effects. Previous antibody mapping studies supported by recent mass spectrometry data suggest that the EGF4–TB2 regions of the eight fibrillin-1 molecules forming a repeat are localized deep within the bead core [20,72,73,77].

Domains upstream of this segment, extending to the first hybrid domain, are likely positioned near the bead periphery. Given that fibrillin-1 molecules align head-to-tail, with N- and C-terminal regions connecting within the beads, and considering the substantial bead mass, it is plausible that terminal regions overlap considerably within the bead, while the remaining portions extend outward to form the interbead regions [72].

In the studied MFS cohort, all DN mutations were missense variants causing single amino acid substitutions, particularly cysteine, within fibrillin-1. These mutant transcripts remain bioavailable and can incorporate into microfibrillar assemblies [186]. Therefore, they are implicated in MFS pathogenesis by impacting local folding and/or molecular interactions. According to UMD predictions, samples MFS6 and MFS7 involve the loss of cysteine residue 1 in cbEGF domains 40 and 22, respectively; in MFS5 and MFS8, cysteine residue 6 is compromised in modules cbEGF30 and cbEGF39, respectively; in sample MFS10, cysteine residue 4 in EGF2 is affected [162]. These variants are expected to disrupt disulfide bonds essential for proper domain folding, potentially destabilizing fibrillin-1 and impairing interactions with associated molecules that normally add to repeat mass, thus resulting in altered structural parameters in DN microfibrils [72]. Furthermore, mutations disrupting calcium-binding sequences likely increase proteolytic susceptibility, as calcium protects fibrillin-1 from degradation [32,187]. *FBN1* variants affecting disulfide bonds in (cb)EGF domains have been shown to compromise thermostability and heighten fibrillin-1 susceptibility to proteases [188]. Nevertheless, point mutations in critical domains of fibrillin-1 appear to lead to the formation of structurally abnormal microfibrillar assemblies [18]. The classification of cysteine-altering DN mutations as a distinct severity subgroup is gaining recognition, as emerging evidence suggests they are associated with a more severe aortic phenotype compared to non-cysteine DN variants [189].

The pronounced morphological alterations seen in the HI subgroup were remarkable. Since the truncated transcripts are predicted to undergo NMD, HI microfibrils, containing predominantly wild-type fibrillin-1, would be expected to be more similar to controls. Instead, they differed significantly, indicating that HI leads not only to reduced overall fibrillin-1 abundance in tissues but also impairs microfibril assembly [190]. This could be the consequence of the resulting quantitative fibrillin-1 monomer deficiency interfering with microfibril synthesis and aggregation into the ECM.

Microfibril formation is a concentration-dependent process: insufficient levels of normal fibrillin-1 are primarily responsible for the defective matrix deposition and impaired microfibrillar assembly observed in mouse models and pulse-chase studies involving human fibroblasts [186,191]. An alternative hypothesis is that small amounts of structurally abnormal mutant transcripts become incorporated into microfibrils. For *FBN1* variants introducing PTCs, mutant transcripts have been detected at levels ranging from 2% to 28% relative to the wild-type protein [191-194]. Although direct evidence of truncated fibrillin-1 protein incorporation into microfibrils remains limited due to their low expression and detection challenges [195], a contribution to defective microfibril architecture cannot be excluded. Finally, similarly to DN cases, these thinner microfibrils may exhibit increased susceptibility to mechanical stress or proteolytic degradation, further exacerbating their aberrant morphology.

All in all, multiple mechanisms offer plausible explanations for the alterations seen in MFS fibrillin-1 microfibrils. The morphological similarities between HI and cysteine-affecting DN microfibrils may explain the comparable severity of aortic manifestations reported for both mutation types [196]. Our results enrich previous findings suggesting that mutant *FBN1* alleles structurally disrupt the normal fibrillin-1 microfibrillar network regardless of the predicted molecular effect.

It is important to note that various disease states, such as diabetes mellitus, have been linked to morphological alterations of microfibrils, including changes in periodicity [197]. This consideration is particularly relevant to our control cohort, which consisted of older individuals with a higher prevalence of atherosclerotic risk factors. It could be argued that some of the microfibrillar features observed in this group may reflect pathological remodeling rather than physiological baseline structure. However, access to truly healthy aortic tissue, especially from age-matched individuals without cardiovascular pathology, is extremely limited. As the bead dimensions measured in control samples closely matched those previously reported from different imaging studies, and the microfibrillar parameters showed minimal inter-sample variability, we argue that these points support the suitability of this control group as a structural reference and further strengthen the conclusion that the morphological abnormalities observed in the MFS cohort are not attributable to technical artifacts, aging, or underlying

comorbidities, but are instead consistent with *FBN1* mutation-associated microfibrillar disruption.

5.1.3. Mechanical assessment

Median Young's modulus values for human aortic fibrillin-1 microfibrils ranged from 1.96 to 3.40 MPa. In MFS samples, medians varied between 1.96 and 3.21 MPa, whereas those from controls ranged from 2.53 to 3.40 MPa. These approximate previously reported stiffness values for fibrillin-1-rich structures across invertebrate and vertebrate species. For instance, the fibrillin-1 microfibrillar network in the sea cucumber dermis exhibited a Young's modulus of approximately 0.2 MPa [87], while jellyfish mesogleal fibers demonstrated values around 0.9 MPa [91]. Stiffness measurements in aortic tissue revealed values of approximately 0.4 MPa in both porcine and octopus samples [88,89], whereas a higher value of 1.06 MPa was recorded in lobster aorta [92]. Fibrillin-1-rich fibers derived from equine nuchal ligament and bovine zonular filaments have shown moduli between 0.56–0.74 MPa and 0.19–1.88 MPa, respectively [90,93]. An alternative measurement approach applied to fibrillin-1 microfibrils isolated from bovine zonular filaments yielded substantially higher Young's modulus values, ranging from 78 to 96 MPa [85]. The data reflect differences based on species, tissue type, and experimental setup. As a result, cross-comparisons remain limited.

The MFS group showed a broader distribution of median Young's moduli, likely reflecting inter-individual heterogeneity caused by the distinct pathogenic variants, each exerting unique effects on fibrillin-1 folding, assembly, and network organization. Still, MFS microfibrils exhibited an overall reduction in microfibrillar stiffness compared to controls. Notably, HI microfibrils had significantly lower stiffness than both their DN counterparts and controls, whereas DN and control values did not differ significantly. The HI subgroup shifted toward lower stiffness values, indicating reduced bead rigidity, while DN values largely overlapped with the higher control range. The narrower distribution in control samples suggests a stable mechanical profile characteristic of normal aortic fibrillin-1 microfibrils.

When considered alongside our structural findings, the decreased Young's modulus observed in the HI subgroup supports a model of diminished protein content within the beads, resulting in increased compliance. This hypothesis supports the notion

that HI may lead to reduced incorporation of fibrillin-1 monomers into the microfibrils due to a quantitative deficit in available wild-type fibrillin-1 molecules during early assembly stages [186,191]. Alternatively, HI microfibrils may incorporate both wild-type and truncated mutant monomers, with the latter lacking essential domains, thereby contributing less mass and structural rigidity to the beads. In contrast, the comparable stiffness observed in DN and control microfibrils suggests that microfibrils contain a similar amount of fibrillin-1, but the presence of structurally aberrant monomers likely alters bead organization and internal packing. This interpretation is consistent with evidence that point mutations disrupting disulfide bonds or calcium-binding motifs in cbEGF domains impair folding and molecular packing without necessarily reducing microfibrillar incorporation [198]. Moreover, DN-associated misfolding may interfere with the binding of fibrillin-associated proteins essential for bead growth and maturation, leading to smaller bead dimensions as observed, without substantially compromising the nanomechanical integrity of the microfibril core itself [72].

The indentation-like features observed on the force-distance curves, considered to reflect conformational changes or mechanical failure at the bead level, appeared at significantly lower forces in MFS microfibrils. Median forces were similar between the HI and DN subgroups but markedly reduced relative to controls, indicating a decreased resistance to mechanical deformation in MFS microfibrils. These results seem to contrast those of the nanomechanical calculations, where DN microfibrils demonstrated stiffness values comparable to controls and substantially higher than HI microfibrils. This apparent discrepancy may reflect underlying differences in microfibril organization that are not fully captured by stiffness measurements alone. One possible interpretation is that, although DN microfibrils maintain normal fibrillin-1 protein content similar to controls, resulting in preserved stiffness, their internal structural integrity is compromised due to aberrant domain folding or disrupted molecular packing caused by missense mutations in key domains. As a result, these microfibrils may fail locally under similar forces as HI microfibrils, which conceivably contain less fibrillin-1. Thus, despite differing stiffness profiles, both mutation types share a reduced threshold for structural disruption when subjected to mechanical stress, pointing to a common architectural vulnerability associated with *FBN1* mutations.

5.1.4. Practical interpretation of AFM findings

In the aortic wall, fibrillin-1 microfibrils surround elastin cores in the *media*, thus enforcing the resulting elastic fibers and possibly mediating force transmission across these units [88]. Elastin fibers form thick, concentric *lamellae* alongside circumferentially arranged smooth muscle cells and collagen [199], creating a configuration that enables the arterial wall to dynamically accommodate blood pressure fluctuations throughout the cardiac cycle. In this architectural context, fibrillin-1 microfibrils have been proposed to act as load-bearing elements involved in elastic recoil [28].

The extent to which fibrillin-1 microfibrils contribute to overall tissue elasticity remains uncertain. Some studies suggest a limited role; for example, experiments on elastic fibers from equine nuchal ligament showed no significant change in elastic properties after the removal of fibrillin-1 microfibrils, with Young's modulus values remaining comparable to those of elastin (0.56–0.74 MPa) [90]. In contrast, Sherratt *et al*. reported exceptionally high stiffness values for isolated fibrillin-1 microfibrils, indicating a potential reinforcing function within elastic fibers [85]. Supporting this view, studies on pig aorta elastic fibers demonstrated that microfibril removal altered fiber compliance under mechanical strain, implying that these microfibrils may participate in modulating load distribution across the elastic fiber network [88].

Our analysis indicated that MFS fibrillin-1 microfibrils exhibit architectural defects that lead to compromised nanomechanical performance. Microfibrils isolated from MFS aortic tissue showed altered structural integrity, evidenced by reduced bead and interbead dimensions, lower stiffness, and decreased resistance to mechanical failure, which may limit their capacity to reinforce and stabilize elastic fibers under normal physiological strain. This impaired resilience likely limits their ability to withstand repetitive mechanical loading, contributing to the disarray and fragmentation of elastic fibers, which is a defining feature of medial degeneration in the MFS aorta [9]. Furthermore, defective microfibrils may impair the mechanical integration and anchorage of elastic *lamellae*, thereby increasing local wall stress and promoting aneurysm formation. Over time, these molecular abnormalities likely exacerbate extracellular matrix degradation and smooth muscle cell loss, ultimately culminating in aortic dissection [200].

5.2. Titin study

MFS is characterized by significant cardiac involvement, most commonly valvular abnormalities. Mitral valve prolapse, affecting up to 40% of patients, is the most frequent, while tricuspid valve degeneration has been reported in 12% of MFS patients undergoing cardiac surgery [123,201]. Multivalvular dysfunction can result in chronic volume overload, potentially leading to LV dilation and dysfunction. Approximately 5% of MFS patients with mitral regurgitation develop cardiac failure [202]. Notably, in MFS, myocardial dysfunction has been observed independently of significant valvular disease, including in pediatric cases, contributing to the recognition of Marfan cardiomyopathy as a distinct clinical entity [125,203,204].

In specific cardiomyopathies, especially DCM, the link between cardiac muscle impairment and titin is well-established. *TTN*tvs are the most frequent known cause of DCM, being responsible for approximately a quarter of the cases [205]. The giant elastic sarcomeric protein titin governs passive myocardial stiffness by acting as a molecular spring between the Z-disk and M-band [133]. Regulatory alternative splicing in the *TTN* gene generates two main myocardium-specific isoforms (N2B and N2BA) with different structures and mechanical properties. Their relative expression modulates titin-based passive tension in the cardiac sarcomere, but also varies with developmental stage, species, and pathological states [136,206,207]. In disease models such as tachycardia-induced DCM in dogs or hypertensive rats, an isoform shift toward the N2B isoform was described, associated with increased myocardial passive stiffness and increased LV afterload, respectively [208,209]. Conversely, human DCM hearts typically exhibit an elevated N2BA:N2B ratio, reflecting a reduction in passive stiffness and compensatory remodeling [137,138,210]. With increasing evidence pointing to intrinsic myocardial dysfunction in MFS, we sought to explore the role of titin isoform expression in the mechanisms underlying Marfan cardiomyopathy.

Our findings constitute the first report of titin isoform composition in the myocardium of MFS patients. We quantified the total titin content in MFS myocardium by normalizing the sum of the N2BA, N2A, and T2 bands to MHC, yielding a mean value of 0.19 ± 0.03. This is comparable to previously reported levels in normal human myocardium (0.20 ± 0.02 and 0.23 ± 0.03) [137,211] and to that measured in the included

*TTN*tv- DCM samples (0.19 ± 0.05), although lower than values observed in DCM in our earlier work [161]. Notably, the amount of full-length titin (T1/MHC) was reduced in PAP samples compared to DCM samples, possibly suggesting proteolytic degradation, an idea supported by the presence of additional protein bands in electrophoretic analyses, though further investigations are required.

We identified a shift in isoform expression toward the more compliant N2BA titin in the MFS myocardium, with a mean N2BA:N2B ratio of 0.71 ± 0.19. This markedly exceeds values reported in healthy donor hearts (approximately 0.4–0.56) [137,138] while nearing levels measured in *TTN*tv- DCM myocardial tissue [161]. Although no significant correlations were observed between the N2BA:N2B ratio and the investigated clinical and echocardiographic variables, this may reflect the limited cohort size rather than a true absence of correlation. Nevertheless, the observed isoform shift likely indicates a compensatory molecular remodeling response to altered myocardial mechanics in MFS. This hypothesis is consistent with recent cardiac magnetic resonance imaging findings showing diffuse myocardial fibrosis in MFS tissue, suggesting that ECM abnormalities contribute to altered sarcomeric mechanics [212]. In particular, increased ECM stiffness, driven by defective fibrillin-1/elastin networks and enhanced TGF-β signaling, may increase mechanical load on titin, thus promoting the isoform switching. Additionally, insufficient TGF-β sequestration by fibrillin-1 microfibrils can result in pathway overactivation, potentially altering titin phosphorylation and elasticity [53].

All in all, the results indicate a preserved total amount of titin but reduced full-length titin content and marked N2BA isoform expression in MFS myocardium, paralleling patterns observed in DCM and hinting at potential molecular mechanisms involved in the development of Marfan cardiomyopathy.

5.3. Limitations

An important limitation across both projects (fibrillin-1 and titin) is the relatively small sample size, inherent to research on rare genetic disorders such as MFS. Nevertheless, the cohort size exceeded that of many comparable studies employing AFM-based approaches [156,197]. Obtaining patient material, especially fresh surgical aortic

and myocardial samples, is particularly challenging, further limiting large-scale recruitment.

Another significant barrier in this type of investigation is the inability to include truly healthy individuals as controls. The use of cadaveric samples was excluded to preserve tissue quality and maintain a uniform harvesting process. Thus, controls were derived from patients undergoing surgery for other cardiovascular conditions but without evidence of connective tissue or aortic diseases. Despite efforts to match cohorts, age and tissue quality differences may have introduced subtle, disease-related variations in microfibril properties.

In the case of the fibrillin-1 microfibril analysis, methodological constraints also apply. AFM relies on examining microfibrils outside their native ECM environment, where biological dynamics are absent. While this allows for high-resolution structural and mechanical investigations, it reduces the biological context. Furthermore, the technique is sensitive to experimental variables; however, under standardized preparation and measurement protocols, the measurements and comparisons remain valid and robust.

In the titin analysis, although we identified an adaptive sarcomeric response in the MFS myocardium, functional measurements at the cardiomyocyte level were not performed, limiting the ability to directly correlate molecular changes to biomechanical performance. Age-related or disease-independent factors may also influence titin isoform expression. However, the identification of a titin isoform shift, even in a small cohort, offers valuable evidence of intrinsic sarcomeric adaptation to extracellular matrix dysfunction, supporting the concept of an early, disease-specific myocardial phenotype. This novel finding lays important groundwork for future studies to better understand and target cardiac involvement in MFS.

Despite these constraints, the study provides novel molecular-level insights into how *FBN1* variants disrupt the structure and mechanical integrity of fibrillin-1 microfibrils and alter myocardial titin composition. These findings highlight potential mechanisms by which ECM dysregulation contributes to both aortic and myocardial pathology in MFS. Future studies should explore links with TGF-β signaling activity and integrate functional data from vascular and myocardial tissues, in order to develop a more complete model of MFS pathogenesis.

6. Conclusions

In this study, we explored the morphological and nanomechanical characteristics of individual fibrillin-1 microfibrils isolated from human aortic tissue in MFS and non-MFS individuals. In parallel, we examined the potential involvement of sarcomeric titin in the myocardial changes associated with Marfan cardiomyopathy.

1. Our analysis provided a detailed characterization of human aortic fibrillin-1 microfibrils.
2. AFM imaging showed that, although the typical beaded aspect of fibrillin-1 microfibrils was preserved across all samples, MFS microfibrils, regardless of the underlying *FBN1* mutation type, exhibited pronounced morphological alterations, notably reduced bead and interbead dimensions, suggestive of disrupted molecular organization.
3. Force spectroscopy measurements demonstrated a notable reduction in transverse stiffness (Young's modulus) in MFS microfibrils, particularly in those from patients with HI *FBN1* mutations. Additionally, AFM-based nanomanipulation revealed failure-like events at the level of the beads, indicating a compromised ability of MFS microfibrils to withstand mechanical stress.
4. Proteomic analysis of LV myocardium revealed a shift in titin isoform expression in MFS hearts, characterized by an increased N2BA:N2B ratio, while total titin content remained unchanged. We propose that this shift toward the more compliant N2BA isoform represents a compensatory mechanism aimed at reducing passive myocardial stiffness in response to ECM abnormalities associated with MFS.

Collectively, these findings reveal that *FBN1* mutations lead to structural and mechanical impairment of fibrillin-1 microfibrils within the aortic wall and are associated with molecular remodeling of titin in the myocardium. Both mechanisms may contribute to the vascular fragility and intrinsic myocardial dysfunction characteristic of MFS.

7. Summary

Marfan syndrome (MFS) is an autosomal dominant connective tissue disorder caused by pathogenic variants in *FBN1*, which encodes fibrillin-1, the core component of extracellular microfibrils. In the aortic wall, these structures are critical for maintaining structural integrity and bearing mechanical loads. *FBN1* mutations are expected to impact the function of fibrillin-1 microfibrils, thereby contributing to the main manifestations of MFS, namely progressive aortic aneurysm and dissection, which remain the leading causes of morbidity and mortality in affected individuals. In addition to aortic involvement, growing evidence suggests that MFS may also involve an intrinsic form of cardiomyopathy, a condition typically linked to the sarcomeric protein titin. These observations highlight the need for a deeper molecular understanding of how *FBN1* variants translate into structural and functional alterations within cardiovascular tissues.

We examined the morphology and nanomechanical properties of individual fibrillin-1 microfibrils isolated from the aortic tissue of MFS patients and non-MFS controls. Atomic force microscopy revealed a preserved microfibrillar appearance but significant morphological changes in MFS samples, where microfibrils exhibited a more fragile structure. Force spectroscopy showed a reduction in microfibrillar stiffness in MFS patients carrying haploinsufficient *FBN1* variants. Indentation-like features in the force-distance curves, interpreted as localized mechanical failure, appeared at significantly lower forces in MFS microfibrils, emphasizing their mechanical fragility.

In parallel, we assessed titin expression within the left ventricular myocardium of MFS patients. Proteomic profiling revealed a shift toward the more compliant N2BA isoform in MFS patients, without a change in total titin content. This change may represent an adaptive response to the extracellular matrix alterations characteristic of MFS, aimed at preserving diastolic function through reduced myocardial stiffness.

In summary, our findings provide a detailed characterization of the molecular and mechanical consequences of *FBN1* mutations in the human aorta and myocardium. The results indicate that aortic fibrillin-1 microfibrils are morphologically and mechanically compromised in MFS, while sarcomeric remodeling in the left ventricular myocardium occurs even in the absence of overt valvular disease, suggesting a broader compensatory response to altered mechanical homeostasis in this condition.

8. References

1. Marfan A. Un cas de déformation congénitale des quartre membres, plus prononcée aux extrémitiés, caractérisée par l'allongement des os avec un certain degré d'amincissement [A case of congenital deformation of the four limbs, more pronounced at the extremities, characterized by elongation of the bones with some degree of thinning]. Bull Mem de la Société Médicale des Hôpitaux de Paris. 1896;13:220–228.
2. Baumgartner WA, Cameron DE, Redmond JM, Greene PS, Gott VL. Operative management of Marfan syndrome: The Johns Hopkins experience. Ann Thorac Surg. 1999;67(6):1859–1860; discussion 1868–1870.
3. MedlinePlus. Bethesda (MD): National Library of Medicine (US). Marfan syndrome [Internet]. 2018 [updated 2018 May 01; cited 2025 Apr 22]. Available from: https://medlineplus.gov/genetics/condition/marfan-syndrome/.
4. Judge DP, Dietz HC. Marfan's syndrome. Lancet. 2005;366(9501):1965–1976.
5. Hilhorst-Hofstee Y, Rijlaarsdam ME, Scholte AJ, Swart-van den Berg M, Versteegh MI, van der Schoot-van Velzen I, Schabitz HJ, Bijlsma EK, Baars MJ, Kerstjens-Frederikse WS, Giltay JC, Hamel BC, Breuning MH, Pals G. The clinical spectrum of missense mutations of the first aspartic acid of cbEGF-like domains in fibrillin-1 including a recessive family. Hum Mutat. 2010;31(12):E1915–1927.
6. Charbonneau NL, Dzamba BJ, Ono RN, Keene DR, Corson GM, Reinhardt DP, Sakai LY. Fibrillins can co-assemble in fibrils, but fibrillin fibril composition displays cell-specific differences. J Biol Chem. 2003;278(4):2740–2749.
7. Sakai LY, Keene DR, Engvall E. Fibrillin, a new 350-kD glycoprotein, is a component of extracellular microfibrils. J Cell Biol. 1986;103(6 Pt 1):2499–2509.
8. Lazea C, Bucerzan S, Crisan M, Al-Khzouz C, Miclea D, Sufana C, Cismaru G, Grigorescu-Sido P. Cardiovascular manifestations in Marfan syndrome. Med Pharm Rep. 2021;94(Suppl No 1):S25–S27.
9. Salik I, Rawla P. Marfan Syndrome [Internet]. 2023 [updated 2023 Jan 23; cited 2025 Apr 22]. Available from: https://www.ncbi.nlm.nih.gov/books/NBK537339/.
10. de Beaufort HWL, Trimarchi S, Korach A, Di Eusanio M, Gilon D, Montgomery DG, Evangelista A, Braverman AC, Chen EP, Isselbacher EM, Gleason TG, De Vincentiis C, Sundt TM, Patel HJ, Eagle KA. Aortic dissection in patients with Marfan syndrome based on the IRAD data. Ann Cardiothorac Surg. 2017;6(6):633–641.

11. Martin C, Evangelista A, Serrano-Fiz S, Villar S, Ospina V, Martinez D, De Villarreal J, Sanchez V, Monivas V, Mingo S, Forteza A. Aortic Complications in Marfan Syndrome: Should We Anticipate Preventive Aortic Root Surgery? Ann Thorac Surg. 2020;109(6):1850–1857.

12. Polos M, Stengl R, Sulea CM, Benke K, Bartha E, Agg B, Koppanyi A, Hartyanszky I, Szekely A, Nemeth E, Kovacs A, Merkely B, Szabolcs Z. [Changing strategies in aortic root reconstruction in Marfan syndrome]. Orv Hetil. 2021;162(18):696–704.

13. Stengl R, Agg B, Polos M, Matyas G, Szabo G, Merkely B, Radovits T, Szabolcs Z, Benke K. Potential predictors of severe cardiovascular involvement in Marfan syndrome: the emphasized role of genotype-phenotype correlations in improving risk stratification-a literature review. Orphanet J Rare Dis. 2021;16(1):245.

14. Loeys BL, Dietz HC, Braverman AC, Callewaert BL, De Backer J, Devereux RB, Hilhorst-Hofstee Y, Jondeau G, Faivre L, Milewicz DM, Pyeritz RE, Sponseller PD, Wordsworth P, De Paepe AM. The revised Ghent nosology for the Marfan syndrome. J Med Genet. 2010;47(7):476–485.

15. Biery NJ, Eldadah ZA, Moore CS, Stetten G, Spencer F, Dietz HC. Revised genomic organization of FBN1 and significance for regulated gene expression. Genomics. 1999;56(1):70–77.

16. Pereira L, D'Alessio M, Ramirez F, Lynch JR, Sykes B, Pangilinan T, Bonadio J. Genomic organization of the sequence coding for fibrillin, the defective gene product in Marfan syndrome. Hum Mol Genet. 1993;2(7):961–968.

17. Collod-Beroud G, Le Bourdelles S, Ades L, Ala-Kokko L, Booms P, Boxer M, Child A, Comeglio P, De Paepe A, Hyland JC, Holman K, Kaitila I, Loeys B, Matyas G, Nuytinck L, Peltonen L, Rantamaki T, Robinson P, Steinmann B, Junien C, Beroud C, Boileau C. Update of the UMD-FBN1 mutation database and creation of an FBN1 polymorphism database. Hum Mutat. 2003;22(3):199–208.

18. Kielty CM, Rantamaki T, Child AH, Shuttleworth CA, Peltonen L. Cysteine-to-arginine point mutation in a 'hybrid' eight-cysteine domain of FBN1: consequences for fibrillin aggregation and microfibril assembly. J Cell Sci. 1995;108 (Pt 3):1317–1323.

19. Veitia RA. Exploring the molecular etiology of dominant-negative mutations. Plant Cell. 2007;19(12):3843–3851.

20. Reinhardt DP, Keene DR, Corson GM, Pöschl E, Bächinger HP, Gambee JE, Sakai LY. Fibrillin-1: organization in microfibrils and structural properties. J Mol Biol. 1996;258(1):104–116.

21. Suk JY, Jensen S, McGettrick A, Willis AC, Whiteman P, Redfield C, Handford PA. Structural consequences of cysteine substitutions C1977Y and C1977R in calcium-binding epidermal growth factor-like domain 30 of human fibrillin-1. J Biol Chem. 2004;279(49):51258–51265.

22. Mátyás G, Alonso S, Patrignani A, Marti M, Arnold E, Magyar I, Henggeler C, Carrel T, Steinmann B, Berger W. Large genomic fibrillin-1 (FBN1) gene deletions provide evidence for true haploinsufficiency in Marfan syndrome. Hum Genet. 2007;122(1):23–32.

23. Franken R, den Hartog AW, Radonic T, Micha D, Maugeri A, van Dijk FS, Meijers-Heijboer HE, Timmermans J, Scholte AJ, van den Berg MP, Groenink M, Mulder BJ, Zwinderman AH, de Waard V, Pals G. Beneficial Outcome of Losartan Therapy Depends on Type of FBN1 Mutation in Marfan Syndrome. Circ Cardiovasc Genet. 2015;8(2):383–388.

24. Robertson I, Jensen S, Handford P. TB domain proteins: evolutionary insights into the multifaceted roles of fibrillins and LTBPs. Biochem J. 2011;433(2):263–276.

25. Asano K, Cantalupo A, Sedes L, Ramirez F. The Multiple Functions of Fibrillin-1 Microfibrils in Organismal Physiology. Int J Mol Sci. 2022;23(3).

26. Schmelzer CEH, Duca L. Elastic fibers: formation, function, and fate during aging and disease. Febs j. 2022;289(13):3704–3730.

27. Thomson J, Singh M, Eckersley A, Cain SA, Sherratt MJ, Baldock C. Fibrillin microfibrils and elastic fibre proteins: Functional interactions and extracellular regulation of growth factors. Semin Cell Dev Biol. 2019;89:109–117.

28. Godwin ARF, Singh M, Lockhart-Cairns MP, Alanazi YF, Cain SA, Baldock C. The role of fibrillin and microfibril binding proteins in elastin and elastic fibre assembly. Matrix Biol. 2019;84:17–30.

29. Milewicz DM, Pyeritz RE, Crawford ES, Byers PH. Marfan syndrome: defective synthesis, secretion, and extracellular matrix formation of fibrillin by cultured dermal fibroblasts. J Clin Invest. 1992;89(1):79–86.

30. Knott V, Downing AK, Cardy CM, Handford P. Calcium binding properties of an epidermal growth factor-like domain pair from human fibrillin-1. J Mol Biol. 1996;255(1):22–27.

31. Reinhardt DP, Mechling DE, Boswell BA, Keene DR, Sakai LY, Bächinger HP. Calcium determines the shape of fibrillin. J Biol Chem. 1997;272(11):7368–7373.

32. Reinhardt DP, Ono RN, Sakai LY. Calcium stabilizes fibrillin-1 against proteolytic degradation. J Biol Chem. 1997;272(2):1231–1236.

33. Wess TJ, Purslow PP, Sherratt MJ, Ashworth J, Shuttleworth CA, Kielty CM. Calcium determines the supramolecular organization of fibrillin-rich microfibrils. J Cell Biol. 1998;141(3):829–837.

34. Jovanovic J, Takagi J, Choulier L, Abrescia NG, Stuart DI, van der Merwe PA, Mardon HJ, Handford PA. alphaVbeta6 is a novel receptor for human fibrillin-1. Comparative studies of molecular determinants underlying integrin-rgd affinity and specificity. J Biol Chem. 2007;282(9):6743–6751.

35. Zeyer KA, Reinhardt DP. Fibrillin-containing microfibrils are key signal relay stations for cell function. J Cell Commun Signal. 2015;9(4):309–325.

36. Jensen SA, Aspinall G, Handford PA. C-terminal propeptide is required for fibrillin-1 secretion and blocks premature assembly through linkage to domains cbEGF41-43. Proc Natl Acad Sci U S A. 2014;111(28):10155–10160.

37. Șulea CM, Mártonfalvi Z, Csányi C, Haluszka D, Pólos M, Ágg B, Stengl R, Benke K, Szabolcs Z, Kellermayer MSZ. Nanoscale Structural Comparison of Fibrillin-1 Microfibrils Isolated from Marfan and Non-Marfan Syndrome Human Aorta. Int J Mol Sci. 2023;24(8).

38. Cain SA, Baldock C, Gallagher J, Morgan A, Bax DV, Weiss AS, Shuttleworth CA, Kielty CM. Fibrillin-1 interactions with heparin. Implications for microfibril and elastic fiber assembly. J Biol Chem. 2005;280(34):30526–30537.

39. Isogai Z, Aspberg A, Keene DR, Ono RN, Reinhardt DP, Sakai LY. Versican interacts with fibrillin-1 and links extracellular microfibrils to other connective tissue networks. J Biol Chem. 2002;277(6):4565–4572.

40. Isogai Z, Ono RN, Ushiro S, Keene DR, Chen Y, Mazzieri R, Charbonneau NL, Reinhardt DP, Rifkin DB, Sakai LY. Latent transforming growth factor beta-binding

protein 1 interacts with fibrillin and is a microfibril-associated protein. J Biol Chem. 2003;278(4):2750–2757.

41. Jensen SA, Reinhardt DP, Gibson MA, Weiss AS. Protein interaction studies of MAGP-1 with tropoelastin and fibrillin-1. J Biol Chem. 2001;276(43):39661–39666.

42. Lin G, Tiedemann K, Vollbrandt T, Peters H, Batge B, Brinckmann J, Reinhardt DP. Homo- and heterotypic fibrillin-1 and -2 interactions constitute the basis for the assembly of microfibrils. J Biol Chem. 2002;277(52):50795–50804.

43. Reinhardt DP, Sasaki T, Dzamba BJ, Keene DR, Chu ML, Göhring W, Timpl R, Sakai LY. Fibrillin-1 and fibulin-2 interact and are colocalized in some tissues. J Biol Chem. 1996;271(32):19489–19496.

44. Cheifetz S, Weatherbee JA, Tsang ML, Anderson JK, Mole JE, Lucas R, Massagué J. The transforming growth factor-beta system, a complex pattern of cross-reactive ligands and receptors. Cell. 1987;48(3):409–415.

45. Derynck R, Jarrett JA, Chen EY, Eaton DH, Bell JR, Assoian RK, Roberts AB, Sporn MB, Goeddel DV. Human transforming growth factor-beta complementary DNA sequence and expression in normal and transformed cells. Nature. 1985;316(6030):701–705.

46. Derynck R, Lindquist PB, Lee A, Wen D, Tamm J, Graycar JL, Rhee L, Mason AJ, Miller DA, Coffey RJ, et al. A new type of transforming growth factor-beta, TGF-beta 3. Embo j. 1988;7(12):3737–3743.

47. Massagué J, Xi Q. TGF-β control of stem cell differentiation genes. FEBS Lett. 2012;586(14):1953–1958.

48. Nakao A, Imamura T, Souchelnytskyi S, Kawabata M, Ishisaki A, Oeda E, Tamaki K, Hanai J, Heldin CH, Miyazono K, ten Dijke P. TGF-beta receptor-mediated signalling through Smad2, Smad3 and Smad4. Embo j. 1997;16(17):5353–5362.

49. Deng Z, Fan T, Xiao C, Tian H, Zheng Y, Li C, He J. TGF-β signaling in health, disease, and therapeutics. Signal Transduct Target Ther. 2024;9(1):61.

50. Shi M, Zhu J, Wang R, Chen X, Mi L, Walz T, Springer TA. Latent TGF-β structure and activation. Nature. 2011;474(7351):343–349.

51. Miyazono K, Olofsson A, Colosetti P, Heldin CH. A role of the latent TGF-beta 1-binding protein in the assembly and secretion of TGF-beta 1. Embo j. 1991;10(5):1091–1101.

52. Taipale J, Miyazono K, Heldin CH, Keski-Oja J. Latent transforming growth factor-beta 1 associates to fibroblast extracellular matrix via latent TGF-beta binding protein. J Cell Biol. 1994;124(1-2):171–181.

53. Benke K, Ágg B, Szilveszter B, Tarr F, Nagy ZB, Pólos M, Daróczi L, Merkely B, Szabolcs Z. The role of transforming growth factor-beta in Marfan syndrome. Cardiol J. 2013;20(3):227–234.

54. Morikawa M, Derynck R, Miyazono K. TGF-β and the TGF-β Family: Context-Dependent Roles in Cell and Tissue Physiology. Cold Spring Harb Perspect Biol. 2016;8(5).

55. Jones JA, Spinale FG, Ikonomidis JS. Transforming growth factor-beta signaling in thoracic aortic aneurysm development: a paradox in pathogenesis. J Vasc Res. 2009;46(2):119–137.

56. Neptune ER, Frischmeyer PA, Arking DE, Myers L, Bunton TE, Gayraud B, Ramirez F, Sakai LY, Dietz HC. Dysregulation of TGF-beta activation contributes to pathogenesis in Marfan syndrome. Nat Genet. 2003;33(3):407–411.

57. Roberts AB, Sporn MB, Assoian RK, Smith JM, Roche NS, Wakefield LM, Heine UI, Liotta LA, Falanga V, Kehrl JH, et al. Transforming growth factor type beta: rapid induction of fibrosis and angiogenesis in vivo and stimulation of collagen formation in vitro. Proc Natl Acad Sci U S A. 1986;83(12):4167–4171.

58. Sime PJ, Xing Z, Graham FL, Csaky KG, Gauldie J. Adenovector-mediated gene transfer of active transforming growth factor-beta1 induces prolonged severe fibrosis in rat lung. J Clin Invest. 1997;100(4):768–776.

59. Agg B, Benke K, Szilveszter B, Pólos M, Daróczi L, Odler B, Nagy ZB, Tarr F, Merkely B, Szabolcs Z. Possible extracardiac predictors of aortic dissection in Marfan syndrome. BMC Cardiovasc Disord. 2014;14:47.

60. Franken R, den Hartog AW, de Waard V, Engele L, Radonic T, Lutter R, Timmermans J, Scholte AJ, van den Berg MP, Zwinderman AH, Groenink M, Mulder BJ. Circulating transforming growth factor-β as a prognostic biomarker in Marfan syndrome. Int J Cardiol. 2013;168(3):2441–2446.

61. Kielty CM, Sherratt MJ, Marson A, Baldock C. Fibrillin microfibrils. Adv Protein Chem. 2005;70:405–436.

62. Gayraud B, Keene DR, Sakai LY, Ramirez F. New insights into the assembly of extracellular microfibrils from the analysis of the fibrillin 1 mutation in the tight skin mouse. J Cell Biol. 2000;150(3):667–680.

63. Koenders MM, Wismans RG, Starcher B, Hamel BC, Dekhuijzen RP, van Kuppevelt TH. Fibrillin-1 staining anomalies are associated with increased staining for TGF-beta and elastic fibre degradation; new clues to the pathogenesis of emphysema. J Pathol. 2009;218(4):446–457.

64. Lamireau T, Dubuisson L, Lepreux S, Bioulac-Sage P, Fabre M, Rosenbaum J, Desmoulière A. Abnormal hepatic expression of fibrillin-1 in children with cholestasis. Am J Surg Pathol. 2002;26(5):637–646.

65. Sedes L, Wondimu E, Crockett B, Hansen J, Cantalupo A, Asano K, Iyengar R, Rifkin DB, Smaldone S, Ramirez F. Fibrillin-1 deficiency in the outer perichondrium causes longitudinal bone overgrowth in mice with Marfan syndrome. Hum Mol Genet. 2022;31(19):3281–3289.

66. Tiedemann K, Sasaki T, Gustafsson E, Göhring W, Bätge B, Notbohm H, Timpl R, Wedel T, Schlötzer-Schrehardt U, Reinhardt DP. Microfibrils at basement membrane zones interact with perlecan via fibrillin-1. J Biol Chem. 2005;280(12):11404–11412.

67. Heinz A. Elastic fibers during aging and disease. Ageing Res Rev. 2021;66:101255.

68. Li L, Liao J, Yuan Q, Hong X, Li J, Peng Y, He M, Zhu H, Zhu M, Hou FF, Fu H, Liu Y. Fibrillin-1-enriched microenvironment drives endothelial injury and vascular rarefaction in chronic kidney disease. Sci Adv. 2021;7(5).

69. Zhang Y, Liu XJ, Zhai XR, Yao Y, Shao B, Zhen YH, Zhang X, Xiao Z, Wang LF, Zhang ML, Chen ZM. Knockdown of fibrillin-1 suppresses retina-blood barrier dysfunction by inhibiting vascular endothelial apoptosis under diabetic conditions. Int J Ophthalmol. 2024;17(8):1403–1410.

70. Marson A, Rock MJ, Cain SA, Freeman LJ, Morgan A, Mellody K, Shuttleworth CA, Baldock C, Kielty CM. Homotypic fibrillin-1 interactions in microfibril assembly. J Biol Chem. 2005;280(6):5013–5021.

71. Li L, Huang J, Liu Y. The extracellular matrix glycoprotein fibrillin-1 in health and disease. Front Cell Dev Biol. 2023;11:1302285.

72. Godwin ARF, Dajani R, Zhang X, Thomson J, Holmes DF, Adamo CS, Sengle G, Sherratt MJ, Roseman AM, Baldock C. Fibrillin microfibril structure identifies long-range effects of inherited pathogenic mutations affecting a key regulatory latent TGFβ-binding site. Nat Struct Mol Biol. 2023;30(5):608–618.

73. Baldock C, Koster AJ, Ziese U, Rock MJ, Sherratt MJ, Kadler KE, Shuttleworth CA, Kielty CM. The supramolecular organization of fibrillin-rich microfibrils. J Cell Biol. 2001;152(5):1045–1056.

74. Sherratt MJ, Holmes DF, Shuttleworth CA, Kielty CM. Scanning transmission electron microscopy mass analysis of fibrillin-containing microfibrils from foetal elastic tissues. Int J Biochem Cell Biol. 1997;29(8-9):1063–1070.

75. Hanssen E, Franc S, Garrone R. Atomic force microscopy and modeling of natural elastic fibrillin polymers. Biol Cell. 1998;90(3):223–228.

76. Sherratt MJ, Wess TJ, Baldock C, Ashworth J, Purslow PP, Shuttleworth CA, Kielty CM. Fibrillin-rich microfibrils of the extracellular matrix: ultrastructure and assembly. Micron. 2001;32(2):185–200.

77. Eckersley A, Mellody KT, Pilkington S, Griffiths CEM, Watson REB, O'Cualain R, Baldock C, Knight D, Sherratt MJ. Structural and compositional diversity of fibrillin microfibrils in human tissues. J Biol Chem. 2018;293(14):5117–5133.

78. Kielty CM. Fell-Muir Lecture: Fibrillin microfibrils: structural tensometers of elastic tissues? Int J Exp Pathol. 2017;98(4):172–190.

79. Sakai LY, Keene DR, Glanville RW, Bächinger HP. Purification and partial characterization of fibrillin, a cysteine-rich structural component of connective tissue microfibrils. J Biol Chem. 1991;266(22):14763–14770.

80. Baldock C, Siegler V, Bax DV, Cain SA, Mellody KT, Marson A, Haston JL, Berry R, Wang MC, Grossmann JG, Roessle M, Kielty CM, Wess TJ. Nanostructure of fibrillin-1 reveals compact conformation of EGF arrays and mechanism for extensibility. Proc Natl Acad Sci U S A. 2006;103(32):11922–11927.

81. Handford PA, Downing AK, Reinhardt DP, Sakai LY. Fibrillin: from domain structure to supramolecular assembly. Matrix Biol. 2000;19(6):457–470.

82. Kuo CL, Isogai Z, Keene DR, Hazeki N, Ono RN, Sengle G, Bächinger HP, Sakai LY. Effects of fibrillin-1 degradation on microfibril ultrastructure. J Biol Chem. 2007;282(6):4007–4020.

83. Godwin ARF, Starborg T, Smith DJ, Sherratt MJ, Roseman AM, Baldock C. Multiscale Imaging Reveals the Hierarchical Organization of Fibrillin Microfibrils. J Mol Biol. 2018;430(21):4142–4155.

84. Jones W, Rodriguez J, Bassnett S. Targeted deletion of fibrillin-1 in the mouse eye results in ectopia lentis and other ocular phenotypes associated with Marfan syndrome. Dis Model Mech. 2019;12(1).

85. Sherratt MJ, Baldock C, Haston JL, Holmes DF, Jones CJ, Shuttleworth CA, Wess TJ, Kielty CM. Fibrillin microfibrils are stiff reinforcing fibres in compliant tissues. J Mol Biol. 2003;332(1):183–193.

86. Morgan M, Elfeky M, Gamage P, Bell D, Knipe H. Young's modulus. Reference article [Internet]. 2014 [updated 2020 Mar 31; cited 2025 May 21]. Available from: https://radiopaedia.org/articles/youngs-modulus.

87. Thurmond F, Trotter J. Morphology and biomechanics of the microfibrillar network of sea cucumber dermis. J Exp Biol. 1996;199(Pt 8):1817–1828.

88. Lillie MA, David GJ, Gosline JM. Mechanical role of elastin-associated microfibrils in pig aortic elastic tissue. Connect Tissue Res. 1998;37(1-2):121–141.

89. Shadwick RE, Gosline JM. Elastic arteries in invertebrates: mechanics of the octopus aorta. Science. 1981;213(4509):759–761.

90. Koenders MM, Yang L, Wismans RG, van der Werf KO, Reinhardt DP, Daamen W, Bennink ML, Dijkstra PJ, van Kuppevelt TH, Feijen J. Microscale mechanical properties of single elastic fibers: the role of fibrillin-microfibrils. Biomaterials. 2009;30(13):2425–2432.

91. Megill WM, Gosline JM, Blake RW. The modulus of elasticity of fibrillin-containing elastic fibres in the mesoglea of the hydromedusa Polyorchis penicillatus. J Exp Biol. 2005;208(Pt 20):3819–3834.

92. McConnell CJ, Wright GM, DeMont ME. The modulus of elasticity of lobster aorta microfibrils. Experientia. 1996;52(9):918–921.

93. Wright DM, Duance VC, Wess TJ, Kielty CM, Purslow PP. The supramolecular organisation of fibrillin-rich microfibrils determines the mechanical properties of bovine zonular filaments. J Exp Biol. 1999;202(Pt 21):3011–3020.

94. Gasser TC. Modeling the Structural and Mechanical Properties of the Normal and Aneurysmatic Aortic Wall. In: Zhang Y, editor. Multi-scale Extracellular Matrix

Mechanics and Mechanobiology. Cham: Springer International Publishing; 2019. 55–82 p.

95. Díaz de Bustamante A, Ruiz-Casares E, Darnaude MT, Perucho T, Martínez-Quesada G. Phenotypic variability in Marfan syndrome in a family with a novel nonsense FBN1 gene mutation. Rev Esp Cardiol (Engl Ed). 2012;65(4):380–381.

96. Pollock L, Ridout A, Teh J, Nnadi C, Stavroulias D, Pitcher A, Blair E, Wordsworth P, Vincent TL. The Musculoskeletal Manifestations of Marfan Syndrome: Diagnosis, Impact, and Management. Curr Rheumatol Rep. 2021;23(11):81.

97. Andersen NH, Hauge EM, Baad-Hansen T, Groth KA, Berglund A, Gravholt CH, Stochholm K. Musculoskeletal diseases in Marfan syndrome: a nationwide registry study. Orphanet J Rare Dis. 2022;17(1):118.

98. Esfandiari H, Ansari S, Mohammad-Rabei H, Mets MB. Management Strategies of Ocular Abnormalities in Patients with Marfan Syndrome: Current Perspective. J Ophthalmic Vis Res. 2019;14(1):71–77.

99. Kjeldsen S, Andersen N, Groth K, Larsen D, Hjortdal J, Berglund A, Gravholt C, Stochholm K. Ocular morbidity in Marfan syndrome: a nationwide epidemiological study. Br J Ophthalmol. 2023;107(8):1051–1055.

100. Kolonics-Farkas AM, Agg B, Benke K, Odler B, Bohacs A, Kovats Z, Szabolcs Z, Müller V. Lung Function Changes are More Common in Marfan Patients Who Need Major Thoracic Surgery. Lung. 2019;197(4):465–472.

101. Kolonics-Farkas AM, Kovats Z, Bohacs A, Odler B, Benke K, Agg B, Szabolcs Z, Müller V. Airway obstruction can be better predicted using Global Lung Function Initiative spirometry reference equations in Marfan syndrome. Physiol Int. 2021.

102. Seeburun S, Wu S, Hemani D, Pham L, Ju D, Xie Y, Kata P, Li L. Insights into elastic fiber fragmentation: Mechanisms and treatment of aortic aneurysm in Marfan syndrome. Vascul Pharmacol. 2023;153:107215.

103. Azadani AN, Chitsaz S, Matthews PB, Jaussaud N, Leung J, Tsinman T, Ge L, Tseng EE. Comparison of mechanical properties of human ascending aorta and aortic sinuses. Ann Thorac Surg. 2012;93(1):87–94.

104. Isselbacher EM, Preventza O, Hamilton Black Iii J, Augoustides JG, Beck AW, Bolen MA, Braverman AC, Bray BE, Brown-Zimmerman MM, Chen EP, Collins TJ, DeAnda A, Jr., Fanola CL, Girardi LN, Hicks CW, Hui DS, Jones WS, Kalahasti V, Kim

KM, Milewicz DM, Oderich GS, Ogbechie L, Promes SB, Ross EG, Schermerhorn ML, Times SS, Tseng EE, Wang GJ, Woo YJ. 2022 ACC/AHA Guideline for the Diagnosis and Management of Aortic Disease: A Report of the American Heart Association/American College of Cardiology Joint Committee on Clinical Practice Guidelines. J Am Coll Cardiol. 2022;80(24):e223–e393.

105. Devereux RB, de Simone G, Arnett DK, Best LG, Boerwinkle E, Howard BV, Kitzman D, Lee ET, Mosley TH, Jr., Weder A, Roman MJ. Normal limits in relation to age, body size and gender of two-dimensional echocardiographic aortic root dimensions in persons ≥15 years of age. Am J Cardiol. 2012;110(8):1189–1194.

106. Wozniak-Mielczarek L, Sabiniewicz R, Drezek-Nojowicz M, Nowak R, Gilis-Malinowska N, Mielczarek M, Łabuc A, Waldoch A, Wierzba J. Differences in Cardiovascular Manifestation of Marfan Syndrome Between Children and Adults. Pediatr Cardiol. 2019;40(2):393–403.

107. Détaint D, Faivre L, Collod-Beroud G, Child AH, Loeys BL, Binquet C, Gautier E, Arbustini E, Mayer K, Arslan-Kirchner M, Stheneur C, Halliday D, Beroud C, Bonithon-Kopp C, Claustres M, Plauchu H, Robinson PN, Kiotsekoglou A, De Backer J, Adès L, Francke U, De Paepe A, Boileau C, Jondeau G. Cardiovascular manifestations in men and women carrying a FBN1 mutation. Eur Heart J. 2010;31(18):2223–2229.

108. Faivre L, Collod-Beroud G, Loeys BL, Child A, Binquet C, Gautier E, Callewaert B, Arbustini E, Mayer K, Arslan-Kirchner M, Kiotsekoglou A, Comeglio P, Marziliano N, Dietz HC, Halliday D, Beroud C, Bonithon-Kopp C, Claustres M, Muti C, Plauchu H, Robinson PN, Adès LC, Biggin A, Benetts B, Brett M, Holman KJ, De Backer J, Coucke P, Francke U, De Paepe A, Jondeau G, Boileau C. Effect of mutation type and location on clinical outcome in 1,013 probands with Marfan syndrome or related phenotypes and FBN1 mutations: an international study. Am J Hum Genet. 2007;81(3):454–466.

109. Saeyeldin A, Zafar MA, Velasquez CA, Ip K, Gryaznov A, Brownstein AJ, Li Y, Rizzo JA, Erben Y, Ziganshin BA, Elefteriades JA. Natural history of aortic root aneurysms in Marfan syndrome. Ann Cardiothorac Surg. 2017;6(6):625–632.

110. Elsayed RS, Cohen RG, Fleischman F, Bowdish ME. Acute Type A Aortic Dissection. Cardiol Clin. 2017;35(3):331–345.

111. Evangelista A, Isselbacher EM, Bossone E, Gleason TG, Eusanio MD, Sechtem U, Ehrlich MP, Trimarchi S, Braverman AC, Myrmel T, Harris KM, Hutchinson S, O'Gara

P, Suzuki T, Nienaber CA, Eagle KA. Insights From the International Registry of Acute Aortic Dissection: A 20-Year Experience of Collaborative Clinical Research. Circulation. 2018;137(17):1846–1860.

112. Sheikhzadeh S, De Backer J, Gorgan NR, Rybczynski M, Hillebrand M, Schüler H, Bernhardt AM, Koschyk D, Bannas P, Keyser B, Mortensen K, Radke RM, Mir TS, Kölbel T, Robinson PN, Schmidtke J, Berger J, Blankenberg S, von Kodolitsch Y. The main pulmonary artery in adults: a controlled multicenter study with assessment of echocardiographic reference values, and the frequency of dilatation and aneurysm in Marfan syndrome. Orphanet J Rare Dis. 2014;9:203.

113. Stark VC, Huemmer M, Olfe J, Mueller GC, Kozlik-Feldmann R, Mir TS. The Pulmonary Artery in Pediatric Patients with Marfan Syndrome: An Underestimated Aspect of the Disease. Pediatr Cardiol. 2018;39(6):1194–1199.

114. Dietz H. FBN1-Related Marfan Syndrome [Internet]. 2001 [updated 2022 Feb 17; cited 2025 May 24]. Available from: https://www.ncbi.nlm.nih.gov/books/NBK1335/.

115. Ágg B, Szilveszter B, Daradics N, Benke K, Stengl R, Kolossváry M, Pólos M, Radovits T, Ferdinandy P, Merkely B, Maurovich-Horvat P, Szabolcs Z. Increased visceral arterial tortuosity in Marfan syndrome. Orphanet J Rare Dis. 2020;15(1):91.

116. Ghoraba HH, Moshfeghi DM. Retinal Arterial Tortuosity in Marfan and Loeys-Dietz Syndromes. Ophthalmol Retina. 2023;7(6):554–557.

117. Spinardi L, Vornetti G, De Martino S, Golfieri R, Faccioli L, Pastore Trossello M, Graziano C, Mariucci E, Donti A. Intracranial Arterial Tortuosity in Marfan Syndrome and Loeys-Dietz Syndrome: Tortuosity Index Evaluation Is Useful in the Differential Diagnosis. AJNR Am J Neuroradiol. 2020;41(10):1916–1922.

118. Ciurică S, Lopez-Sublet M, Loeys BL, Radhouani I, Natarajan N, Vikkula M, Maas A, Adlam D, Persu A. Arterial Tortuosity. Hypertension. 2019;73(5):951–960.

119. Franken R, El Morabit A, de Waard V, Timmermans J, Scholte AJ, van den Berg MP, Marquering H, Planken NR, Zwinderman AH, Mulder BJ, Groenink M. Increased aortic tortuosity indicates a more severe aortic phenotype in adults with Marfan syndrome. Int J Cardiol. 2015;194:7–12.

120. Milewicz DM, Dietz HC, Miller DC. Treatment of aortic disease in patients with Marfan syndrome. Circulation. 2005;111(11):e150–157.

121. Thacoor A. Mitral valve prolapse and Marfan syndrome. Congenit Heart Dis. 2017;12(4):430–434.

122. Demolder A, Timmermans F, Duytschaever M, Muiño-Mosquera L, De Backer J. Association of Mitral Annular Disjunction With Cardiovascular Outcomes Among Patients With Marfan Syndrome. JAMA Cardiol. 2021;6(10):1177–1186.

123. Gu X, He Y, Li Z, Han J, Chen J, Nixon JV. Echocardiographic versus histologic findings in Marfan syndrome. Tex Heart Inst J. 2015;42(1):30–34.

124. Marelli S, Micaglio E, Taurino J, Salvi P, Rurali E, Perrucci GL, Dolci C, Udugampolage NS, Caruso R, Gentilini D, Trifiro G, Callus E, Frigiola A, De Vincentiis C, Pappone C, Parati G, Pini A. Marfan Syndrome: Enhanced Diagnostic Tools and Follow-up Management Strategies. Diagnostics (Basel). 2023;13(13).

125. Alpendurada F, Wong J, Kiotsekoglou A, Banya W, Child A, Prasad SK, Pennell DJ, Mohiaddin RH. Evidence for Marfan cardiomyopathy. Eur J Heart Fail. 2010;12(10):1085–1091.

126. De Backer JF, Devos D, Segers P, Matthys D, François K, Gillebert TC, De Paepe AM, De Sutter J. Primary impairment of left ventricular function in Marfan syndrome. Int J Cardiol. 2006;112(3):353–358.

127. Hetzer R, Siegel G, Delmo Walter EM. Cardiomyopathy in Marfan syndrome. Eur J Cardiothorac Surg. 2016;49(2):561–567; discussion 567–568.

128. Winther S, Williams LK, Keir M, Connelly KA, Bradley TJ, Rakowski H, Crean AM. Cardiovascular Magnetic Resonance Provides Evidence of Abnormal Myocardial Strain and Primary Cardiomyopathy in Marfan syndrome. J Comput Assist Tomogr. 2019;43(3):410–415.

129. Steijns F, van Hengel J, Sips P, De Backer J, Renard M. A heart for fibrillin: spatial arrangement in adult wild-type murine myocardial tissue. Histochem Cell Biol. 2018;150(3):271–280.

130. Rouf R, MacFarlane EG, Takimoto E, Chaudhary R, Nagpal V, Rainer PP, Bindman JG, Gerber EE, Bedja D, Schiefer C, Miller KL, Zhu G, Myers L, Amat-Alarcon N, Lee DI, Koitabashi N, Judge DP, Kass DA, Dietz HC. Nonmyocyte ERK1/2 signaling contributes to load-induced cardiomyopathy in Marfan mice. JCI Insight. 2017;2(15).

131. Hershberger RE, Hedges DJ, Morales A. Dilated cardiomyopathy: the complexity of a diverse genetic architecture. Nat Rev Cardiol. 2013;10(9):531–547.

132. Labeit S, Kolmerer B, Linke WA. The giant protein titin. Emerging roles in physiology and pathophysiology. Circ Res. 1997;80(2):290–294.
133. Granzier HL, Irving TC. Passive tension in cardiac muscle: contribution of collagen, titin, microtubules, and intermediate filaments. Biophys J. 1995;68(3):1027–1044.
134. Sziklai D, Sallai J, Papp Z, Kellermayer D, Mártonfalvi Z, Pires RH, Kellermayer MSZ. Nanosurgical Manipulation of Titin and Its M-Complex. Nanomaterials (Basel). 2022;12(2).
135. Loescher CM, Hobbach AJ, Linke WA. Titin (TTN): from molecule to modifications, mechanics, and medical significance. Cardiovasc Res. 2022;118(14):2903–2918.
136. Cazorla O, Freiburg A, Helmes M, Centner T, McNabb M, Wu Y, Trombitás K, Labeit S, Granzier H. Differential expression of cardiac titin isoforms and modulation of cellular stiffness. Circ Res. 2000;86(1):59–67.
137. Nagueh SF, Shah G, Wu Y, Torre-Amione G, King NM, Lahmers S, Witt CC, Becker K, Labeit S, Granzier HL. Altered titin expression, myocardial stiffness, and left ventricular function in patients with dilated cardiomyopathy. Circulation. 2004;110(2):155–162.
138. Neagoe C, Kulke M, del Monte F, Gwathmey JK, de Tombe PP, Hajjar RJ, Linke WA. Titin isoform switch in ischemic human heart disease. Circulation. 2002;106(11):1333–1341.
139. Kellermayer D, Kiss B, Tordai H, Oláh A, Granzier HL, Merkely B, Kellermayer M, Radovits T. Increased Expression of N2BA Titin Corresponds to More Compliant Myofibrils in Athlete's Heart. Int J Mol Sci. 2021;22(20).
140. Kellermayer D, Smith JE, 3rd, Granzier H. Novex-3, the tiny titin of muscle. Biophys Rev. 2017;9(3):201–206.
141. Franken R, Groenink M, de Waard V, Feenstra HM, Scholte AJ, van den Berg MP, Pals G, Zwinderman AH, Timmermans J, Mulder BJ. Genotype impacts survival in Marfan syndrome. Eur Heart J. 2016;37(43):3285–3290.
142. Renard M, Francis C, Ghosh R, Scott AF, Witmer PD, Adès LC, Andelfinger GU, Arnaud P, Boileau C, Callewaert BL, Guo D, Hanna N, Lindsay ME, Morisaki H, Morisaki T, Pachter N, Robert L, Van Laer L, Dietz HC, Loeys BL, Milewicz DM, De

Backer J. Clinical Validity of Genes for Heritable Thoracic Aortic Aneurysm and Dissection. J Am Coll Cardiol. 2018;72(6):605–615.

143. Monda E, Lioncino M, Verrillo F, Rubino M, Caiazza M, Mauriello A, Guarnaccia N, Fusco A, Cirillo A, Covino S, Altobelli I, Diana G, Palmiero G, Dongiglio F, Natale F, Cesaro A, Bossone E, Russo MG, Calabrò P, Limongelli G. The Role of Genetic Testing in Patients with Heritable Thoracic Aortic Diseases. Diagnostics (Basel). 2023;13(4).

144. Caruana M, Baars MJ, Bashiardes E, Benke K, Björck E, Codreanu A, de Moya Rubio E, Dumfarth J, Evangelista A, Groenink M, Kallenbach K, Kempers M, Keravnou A, Loeys B, Muiño-Mosquera L, Nagy E, Milleron O, Nistri S, Pepe G, Roos-Hesselink J, Szabolcs Z, Teixidó-Tura G, Timmermans J, Van de Laar I, van Kimmenade R, Verstraeten A, Von Kodolitsch Y, De Backer J, Jondeau G. HTAD patient pathway: Strategy for diagnostic work-up of patients and families with (suspected) heritable thoracic aortic diseases (HTAD). A statement from the HTAD working group of VASCERN. Eur J Med Genet. 2023;66(1):104673.

145. Meester JAN, Verstraeten A, Schepers D, Alaerts M, Van Laer L, Loeys BL. Differences in manifestations of Marfan syndrome, Ehlers-Danlos syndrome, and Loeys-Dietz syndrome. Ann Cardiothorac Surg. 2017;6(6):582–594.

146. Callewaert B. Congenital Contractural Arachnodactyly [Internet]. 2001 [updated 2022 Jul 14; cited 2025 Jun 8]. Available from: https://www.ncbi.nlm.nih.gov/books/NBK1386/.

147. Becerra-Muñoz VM, Gómez-Doblas JJ, Porras-Martín C, Such-Martínez M, Crespo-Leiro MG, Barriales-Villa R, de Teresa-Galván E, Jiménez-Navarro M, Cabrera-Bueno F. The importance of genotype-phenotype correlation in the clinical management of Marfan syndrome. Orphanet J Rare Dis. 2018;13(1):16.

148. Pugnaloni F, De Rose DU, Digilio MC, Magliozzi M, Braguglia A, Valfrè L, Toscano A, Dotta A, Di Pede A. Neonatal Marfan syndrome: a case report of a novel fibrillin 1 mutation, with genotype-phenotype correlation and brief review of the literature. Ital J Pediatr. 2024;50(1):183.

149. Godfrey M, Raghunath M, Cisler J, Bevins CL, DePaepe A, Di Rocco M, Gregoritch J, Imaizumi K, Kaplan P, Kuroki Y, et al. Abnormal morphology of fibrillin microfibrils in fibroblast cultures from patients with neonatal Marfan syndrome. Am J Pathol. 1995;146(6):1414–1421.

150. Pereira L, Lee SY, Gayraud B, Andrikopoulos K, Shapiro SD, Bunton T, Biery NJ, Dietz HC, Sakai LY, Ramirez F. Pathogenetic sequence for aneurysm revealed in mice underexpressing fibrillin-1. Proc Natl Acad Sci U S A. 1999;96(7):3819–3823.

151. Vahanian A, Beyersdorf F, Praz F, Milojevic M, Baldus S, Bauersachs J, Capodanno D, Conradi L, De Bonis M, De Paulis R, Delgado V, Freemantle N, Gilard M, Haugaa KH, Jeppsson A, Jüni P, Pierard L, Prendergast BD, Sádaba JR, Tribouilloy C, Wojakowski W. 2021 ESC/EACTS Guidelines for the management of valvular heart disease. Eur Heart J. 2022;43(7):561–632.

152. Benke K, Ágg B, Szabó L, Szilveszter B, Odler B, Pólos M, Cao C, Maurovich-Horvat P, Radovits T, Merkely B, Szabolcs Z. Bentall procedure: quarter century of clinical experiences of a single surgeon. J Cardiothorac Surg. 2016;11:19.

153. Benke K, Ágg B, Pólos M, Sayour AA, Radovits T, Bartha E, Nagy P, Rákóczi B, Koller Á, Szokolai V, Hedberg J, Merkely B, Nagy ZB, Szabolcs Z. The effects of acute and elective cardiac surgery on the anxiety traits of patients with Marfan syndrome. BMC Psychiatry. 2017;17(1):253.

154. Pólos M, Benke K, Ágg B, Stengl R, Szabó A, Nagy Á, Ruskó B, Hedberg J, Radovits T, Susánszky É, Merkely B, Székely A, Szabolcs Z. Psychological factors affecting Marfan syndrome patients with or without cardiac surgery. Ann Palliat Med. 2020;9(5):3007–3017.

155. Agota A, Agg B, Benke K, Joó JG, Langmár Z, Marosi K, Lelovics Z, Deé K, Nagy P, Köles B, Horváth E, Crespo Z, Szabolcs Z, Nagy ZB. [The establishment of the Marfan syndrome biobank in Hungary]. Orv Hetil. 2012;153(8):296–302.

156. Cox T, Comerford EJ, Wegg M, Mills A, Barrett SD, Smith KD, Sherratt MJ, Akhtar R. Investigation of fibrillin microfibrils in the canine cruciate ligament in dogs with different predispositions to ligament rupture. Res Vet Sci. 2020;133:53–58.

157. Kielty CM, Cummings C, Whittaker SP, Shuttleworth CA, Grant ME. Isolation and ultrastructural analysis of microfibrillar structures from foetal bovine elastic tissues. Relative abundance and supramolecular architecture of type VI collagen assemblies and fibrillin. J Cell Sci. 1991;99 (Pt 4):797–807.

158. Dufrêne YF, Ando T, Garcia R, Alsteens D, Martinez-Martin D, Engel A, Gerber C, Müller DJ. Imaging modes of atomic force microscopy for application in molecular and cell biology. Nat Nanotechnol. 2017;12(4):295–307.

159. Nečas DK, P. Gwyddion: an open-source software for SPM data analysis. Centr Eur J Phys. 2012;10:181–188.

160. Kellermayer D, Șulea CM, Tordai H, Benke K, Pólos M, Ágg B, Stengl R, Csonka M, Radovits T, Merkely B, Szabolcs Z, Kellermayer M, Kiss B. Marfan syndrome cardiomyocytes show excess of titin isoform N2BA and extended sarcomeric M-band. J Gen Physiol. 2025;157(3).

161. Kellermayer D, Tordai H, Kiss B, Török G, Péter DM, Sayour AA, Pólos M, Hartyánszky I, Szilveszter B, Labeit S, Gángó A, Bedics G, Bödör C, Radovits T, Merkely B, Kellermayer MS. Truncated titin is structurally integrated into the human dilated cardiomyopathic sarcomere. J Clin Invest. 2024;134(2).

162. Béroud C, Collod-Béroud G, Boileau C, Soussi T, Junien C. UMD (Universal mutation database): a generic software to build and analyze locus-specific databases. Hum Mutat. 2000;15(1):86–94.

163. UniProt Consortium. UniProt: the Universal Protein Knowledgebase in 2025. Nucleic Acids Res. 2025;53(D1):D609–D617.

164. Comeglio P, Johnson P, Arno G, Brice G, Evans A, Aragon-Martin J, da Silva FP, Kiotsekoglou A, Child A. The importance of mutation detection in Marfan syndrome and Marfan-related disorders: report of 193 FBN1 mutations. Hum Mutat. 2007;28(9):928.

165. Madar L, Szakszon K, Pfliegler G, Szabó GP, Brúgós B, Ronen N, Papp J, Zahuczky K, Szakos E, Fekete G, Oláh É, Koczok K, Balogh I. FBN1 gene mutations in 26 Hungarian patients with suspected Marfan syndrome or related fibrillinopathies. J Biotechnol. 2019;301:105–111.

166. Yum HR, Kim SE, Shin SY, Park SH. Identification of a fibrillin-1 gene mutation in a monozygotic twin presenting with bilateral juvenile-onset ectopia lentis. Korean J Ophthalmol. 2015;29(1):77–78.

167. Lebreiro A, Martins E, Cruz C, Almeida J, Pimenta S, Bernardes M, Carlos Machado J, Júlia Maciel M, Abreu-Lima C. [Genotypic characterization of a Portuguese population of Marfan syndrome patients]. Rev Port Cardiol. 2011;30(7-8):649–654.

168. Rommel K, Karck M, Haverich A, von Kodolitsch Y, Rybczynski M, Müller G, Singh KK, Schmidtke J, Arslan-Kirchner M. Identification of 29 novel and nine recurrent fibrillin-1 (FBN1) mutations and genotype-phenotype correlations in 76 patients with Marfan syndrome. Hum Mutat. 2005;26(6):529–539.

169. Attanasio M, Lapini I, Evangelisti L, Lucarini L, Giusti B, Porciani M, Fattori R, Anichini C, Abbate R, Gensini G, Pepe G. FBN1 mutation screening of patients with Marfan syndrome and related disorders: detection of 46 novel FBN1 mutations. Clin Genet. 2008;74(1):39–46.

170. Hung CC, Lin SY, Lee CN, Cheng HY, Lin SP, Chen MR, Chen CP, Chang CH, Lin CY, Yu CC, Chiu HH, Cheng WF, Ho HN, Niu DM, Su YN. Mutation spectrum of the fibrillin-1 (FBN1) gene in Taiwanese patients with Marfan syndrome. Ann Hum Genet. 2009;73(Pt 6):559–567.

171. Magyar I, Colman D, Arnold E, Baumgartner D, Bottani A, Fokstuen S, Addor MC, Berger W, Carrel T, Steinmann B, Mátyás G. Quantitative sequence analysis of FBN1 premature termination codons provides evidence for incomplete NMD in leukocytes. Hum Mutat. 2009;30(9):1355–1364.

172. Howarth R, Yearwood C, Harvey JF. Application of dHPLC for mutation detection of the fibrillin-1 gene for the diagnosis of Marfan syndrome in a National Health Service Laboratory. Genet Test. 2007;11(2):146–152.

173. Baudhuin LM, Kotzer KE, Lagerstedt SA. Increased frequency of FBN1 truncating and splicing variants in Marfan syndrome patients with aortic events. Genet Med. 2015;17(3):177–187.

174. Lang RM, Badano LP, Mor-Avi V, Afilalo J, Armstrong A, Ernande L, Flachskampf FA, Foster E, Goldstein SA, Kuznetsova T, Lancellotti P, Muraru D, Picard MH, Rietzschel ER, Rudski L, Spencer KT, Tsang W, Voigt JU. Recommendations for cardiac chamber quantification by echocardiography in adults: an update from the American Society of Echocardiography and the European Association of Cardiovascular Imaging. J Am Soc Echocardiogr. 2015;28(1):1–39.e14.

175. Nagueh SF, Appleton CP, Gillebert TC, Marino PN, Oh JK, Smiseth OA, Waggoner AD, Flachskampf FA, Pellikka PA, Evangelista A. Recommendations for the evaluation of left ventricular diastolic function by echocardiography. J Am Soc Echocardiogr. 2009;22(2):107–133.

176. O'Leary NA, Wright MW, Brister JR, Ciufo S, Haddad D, McVeigh R, Rajput B, Robbertse B, Smith-White B, Ako-Adjei D, Astashyn A, Badretdin A, Bao Y, Blinkova O, Brover V, Chetvernin V, Choi J, Cox E, Ermolaeva O, Farrell CM, Goldfarb T, Gupta T, Haft D, Hatcher E, Hlavina W, Joardar VS, Kodali VK, Li W, Maglott D, Masterson P,

McGarvey KM, Murphy MR, O'Neill K, Pujar S, Rangwala SH, Rausch D, Riddick LD, Schoch C, Shkeda A, Storz SS, Sun H, Thibaud-Nissen F, Tolstoy I, Tully RE, Vatsan AR, Wallin C, Webb D, Wu W, Landrum MJ, Kimchi A, Tatusova T, DiCuccio M, Kitts P, Murphy TD, Pruitt KD. Reference sequence (RefSeq) database at NCBI: current status, taxonomic expansion, and functional annotation. Nucleic Acids Res. 2016;44(D1):D733–745.

177. Downing AK, Knott V, Werner JM, Cardy CM, Campbell ID, Handford PA. Solution structure of a pair of calcium-binding epidermal growth factor-like domains: implications for the Marfan syndrome and other genetic disorders. Cell. 1996;85(4):597–605.

178. Yuan X, Downing AK, Knott V, Handford PA. Solution structure of the transforming growth factor beta-binding protein-like module, a domain associated with matrix fibrils. Embo j. 1997;16(22):6659–6666.

179. Richards S, Aziz N, Bale S, Bick D, Das S, Gastier-Foster J, Grody WW, Hegde M, Lyon E, Spector E, Voelkerding K, Rehm HL. Standards and guidelines for the interpretation of sequence variants: a joint consensus recommendation of the American College of Medical Genetics and Genomics and the Association for Molecular Pathology. Genet Med. 2015;17(5):405–424.

180. Schrijver I, Liu W, Odom R, Brenn T, Oefner P, Furthmayr H, Francke U. Premature termination mutations in FBN1: distinct effects on differential allelic expression and on protein and clinical phenotypes. Am J Hum Genet. 2002;71(2):223–237.

181. Caputi M, Kendzior RJ, Jr., Beemon KL. A nonsense mutation in the fibrillin-1 gene of a Marfan syndrome patient induces NMD and disrupts an exonic splicing enhancer. Genes Dev. 2002;16(14):1754–1759.

182. Hubmacher D, El-Hallous EI, Nelea V, Kaartinen MT, Lee ER, Reinhardt DP. Biogenesis of extracellular microfibrils: Multimerization of the fibrillin-1 C terminus into bead-like structures enables self-assembly. Proc Natl Acad Sci U S A. 2008;105(18):6548–6553.

183. Lu Y, Sherratt MJ, Wang MC, Baldock C. Tissue specific differences in fibrillin microfibrils analysed using single particle image analysis. J Struct Biol. 2006;155(2):285–293.

184. Haston JL, Engelsen SB, Roessle M, Clarkson J, Blanch EW, Baldock C, Kielty CM, Wess TJ. Raman microscopy and X-ray diffraction, a combined study of fibrillin-rich microfibrillar elasticity. J Biol Chem. 2003;278(42):41189–41197.

185. Wang MC, Lu Y, Baldock C. Fibrillin microfibrils: a key role for the interbead region in elasticity. J Mol Biol. 2009;388(1):168–179.

186. Judge DP, Biery NJ, Keene DR, Geubtner J, Myers L, Huso DL, Sakai LY, Dietz HC. Evidence for a critical contribution of haploinsufficiency in the complex pathogenesis of Marfan syndrome. J Clin Invest. 2004;114(2):172–181.

187. Reinhardt DP, Ono RN, Notbohm H, Müller PK, Bächinger HP, Sakai LY. Mutations in calcium-binding epidermal growth factor modules render fibrillin-1 susceptible to proteolysis. A potential disease-causing mechanism in Marfan syndrome. J Biol Chem. 2000;275(16):12339–12345.

188. Liu X, Liu K, Nie D, Zhang J, Zhang L, Liu X, Wang J. Case report: Biochemical and clinical phenotypes caused by cysteine substitutions in the epidermal growth factor-like domains of fibrillin-1. Front Genet. 2022;13:928683.

189. Stengl R, Bors A, Ágg B, Pólos M, Matyas G, Molnár MJ, Fekete B, Csabán D, Andrikovics H, Merkely B, Radovits T, Szabolcs Z, Benke K. Optimising the mutation screening strategy in Marfan syndrome and identifying genotypes with more severe aortic involvement. Orphanet J Rare Dis. 2020;15(1):290.

190. Hollister DW, Godfrey M, Sakai LY, Pyeritz RE. Immunohistologic abnormalities of the microfibrillar-fiber system in the Marfan syndrome. N Engl J Med. 1990;323(3):152–159.

191. Aoyama T, Francke U, Dietz HC, Furthmayr H. Quantitative differences in biosynthesis and extracellular deposition of fibrillin in cultured fibroblasts distinguish five groups of Marfan syndrome patients and suggest distinct pathogenetic mechanisms. J Clin Invest. 1994;94(1):130–137.

192. Dietz HC, McIntosh I, Sakai LY, Corson GM, Chalberg SC, Pyeritz RE, Francomano CA. Four novel FBN1 mutations: significance for mutant transcript level and EGF-like domain calcium binding in the pathogenesis of Marfan syndrome. Genomics. 1993;17(2):468–475.

193. Halliday D, Hutchinson S, Kettle S, Firth H, Wordsworth P, Handford PA. Molecular analysis of eight mutations in FBN1. Hum Genet. 1999;105(6):587–597.

194. Karttunen L, Ukkonen T, Kainulainen K, Syvänen AC, Peltonen L. Two novel fibrillin-1 mutations resulting in premature termination codons but in different mutant transcript levels and clinical phenotypes. Hum Mutat. 1998;Suppl 1:S34–37.

195. Kainulainen K, Sakai LY, Child A, Pope FM, Puhakka L, Ryhänen L, Palotie A, Kaitila I, Peltonen L. Two mutations in Marfan syndrome resulting in truncated fibrillin polypeptides. Proc Natl Acad Sci U S A. 1992;89(13):5917–5921.

196. Takeda N, Inuzuka R, Maemura S, Morita H, Nawata K, Fujita D, Taniguchi Y, Yamauchi H, Yagi H, Kato M, Nishimura H, Hirata Y, Ikeda Y, Kumagai H, Amiya E, Hara H, Fujiwara T, Akazawa H, Suzuki JI, Imai Y, Nagai R, Takamoto S, Hirata Y, Ono M, Komuro I. Impact of Pathogenic FBN1 Variant Types on the Progression of Aortic Disease in Patients With Marfan Syndrome. Circ Genom Precis Med. 2018;11(6):e002058.

197. Akhtar R, Cruickshank JK, Zhao X, Walton LA, Gardiner NJ, Barrett SD, Graham HK, Derby B, Sherratt MJ. Localized micro- and nano-scale remodelling in the diabetic aorta. Acta Biomater. 2014;10(11):4843–4851.

198. Jensen SA, Handford PA. New insights into the structure, assembly and biological roles of 10-12 nm connective tissue microfibrils from fibrillin-1 studies. Biochem J. 2016;473(7):827–838.

199. Cocciolone AJ, Hawes JZ, Staiculescu MC, Johnson EO, Murshed M, Wagenseil JE. Elastin, arterial mechanics, and cardiovascular disease. Am J Physiol Heart Circ Physiol. 2018;315(2):H189–h205.

200. Ramirez F, Sakai LY. Biogenesis and function of fibrillin assemblies. Cell Tissue Res. 2010;339(1):71–82.

201. Rybczynski M, Mir TS, Sheikhzadeh S, Bernhardt AM, Schad C, Treede H, Veldhoen S, Groene EF, Kühne K, Koschyk D, Robinson PN, Berger J, Reichenspurner H, Meinertz T, von Kodolitsch Y. Frequency and age-related course of mitral valve dysfunction in the Marfan syndrome. Am J Cardiol. 2010;106(7):1048–1053.

202. Rybczynski M, Treede H, Sheikhzadeh S, Groene EF, Bernhardt AM, Hillebrand M, Mir TS, Kühne K, Koschyk D, Robinson PN, Berger J, Reichenspurner H, Meinertz T, von Kodolitsch Y. Predictors of outcome of mitral valve prolapse in patients with the Marfan syndrome. Am J Cardiol. 2011;107(2):268–274.

203. Muiño-Mosquera L, De Wilde H, Devos D, Babin D, Jordaens L, Demolder A, De Groote K, De Wolf D, De Backer J. Myocardial disease and ventricular arrhythmia in Marfan syndrome: a prospective study. Orphanet J Rare Dis. 2020;15(1):300.

204. Weigand J, Stephens-Novy S, Sachdeva S, Doan TT, Yasso A, Morris SA. Evidence of cardiomyopathy associated with Marfan syndrome in children. Heart. 2024;110(13):887–891.

205. Herman DS, Lam L, Taylor MR, Wang L, Teekakirikul P, Christodoulou D, Conner L, DePalma SR, McDonough B, Sparks E, Teodorescu DL, Cirino AL, Banner NR, Pennell DJ, Graw S, Merlo M, Di Lenarda A, Sinagra G, Bos JM, Ackerman MJ, Mitchell RN, Murry CE, Lakdawala NK, Ho CY, Barton PJ, Cook SA, Mestroni L, Seidman JG, Seidman CE. Truncations of titin causing dilated cardiomyopathy. N Engl J Med. 2012;366(7):619–628.

206. Trombitás K, Redkar A, Centner T, Wu Y, Labeit S, Granzier H. Extensibility of isoforms of cardiac titin: variation in contour length of molecular subsegments provides a basis for cellular passive stiffness diversity. Biophys J. 2000;79(6):3226–3234.

207. Warren CM, Krzesinski PR, Campbell KS, Moss RL, Greaser ML. Titin isoform changes in rat myocardium during development. Mech Dev. 2004;121(11):1301–1312.

208. Warren CM, Jordan MC, Roos KP, Krzesinski PR, Greaser ML. Titin isoform expression in normal and hypertensive myocardium. Cardiovasc Res. 2003;59(1):86–94.

209. Wu Y, Bell SP, Trombitas K, Witt CC, Labeit S, LeWinter MM, Granzier H. Changes in titin isoform expression in pacing-induced cardiac failure give rise to increased passive muscle stiffness. Circulation. 2002;106(11):1384–1389.

210. Makarenko I, Opitz CA, Leake MC, Neagoe C, Kulke M, Gwathmey JK, del Monte F, Hajjar RJ, Linke WA. Passive stiffness changes caused by upregulation of compliant titin isoforms in human dilated cardiomyopathy hearts. Circ Res. 2004;95(7):708–716.

211. Morano I, Hädicke K, Grom S, Koch A, Schwinger RH, Böhm M, Bartel S, Erdmann E, Krause EG. Titin, myosin light chains and C-protein in the developing and failing human heart. J Mol Cell Cardiol. 1994;26(3):361–368.

212. Demolder A, Devos D, De Backer J, Muiño-Mosquera L. Assessment of Myocardial Fibrosis in Marfan Syndrome Using Cardiac Magnetic Resonance Imaging. Mol Genet Genomic Med. 2024;12(11):e70024.

9. Bibliography of the candidate's publications

9.1. Peer-reviewed articles related to the PhD thesis (Σ IF = 7.8)

1. **Șulea CM**, Mártonfalvi Z, Csányi C, Haluszka D, Pólos M, Ágg B, Stengl R, Benke K, Szabolcs Z, Kellermayer MSZ. Nanoscale Structural Comparison of Fibrillin-1 Microfibrils Isolated from Marfan and Non-Marfan Syndrome Human Aorta. Int J Mol Sci. 2023;24(8):7561. **IF: 4.9**
2. Kellermayer D*, **Șulea CM***, Tordai H, Benke K, Pólos M, Ágg B, Stengl R, Csonka M, Radovits T, Merkely B, Szabolcs Z, Kellermayer M, Kiss B. Marfan syndrome cardiomyocytes show excess of titin isoform N2BA and extended sarcomeric M-band. J Gen Physiol. 2025;157(3):e202413690. *: shared first authorship. **IF: 2.9**

9.2. Oral and poster presentations related to the PhD thesis

1. **Șulea CM**, Mártonfalvi Z, Csányi C, Haluszka D, Pólos M, Benke K, Szabolcs Z, Kellermayer MSZ. Nanoscale morphological and mechanical properties of fibrillin-1 microfibrils isolated from human Marfan and non-Marfan aorta. 49th European Muscle Conference, Prague, Czech Republic. 2022.
2. **Șulea CM**, Mártonfalvi Z, Csányi C, Haluszka D, Pólos M, Benke K, Szabolcs Z, Kellermayer MSZ. Fibrillin-1 microfibrils in Marfan syndrome: nanoscale structural characterization using atomic force microscopy. 29th Congress of the Hungarian Biophysical Society, Budapest, Hungary. 2023.
3. **Șulea CM**, Sziklai D, Pólos M, Benke K, Szabolcs Z, Kellermayer MSZ. Atomic force microscopy investigation of human fibrillin microfibril morphology and mechanics in Marfan syndrome. XXIII. Linz Winter Workshop, Linz, Austria. 2024.
4. Kellermayer D, **Șulea CM**, Kiss B, Benke K, Pólos M, Ágg B, Csonka M, Tordai H, Radovits T, Merkely B, Szabolcs Z, Kellermayer M. Titin isoform expression in the left ventricle of Marfan-syndrome patients. 51st European Muscle Conference, Ljubljana, Slovenia. 2024.
5. Kellermayer D, **Șulea CM**, Benke K, Pólos M, Ágg B, Csonka M, Tordai H, Radovits T, Merkely B, Szabolcs Z, Kellermayer M, Kiss B. Titin isoforms and structural layout in the cardiac sarcomere of Marfan syndrome patients. 69th Biophysical Society Annual Meeting, Los Angeles, USA. 2025.

9.3. Other peer-reviewed articles (Σ IF = 17.418)

1. Pólos M, **Şulea CM**, Benke K, Ágg B, Kovács A, Hartyánszky I, Merkely B, Schäfers HJ, Szabolcs Z. Giant unruptured sinus of Valsalva aneurysm successfully managed with valve-sparing procedure - a case report. J Cardiothorac Surg. 2020;15(1):6. **IF: 1.637**
2. Pólos M, Domokos D, **Şulea CM**, Benke K, Csikós G, Nagy A, Skoda R, Szabó A, Merkel E, Hartyánszky I, Szabolcs Z, Merkely B, Becker D. Needle in the heart: a rare case of cardiac tamponade caused by a migrated foreign body and mimicking ST segment elevation myocardial infarction. BMC Cardiovasc Disord. 2021;21(1):143. **IF: 2.174**
3. Pólos M, Stengl R, **Şulea CM**, Benke K, Bartha E, Ágg B, Koppányi Á, Hartyánszky I, Székely A, Németh E, Kovács A, Merkely B, Szabolcs Z. Stratégiai szemléletváltás a Marfan-szindrómás betegeken végzett aortagyök-rekonstrukciókban [Changing strategies in aortic root reconstruction in Marfan syndrome]. Orv Hetil. 2021;162(18):696–704. **IF: 0.707**
4. **Şulea CM***, Lakatos B*, Kovács A, Benke K, Suhai FI, Csulak E, Merkel E, Nagy B, Hartyánszky I, Merkely B, Szabolcs Z, Pólos M. Blood-filled cyst of the tricuspid valve: Multiple cardiac disorders, one surgical case. J Card Surg. 2022;37(1):245–248. *: shared first authorship. **IF: 1.6**
5. **Şulea CM**, Nădășan V, Ursachi T, Toboltoc PC, Benedek T. What Patients Find on the Internet When Looking for Information About Percutaneous Coronary Intervention: Multilanguage Cross-sectional Assessment. J Med Internet Res. 2022;24(12):e41219. **IF: 7.4**
6. **Şulea CM**, Csobay-Novák C, Oláh Z, Banga P, Szeberin Z, Soltész Á, Jokkel Z, Benke K, Csonka M, Merkel ED, Merkely B, Szabolcs Z, Pólos M. Staged Hybrid Repair of a Complex Type B Aortic Dissection. J Cardiovasc Dev Dis. 2022;9(9):297. **IF: 2.4**
7. **Şulea CM***, Kiss AB*, Ágg B, Benke K, Bartha E, Szilveszter B, Stengl R, Csonka M, Szabolcs Z, Pólos M. Pregnancy-related chronic type A aortic dissection highlights the importance of thorough prenatal maternal examination. J Cardiothorac Surg. 2025;20(1):105. *: shared first authorship. **IF: 1.5**

10. Acknowledgements

This research was supported by grants from the Hungarian National Research, Development and Innovation Office (K135360 and FK145928) and the New National Excellence Program of the Ministry for Culture and Innovation from the source of the National Research, Development, and Innovation Fund (ÚNKP-22-3-I-SE-49, UNKP-23-3-II-SE-22, and ÚNKP-19-3-I). TKP2021-EGA-23 has been implemented with the support provided by the Ministry of Innovation and Technology of Hungary from the National Research, Development and Innovation Fund, financed under the TKP2021-EGA funding scheme. Project no. RRF-2.3.1-21-2022-00003 (National Cardiovascular Laboratory) was implemented with the support provided by the European Union.

I am immensely grateful to my supervisors for their tremendous support, enthusiasm, and guidance, which have shaped my growth as both a researcher and a healthcare professional. I wish to extend my sincere thanks to Prof. Dr. Miklós Kellermayer for teaching me the rigor and beauty of scientific research, for nurturing my curiosity, and for constantly encouraging me to think beyond boundaries. I am equally thankful to Prof. Dr. Zoltán Szabolcs, who recognized my potential early on and welcomed me into the Marfan Research Group. From him, I have learned the principles of distinguished clinical practice – lessons that will undoubtedly guide my future career.

I wish to thank the members of the Hungarian Marfan Foundation and the Marfan Research Group for their teamwork and for generously sharing their expertise. My appreciation goes to Dr. Kálmán Benke for his steadfast support and stimulating discussions, to Dr. Miklós Pólos for providing samples, and to Dr. Bence Ágg for his meticulous assistance in reviewing my manuscripts. Furthermore, I would also like to thank Prof. Dr. Béla Merkely for his visionary support of research, Dr. Tamás Radovits for the opportunity to join the Transplantation Biobank team, and all involved coworkers from the Semmelweis University Heart and Vascular Center who facilitated this research.

I am sincerely grateful to my colleagues in the Department of Biophysics and Radiation Biology for their warm welcome and for fostering a supportive, intellectually stimulating environment, where not once were my questions left unanswered. I owe particular gratitude to Dr. Zsolt Mártonfalvi for his tremendous help in establishing and optimizing the experimental setup; to Dr. Bálint Kiss, Dr. Dóra Haluszka, and Dr. Csilla

Csányi for their indispensable guidance in mastering atomic force microscopy; to Dr. Dominik Sziklai for the many brainstorming sessions and his assistance with Python programming; and to Dr. Dalma Kellermayer for her extensive efforts in the titin experiments and for providing key data for the analysis.

I express my heartfelt appreciation to the Hungarian Marfan syndrome patient community and all study participants for their willingness to contribute to research, with the shared ambition of advancing knowledge and improving care. I also wish to acknowledge the contribution of laboratory animals involved in the refinement of experimental methods, whose role was instrumental to the success of this work.

On a personal note, I am profoundly grateful to my family for their unwavering support, constant motivation, and care. Finally, to my person: thank you for your endless patience and for always believing in me.

Per aspera ad astra.